NASA Technical Memorandum 81258

An Extension of the Local Momentum Theory to a Distorted Wake Model of a Hovering Rotor

Keiji Kawachi

February 1981

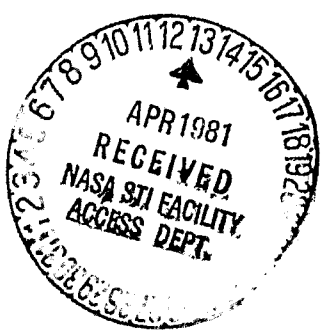

National Aeronautics and
Space Administration

NASA Technical Memorandum 81258

An Extension of the Local Momentum Theory to a Distorted Wake Model of a Hovering Rotor

Keiji Kawachi, NASA Ames Research Center, Moffett Field, California

National Aeronautics and
Space Administration

Ames Research Center
Moffett Field, California 94035

AN EXTENSION OF THE LOCAL MOMENTUM THEORY TO A DISTORTED WAKE MODEL OF A HOVERING ROTOR

Keiji Kuwachi*
Ames Research Center

Summary

The fundamentals of the Local Momentum Theory and a recent extension of this theory are presented in this report. The Local Momentum Theory is based on the instantaneous balance between the fluid momentum and the blade elemental lift at a local station in the rotor rotational plane. Therefore, the theory has the capability of evaluating time-wise variations of air-loading and induced velocity distributions along a helicopter blade span. Unlike a complex vortex theory, this theory was developed to analyze the instantaneous induced velocity distribution effectively. This presentation of the fundamentals of the Local Momentum Theory makes clear the boundaries of this theory and assists to make a computer program using this theory. A new concept introduced into the theory in this report is the effect of the rotor wake contraction in hovering flight. A comparison of this extended Local Momentum Theory with a prescribed wake vortex theory is also presented. The results indicate that the extended Local Momentum Theory has the capability of achieving a level of accuracy similar to that of the prescribed wake vortex theory over wide range variations of rotor geometrical parameters. It is also shown that the analytical results obtained using either theory are in reasonable agreement with experimental data.

Introduction

This paper has two purposes: (1) to give a more detailed explanation of the Local Momentum Theory than has been given in previous papers[1,2,3]; and (2) to present recent improvements of the theory.

---

*National Research Council Associate.

There are two theories commonly used to estimate the induced velocity distribution and the airloading distribution of a helicopter rotor, vortex theory and momentum theory. Vortex theory has the capability of analyzing the induced flow field exactly, but the numerical integration requires considerable computer time. In addition, difficulties exist in the analysis of complex problems such as predicting rotor airloading under maneuvering conditions, even if a rigid wake system is assumed.

In contrast, the ordinary momentum theory is simpler, being based on the assumption that the induced velocity is uniform over the entire rotor disk[4]. This, however, leads to unreliable airloading calculations. To overcome this shortcoming, various changes have been suggested. First, a rotor disk was assumed to be divided into annular ring elements[5], and momental balance was considered on these elements. Then, the concept of the annular ring elements was extended to the pie-shaped elements[6] in order to analyze the azimuth-wise asymmetric flow field. Using these elements, a few analyses were presented for a low frequency response of a helicopter rotor[7,8]. In addition to the nonuniformity in space, the time-wise variation of the induced velocity has been considered within the frame of the momentum theory. The concept of apparent mass was proposed for an entire rotor disk, the value of which was determined by an experimental study of the thrust variation following a rapid collective pitch change[9,10]. The concept was then extended to apply to the pie-shaped elements, and improvement of the predicting capability was achieved[11-15] for low frequency response of a rotor. As a further extension, the Local Momentum Theory was proposed by Dr. Azuma and this author[1,2].

In the Local Momentum Theory, a rotor blade is represented by a series of n overlapping wings of decreasing wing-span. Each overlapping wing has an elliptical circulation along its wing-span, producing, therefore, a uniform downwash velocity. The actual airloading and induced velocity distribution of a real rotor blade is represented by the summation of the lift and induced velocity of this series of n overlapping wings. Momentum theory is used to obtain the relation between the lift distribution and the induced velocity distribution for each overlapping wings. Consequently, in this theory, the momentum generated by a blade itself is counted. In contrast, in the previous momentum theory, the momentum generated by an entire or partial rotor disk is considered. Because of this basic difference, the theory was named Local Momentum Theory, and it has the capability of predicting the higher frequency loading of a helicopter rotor and also a more precise airloading distribution along a blade span than have the previous momentum theories. The present theory, however, requires the use of a computer; therefore, the theory cannot give an analytical solution which is useful in obtaining a general view of a phenomenon.

By comparison with vortex theory, the Local Momentum Theory can achieve an equal level of accuracy, using a much smaller amount of computer time. The reasons are as follows: the theory does not require the iterative procedure nor the calculation of the inverse matrix; and numerical integration is avoided by using the attenuation coefficient, which expresses the timewise variation of the induced velocity. The present theory, however, requires more complicated analytical procedure than that which is required by vortex theory.

The theory presented in this paper is applicable not only to steady state conditions, but also to various kinds of low frequency rotor responses, where trailing vortices play the primary role in the creation of the unsteady phenomena. The present theory is, however, based on steady airfoil characteristics; therefore, some extension of the theory is necessary when applying it to a problem of very high frequency rotor response, such as flutter, where shed vortices are the primary cause of the unsteady phenomena. An example of the extension of the present theory is shown in Ref. 21, where the unsteady airfoil characteristics, such as Wagner function, Küssner function or the apparent mass for a blade, have been introduced in order to study the rotor gust response.

The Local Momentum Theory was recently extended to include the effect of the rotor wake contraction in hovering flight. The theory previously assumed that the wake of a hovering rotor did not move in the radial direction; therefore, the theory gave almost the same result as the rigid wake vortex theory[1,2]. It has been pointed out, however, that the wake deformation has strong effects on the airloading and induced velocity distribution in hovering flight[16,17,18]. This extension of the theory to include the wake deformation effect was necessary in order to analyze airloading distributions measured by a laser velocimeter[33,34]. In the new contraction model to be described in this paper, fluid elements surrounding a rotor can be moved as observed in experiments[16,17,18]. In addition, the model to calculate the attenuation coefficient was improved in order to include the effect of the blade tip vortex. The spanwise lift distributions obtained by this extended Local Momentum Theory are compared with experimental results with those of a prescribed wake vortex theory[18,22].

Notation

(A_{ij})	matrix
AR	aspect ratio of a wing
a	lift curve slope (rad^{-1})
a_s	speed of sound
B	constant or tip loss factor
b	wing span or number of blades
C	constant or attenuation coefficient
C*	equivalent attenuation coefficient given by equation (57)
C_T	thrust coefficient = $T/\rho\pi R^2(\Omega R)^2$
c	wing chord
f	function given by equations (15) and (16)
G	function given by equation (A.1-9)
g	function given by equation (A.1-5)
H	function given by equation (A.3-7)
I_β	moment of inertia of a blade about flapping hinge = $\int_{r_\beta}^{R}(r-r_\beta)^2 dm$
I	running index or inclination angle of tip path plane (positive forward tilt)
(i,j,k)	coordinate of a blade element
J	running index
K	parameters showing tip vortex positions
k_β	spring stiffness at flapping hinge
L	lift
ℓ	airloading
(ℓ,m)	coordinate of a station on rotor rotational plane
M	Mach number
M_o	apparent mass of impervious disk given by equation (65)
M_β	mass moment of a blade about flapping hinge = $\int_{r_\beta}^{R} r(r-r_\beta)\,dm$

m	mass of air
$\bar{m}$	mass of air associated with local momentum given by equations (21), (26) and (47)
n	number of spanwise partition
p	rolling angular velocity of a rotor (positive advancing-side down)
q	pitching angular velocity of a rotor (positive nose up)
R	rotor radius
r	radial position
r_β	flapping hinge offset
T	thrust
t	time
U	horizontal inflow velocity of a blade element given by equation (29)
V	forward velocity
$V_{i,c}$	mean horizontal inflow velocity of the i-th elliptical wing given by equation (33)
V_N	normal component of inflow velocity (positive downward)
v	induced velocity (positive downward)
(X,Y,Z)	coordinate of fixed wing shown in Fig. 1
x	nondimensional radial position = r/R
$x_{r,c}$	nondimensional radial position given by equation (44)
x_T	nondimensional radial position of tip vortex given by equation (66)
x_β	nondimensional flapping hinge offset = r_β/R
y	spanwise position of fixed wing
Z	distance from rotor rotational plane (positive downward)
z_T	nondimensional axial position of tip vortex given by equation (67)

β	flapping angle (positive blade up) = $\beta_0 + \beta_{1c}\cos\psi + \beta_{1s}\sin\psi$
$\bar{\beta}_0$	preconing angle
Γ	circulation
γ	lock number = $\rho a c R^4/I_\beta$
Δ	small increment
δ_{lm}	function given by equations (50) and (53)
ζ	nondimensional spanwise position
η	nondimensional spanwise position of fixed wing given by equation (6)
θ	blade pitch angle (positive leading-edge up) = $\theta_0 + \theta_t(x-0.75) + \theta_{1c}\cos\psi + \theta_{1s}\sin\psi + \cdots$
θ_t	blade twist rate
$\theta_{0.75}$	collective pitch angle at x = 0.75
λ	running index or inflow ratio = $(V\sin i + v)/\Omega R$
μ	advance ratio = $V\cos i/\Omega R$
ξ	nondimensional spanwise position of each elliptical wing
ρ	air density
Σ	summation
σ	solidity = $bc/\pi R$
ϕ	inflow angle or wake age
χ	skewed angle
ψ	azimuth angle
Ω	rotor rotational speed

Subscripts

b	number of blades
cy	cylinder
down	downwash
elp	elliptical wing

i	spanwise partition, the quantity of i-th elliptical wing, or the quantity of tip vortex No. i
j	azimuth-wise or time-wise partition, spanwise position, or the quantity of j-th elliptical wing
k	the quantity of k-th blade
p	representative point
root	blade root
tip	blade tip
up	upwash
Γ	circulation
λ	azimuth-wise or time-wise partition
0	uniform or initial value
1c,1s	first harmonic contents of Fourier cosine and sine series
0.75	the quantity at three-quarter radial position
Superscript	
$(\dot{})$	d ()/dt
$(\ )^{j}_{\ell m}$	the quantity at a station (ℓ, m) at time t = j

Fundamentals of the Local Momentum Theory

Fixed Wing

Fig. 1[1] shows the air flow field surrounding an elliptical wing flying with constant forward speed V. A well-known result from the lifting line theory[19] is that the induced velocity is uniform inside the wing span and the uniform induced velocity, v_0 is developed to $2v_0$ far downstream. Outside the wing span, there are upwash regions, but they are concentrated near the wing tips. Considering the momentum change, the total lift of wing L is given:

$$L = 2mv_0 \tag{1}$$

where, $m = \rho V \pi \left(\frac{b}{2}\right)^2$ (2)

The lift distribution, ℓ, and induced velocity distribution, v, are:

$$\ell = \frac{4L}{\pi b}\sqrt{1-\eta^2} \tag{3}$$

$$v \begin{cases} = v_0 & ; |\eta| \leq 1 \text{ inside the wing span} \quad (4) \\ = v_0\left(1 - |\eta|/\sqrt{\eta^2-1}\right) & ; |\eta| > 1 \text{ outside the wing span} \quad (5) \end{cases}$$

where

$$\eta = y/\left(\frac{b}{2}\right) \tag{6}$$

When a wing has an arbitrary planform or lift distribution, we may consider that the wing is composed of a series of n hypothetical elliptical wings. The elliptical wings may be arranged arbitrarily, for example, Fig. 2[1] shows a symmetrical arrangement and a one-sided arrangement. In each elliptical wing, the momentum balance is given by equations (1) and (2). Using a suffix to designate quantities of the i-th elliptical wing, equations (1) and (2) are rewritten as follows:

$$L_i = 2 m_i \Delta v_i \tag{7}$$

where,

$$m_i = \rho V \pi \left(\frac{b_i}{2}\right)^2 \tag{8}$$

The present theory was developed with the use of a computer; therefore, expressions with suffixes are adopted in this report for convenience in programming.

The lift distribution, $\ell(\eta)$, on the most left hand wing in Fig. 2[1] is expressed by the summation of elliptical lift, $\ell_i(\xi)$, on the component wings. As the lift distribution of each elliptical wing, $\ell_i(\xi)$, can be obtained by using a relationship similar to equation (3), the following equation is obtained :

$$\ell(\eta) = \sum_{i=1}^{\dagger} \ell_i(\xi) = \sum_{i=1}^{\dagger} \frac{4L_i}{\pi b_i} \sqrt{1-\xi^2} \tag{9}$$

where

$$\xi = (y - y_{oi}) / \left(\frac{b_i}{2}\right) \tag{10}$$

and y_{oi} shows the origin of the ξ axis, that is, the mid-span of each elliptical wing. Substituting $y = \left(\frac{b}{2}\right)\eta$ from equation (6) into (10), equation (10) becomes

$$\xi = (\eta - \eta_{oi})(b/b_i) \qquad (11)$$

where

$$\eta_{oi} = y_{oi}/(\tfrac{b}{2}) \qquad (12)$$

In the above equations, ξ is the non-dimensional coordinate fixed to each of the elliptical wings and j is the number of elliptical wings which include the point, η, within their span; therefore, only $|\xi| \leq 1$ is considered in equation (9).

Substituting equations (7) and (8) into (9), the lift distribution, $\ell(\eta)$, can be expressed directly by the downwash of each elliptical wing Δv_i, then

$$\ell(\eta) = \sum_{i=1}^{j} 2\rho V b_i \Delta v_i \sqrt{1-\xi^2} \qquad (13)$$

The induced velocity distribution of the most left hand wing in Fig. 2[1], $v(\eta)$, is also given by the summation of downwashes and upwashes of the component elliptical wings. As the induced velocity distribution of each elliptical wing is given by equations (4) and (5), the following can be obtained:

$$v(\eta) = \sum_{i=1}^{n} \Delta v_i f(\xi) = \sum_{i=1}^{j} \Delta v_i f_{down}(\xi) + \sum_{i=j+1}^{n} \Delta v_i f_{up}(\xi) \qquad (14)$$

where

$$f(\xi) \begin{cases} = f_{down}(\xi) = 1 & ; |\xi| \leq 1 \qquad (15) \\ = f_{up}(\xi) = 1 - |\xi|/\sqrt{\xi^2 - 1} & ; |\xi| > 1 \qquad (16) \end{cases}$$

In the above equations, f_{down} expresses the uniform downwash inside the wing span of each elliptical wing and f_{up} expresses the upwash outside the wing span of each elliptical wing. According to blade element theory, the lift distribution of a wing is:

$$\ell(\eta) = \frac{1}{2}\rho V^2 C a\left(\theta - \frac{v(\eta)}{V}\right) \qquad (17)$$

Substituting equation (14) into (17), equation (17) becomes

$$\ell(\eta) = \frac{1}{2}\rho V^2 C a\left(\theta - \sum_{i=1}^{n}\Delta v_i f(\xi)/V\right) \qquad (18)$$

Now, two expressions of lift distribution, that is, equations (13) and (18), have been obtained using momentum theory and blade element theory respectively. In both equations, the only unknown variable is the downwash generated by each elliptical wing, i.e., Δv_i $(i = 1 \sim n)$.

Equations to solve for Δv_i from equations (13) and (18) are derived as follows:

The lift per unit span, ℓ_j, acting on a local segment spanned by $(-\eta_j, -\eta_{j+1})$ (cross hatched area in Fig. 3) is given

$$\ell_j = \int_{-\eta_j}^{-\eta_{j+1}} \ell(\eta)\, d\eta/(\eta_j - \eta_{j+1}) \qquad (19)$$

where, η_j and η_{j+1} are the tip positions of the j-th elliptical wing, and the (j + 1)-th elliptical wing respectively (Fig. 3), and they are non-dimensionalized by using equation (6). Substituting equations (13) and (18) into (19) gives two expressions for ℓ_j. Then, equating these expressions and using equation (11), the following relation is obtained:

$$l_j = \int_{-\eta_j}^{-\eta_{j+1}} \frac{1}{2} \rho V^2 C a \left(\theta - \sum_{i=1}^{n} \Delta v_i f(\xi)/V\right) d\eta/(\eta_j - \eta_{j+1})$$

$$= \sum_{i=1}^{j} 2 \bar{m}_i \Delta v_i \qquad (20)$$

where

$$\bar{m}_i = \int_{-\eta_j}^{-\eta_{j+1}} \rho b_i V \sqrt{1-\left(\frac{1}{b}\right)^2 (\eta - \eta_{oi})^2}\, d\eta/(\eta_j - \eta_{j+1}) \qquad (21)$$

and η_{oi} is given by equation (12). The above equation indicates that the lift due to blade element theory at a local segment spanned by $(-\eta_j, -\eta_{j+1})$ is balanced with the local momentum change.

When the wing chord $C(\eta)$ and the geometrical attack angle $\theta(\eta)$ are given in the simple forms, equation (20) is analytically integrated, and n x n simultaneous equations to solve for Δv_i $(i = 1 \sim n)$ are obtained by changing j value from 1 to n in equation (20):

$$(A_{ij}) \begin{pmatrix} \Delta v_1 \\ \vdots \\ \Delta v_n \end{pmatrix} = \begin{pmatrix} B_1 \\ \vdots \\ B_n \end{pmatrix} \qquad (22)$$

When equation (20) cannot be analytically integrated, $C(\eta)$ and $\theta(\eta)$ are considered uniform inside the local segment spanned by $(-\eta_j, -\eta_{j+1})$, and the values at the middle point of the local segment may be adopted:

$$C_j = C\left(\eta = \frac{-\eta_j - \eta_{j+1}}{2}\right) \tag{23}$$

$$\theta_j = \theta\left(\eta = \frac{-\eta_j - \eta_{j+1}}{2}\right) \tag{24}$$

In this simplification, equation (20) can be integrated analytically, but a larger number of spanwise partitions is usually necessary to achieve a similar level of accuracy.

Instead of the integral method as stated in equation (20), there is another way to obtain n × n simultaneous equations, i.e., equation (22) to solve for ΔV_i ($i = 1 \sim n$). Selecting a representative point, η_{pj}, inside the local segment spanned by $(-\eta_j, -\eta_{j+1})$ and substituting η_{pj} into equation (13) and equation (18) respectively, the following relations are obtained:

$$\ell(\eta_{pj}) = \frac{1}{2} \rho V^2 C_{pj} a \left(\theta_{pj} - \sum_{i=1}^{n} \Delta V_i f(\xi_{pj})/V\right)$$

$$= \sum_{i=1}^{j} 2 \bar{m}'_i \Delta V_i \tag{25}$$

where

$$\left.\begin{aligned} \bar{m}'_i &= \rho V b_i \sqrt{1-\xi_{pj}^2} \\ C_{pj} &= C(\eta = \eta_{pj}) \\ \theta_{pj} &= \theta(\eta = \eta_{pj}) \\ \xi_{pj} &= (\eta_{pj} - \eta_{oi})(b/b_i) \end{aligned}\right\} \quad (26)$$

Although equations (25) and (26) have simpler form than equations (20), (21), (23) and (24), the author prefers the integral method (equations (20), (21), (23) and (24)) to the other (equations (25) and (26)). His previous calculations for a rectangular wing showed that a smaller number of spanwise partitions was required in the integral method than in the representative point method to achieve a similar level of accuracy.

As shown in Fig. 1[1], the upwash regions outside the elliptical wing are concentrated near the wing tips; therefore, let us assume the upwash velocity induced by each elliptical wing can be neglected, that is, $f_{up}(\xi) = 0$ in equation (16). Substituting equation (15) into (14) and using the assumption $f_{up}(\xi) = 0$, equation (14) becomes

$$w(\eta) = \sum_{i=1}^{n} \Delta w_i f(\xi) = \sum_{i=1}^{j} \Delta w_i \qquad (27)$$

Using equations (23), (24), and (27), equation (20) becomes

$$\ell_j = \int_{-\eta_j}^{-\eta_{j+1}} \frac{1}{2} \rho V^2 C_j a \left(\theta_j - \sum_{i=1}^{j} \Delta w_i / V\right) d\eta / (\eta_j - \eta_{j+1})$$

$$= \sum_{i=1}^{j} 2 \bar{m}_i \Delta w_i \qquad (28)$$

where $\bar{m}_i$ is given in equation (21). In the above equation, the only unknown variable is Δv_i ($i = 1 \sim j$) instead of Δv_i ($i = 1 \sim n$) as in equation (20); therefore, changing the value of j from 1 to n in equation (28), the solution of Δv_j from 1 to n can be obtained without calculating the inverse matrix or any iterations. In other words, the coefficient matrix in equation (22), (A_{ij}), becomes triangular by neglecting the upwash outside each elliptical wing. The sample calculation of this procedure and recurrence equation to solve Δv_j are presented in appendix A-1. After the value of Δv_j has been obtained in the above procedure, the induced velocity distribution and the lift distribution can be calculated by using equations (27) and (17) respectively.

An example of the application of the present method for calculating lift and induced velocity distributions for a rectangular wing with aspect ratio (AR) = 6 is shown in Fig. 4[1]. The number of spanwise partitions is n = 50. The solid line and the broken line show the results when using the Local Momentum Theory with a one-sided arrangement and with a symmetrical arrangement respectively. The chain line shows the results when using lifting line theory[20]. The discrepancy in the results between the present theory and lifting line theory can be eliminated completely by introducing the upwashes that have been neglected in the present calculation. The error due to the neglect of the upwash is less in the middle of the wing span than in the other parts for the symmetrical arrangement. On the other hand, for the one-sided arrangement, the error is less in the tip of the wing than

in the other parts. Therefore, Fig. 4[1] shows that the error due to the neglect of the upwash is less in that area of each elliptical wing which is common to every other elliptical wing. Also, it is shown that the error is not very much even in the worst case, because the upwash region is limited to an area near the tip of each elliptical wing as shown in Fig. 1[1]. When a more precise estimation is needed in using the Local Momentum Theory, the upwash generated by an elliptical wing can be calculated as an iterative procedure. Usually, however, this procedure is not necessary when applying the present theory to the rotary wing.

Rotary Wing

When trying to apply the present theory to a rotary wing, the following differences between the fixed wing and the rotary wing should be considered: (1) the forward speed of a rotor blade is not uniform along the blade span because the rotor blade is rotating, and (2) the following blade may pass through the local station on the rotor rotational plane where the induced velocity generated by the preceding blade still remains. Therefore, the time-wise variation of the induced velocity generated by a preceding blade, should be estimated when analyzing the airloading of the following blade. To account for these differences, the theory is extended as follows. As shown in Fig. 5[1], a rotor blade is assumed to be operated in a sheared flow in the rotor rotational plane. The forward velocity of the sheared flow is given along the blade span as follows:

$$U(x) = V \sin\psi + \Omega R x \qquad (29)$$

where V is the forward speed of the rotor, and ψ is the azimuth angle of the rotor blade.

It is assumed that the rotor blade is composed of hypothetical elliptical wings similar to the case of the fixed wing. (For convenience, an elliptical wing means a wing which has elliptical circulation along the span, although such a wing does not have elliptical planform nor elliptical lift distribution because of its operation in sheared flow.) By this approximation of the flow, the trailing vortices shed from each elliptical wing may be considered to be straight, perpendicular to the wing span and to extend to infinity; therefore, referring to the Biot-Savart relationship, the induced velocity distribution along the span of each elliptical wing is the same as in the case of the fixed wing, i.e. uniform within the blade span, and it is given by equations (4) and (5).

If each elliptical wing is one-sidedly arranged as shown in Fig. 5[1], the lift near the blade tip can be estimated more correctly than the lift in other parts of the blade by using the Local Momentum Theory, as discussed above. As the greater part of lift acts on the blade elements near the blade tip, this arrangement is especially suitable for the calculation of a helicopter rotor blade, and it gives a better estimation of airloading.

In each elliptical wing spanned by ($R\chi_i$, R), as shown on the right-hand side of Fig. 5[1], the following momentum balance can be obtained (Refer to Appendix A-2):

$$L_i = 2 m_i \Delta V_i \tag{30}$$

$$m_i = \rho \pi \left(\frac{b_i}{2}\right)^2 V_{i,c} \tag{31}$$

where

$$b_i = R(1 - \chi_i) \tag{32}$$

$$V_{i,c} = V \sin\psi + \Omega R(1 + \chi_i)/2 \tag{33}$$

In the above equations, b_i means the span length of each elliptical wing and $V_{i,c}$ expresses the mean speed of the sheared flow along the span of the elliptical wing (Refer to equation (29)). Referring to Appendix A-2, the lift distribution on each elliptical wing, $(l_i)_{elp}$, is given as follows:

$$(l_i(\chi))_{elp} = (2\rho V_{i,c}\, b_i\, \Delta\nu_i)\left(U/V_{i,c}\right)\sqrt{1-\xi^2} \tag{34}$$

where $U(\chi)$, b_i and $V_{i,c}$ are given by equations (29), (32) and (33), respectively. ξ is the non-dimensional axis fixed to each elliptical wing and it is related to the non-dimensional rotor radius, i.e. x, as shown in the following equations, because a one-sided arrangement is adopted here (Refer to Fig. 6[1]).

$$\xi = \{2\chi - (1+\chi_i)\}/(1-\chi_i) \tag{35}$$

Similar to the case of the previous fixed wing, the lift distribution and the induced velocity distribution of the rotor blade shown on the most left-hand side in Fig. 5[1] are given by the summation of those of the component elliptical wings. These concepts are schematically shown in Fig. 6[1].

Using equation (34) and neglecting upwash outside each elliptical wing, the following equations are obtained:

$$L(x) = \sum_{i=1}^{i'} (l_i(x))_{elp}$$

$$= \sum_{i=1}^{i'} (2\rho V_{i,c} b_i \Delta v_i)(v(x)/V_{i,c})\sqrt{1-\xi^2} \quad (36)$$

$$v(x) = v_{i,j,k} = \sum_{i=1}^{i'} \Delta v_i \quad (37)$$

where i' means the number of elliptical wings which include the point, x, within their span.

In this subsection, for convenience in numerical calculations, many variables are expressed by using subscripts. Generally, the first subscript of any quantity, i, indicates the i-th radial segment of the blade, the second subscript, j, indicates the time or azimuth-wise location of the blade segment, and the third subscript, k, indicates the k-th blade of a b-bladed rotor. When using this subscript form of expression, variables may be considered as uniform inside a given blade segment. For example, the spanwise induced velocity distribution, $v(x)$ in equation (37), is also the azimuth-wise variable and may have a different value for each blade; therefore, $v(x)$ is expressed as $v_{i,j,k}$, that is, the induced velocity generated by the (i, j, k) blade segment. However, for the sake of simplicity, more abbreviated expressions are sometimes used. In equation (37), for example, Δv_i is used instead of $\Delta v_{i,j,k}$, although Δv is the spanwise and azimuthwise variable and is also a function of each blade.

The other expression of the spanwise lift distribution may be derived by using blade element theory as follows:

$$\ell(x) = \frac{1}{2}\rho U^2 C a (\theta - \phi) \tag{38}$$

where ϕ is the inflow angle. In the case of the rotary wing, the induced velocity generated by the preceding blade may affect the inflow angle. However, for simplicity, the equation to obtain the lift distribution is discussed first, and the mathematical model to estimate the inflow angle will be presented later.

From the above discussion of the "integral method" in the case of the fixed wing, we may now derive simultaneous equations to solve Δv_i from equations (36), (37) and (38). Here, the integral area is chosen as $(x_{i'}, x_{i'+1})$, because $x_{i'}$ and $x_{i'+1}$ are the tip positions of the i'-th elliptical wing and $(i'+1)$-th elliptical wing respectively (Refer Fig. 3). Equating the lift per unit span, $\ell_{i'}$, acting on a local segment spanned by $(x_{i'}, x_{i'+1})$, the following equations can be obtained;

$$\ell_{i'} = \int_{x_{i'}}^{x_{i'+1}} \frac{1}{2}\rho U_{i'}^2 C_{i'} a_{i'} (\theta_{i'} - \phi_{i'})\, dx / (x_{i'+1} - x_{i'})$$

$$= \sum_{i=1}^{i'} 2\bar{m}_i \Delta v_i \tag{39}$$

where

$$U_{i'} = V \sin\psi + \Omega R x_{i',c} \tag{40}$$

$$C_{i'} = C(x = x_{i',c}) \tag{41}$$

$$\theta_{i'} = \theta(x = x_{i',c}) \tag{42}$$

$$a_{i'} = a(x = x_{i',c}) \tag{43}$$

$$x_{i',c} = (x_{i'} + x_{i'+1})/2 \tag{44}$$

$$\phi_{i'} = (V_N + v_{im}^{+} + v_{i+k})/U_{i'} \tag{45}$$

$$V_N = V \sin i \tag{46}$$

$$\overline{m}_i = \int_{x_{i'}}^{x_{i'+1}} \rho V_{i,c} b_i \left(\frac{\Omega R x + V \sin \psi_j}{V_{i,c}} \right) \sqrt{1-\xi^2} \, \frac{dx}{(x_{i'+1} - x_{i'})} \tag{47}$$

In the above equations, b_i, $V_{i,c}$, ξ and $v_{i,j,k}$ are given by equations (32), (33), (35) and (37) respectively. As discussed in the case of the fixed wing, equation (39) can be analytically integrated when U(x), C(x), θ(x) and a(x) are given in the simple form. However, for convenience, expressions with subscripts are presented here, and U(x), C(x), θ(x) and a(x) are represented by values at the middle point, $x_{i',c}$, of the local segment (Refer to equations (40), (41), (42), (43) and (44)). For convenience in numerical calculation, the azimuth angle ψ_j is expressed as follows:

$$\psi_j = \psi_{k,0} + \sum_{\lambda=1}^{j} \Delta\psi_\lambda \tag{48}$$

where $\psi_{k,0}$ and $\Delta\psi$ are the initial azimuth angle of the k-th blade and the azimuth-wise increment of the numerical calculation, respectively.

Similar to the case of the fixed wing, the combination of equation (37) and equations (39) through (48) gives the recurrence equation to solve for Δv_i, if $v_{\ell m}^{j}$ is given as discussed below. The complete procedure and the recurrence equation are presented in the Appendix A-3.

Now let us discuss the inflow angle, ϕ, in equation (45). The flow velocity normal to the rotor rotational plane is generally composed of the induced velocity and the normal component of the rotor forward speed V_N. Furthermore, in the case of the rotary wing, the induced velocity may be generated by the preceding blade in addition to the blade under consideration. For example, in the case of the forward flight of the rotary wing, Fig. 7[1] shows that the air flow at a local station (ℓ, m) on the rotor rotational plane is influenced directly by two blade passages, i.e., by the i-th blade

element of the k-th blade at time j or (i, j, k) blade segment and by the i'-th blade element of the k'-th blade at time j' or (i', j', k') blade segment. Consequently, the normal component of the total flow velocity at a local station (ℓ, m) on the rotor rotational plane is given by the summation of the following: 1) V_N, the normal component of the rotor forward speed (given by equation (46)), 2) $v_{i,j,k}$, the induced velocity generated by the blade under consideration, 3) $v^{j}_{\ell m}$, the entire remaining induced velocity generated by blades that have previously passed through the local station (ℓ, m). Among the three kinds of flow velocity, only the induced velocity, $v_{i,j,k}$, generated by the blade under consideration is related to the lift when momentum balance is considered (Refer to equations (36) and (37)). Dividing the normal component of the total flow velocity by the level forward velocity of the blade element, equation (45) can be obtained.

Here, let us discuss the time-wise variation of the induced velocity on the rotor rotational plane. It is shown in Fig. 8[1] that the rotor rotational plane is assumed to be divided into small elements called stations. The position of each station is given by the coordinate, (ℓ, m). A blade element is shown to proceed on the rotor rotational plane within a small time interval for the case of hovering or steady vertical climb. The blade element is located at a station (ℓ', m') at time t = j-1 with forward speed of $U_{i,j-1,k}$, and it moves to stations (ℓ, m) and (ℓ'', m'') at time t = j and t = j+1 respectively. At time t = j-1 shown in Fig. 8(a), the normal velocity at the station (ℓ', m') is given by the summation of the three components i.e., V_N, $v^{j-1}_{\ell' m'}$ and $v_{i,j-1,k}$. As a small time interval has

passed, the disturbed air at station (ℓ', m') has gone downward and the field in the rotor rotational plane is partially filled with fresh air. The induced velocity at station (ℓ', m') has been changed at time t = j, therefore, while the normal component of the forward velocity, V_N, is still constant (Refer to Fig. 8(b)). By introducing the time-wise changing rate of the induced velocity, the remaining induced velocity, $v^{j}_{\ell' m'}$, at station (ℓ', m') at time t = j can be related to the previous induced velocity i.e. $v^{j-1}_{\ell' m'}$ and $v_{i,j-1,k}$ as follows:

$$v^{j}_{\ell' m'} = C^{j-1}_{\ell' m'} \left(v^{j-1}_{\ell' m'} + v_{i\, j-1\, k} \right) \qquad (49)$$

This time-wise changing rate of the induced velocity, $C^{j-1}_{\ell' m'}$, is called "an attenuation coefficient." Generally, each station has its own attenuation coefficient, and the attenuation coefficient is a function of time. Because the blade element induces the velocity $v_{i,j,k}$ only at the station where the blade element is just passing through, equation (49) can be expressed in a more general form as follows:

$$v^{j}_{\ell m} = C^{j-1}_{\ell m} \left(v^{j-1}_{\ell m} + \sum_{i=1}^{n} \sum_{k=1}^{k} v_{i\, j-1\, k} \cdot \delta_{\ell m} \right) \qquad (50)$$

where $\delta_{\ell m}$ is one if any blade element exists at station (ℓ, m) at t = j-1 and otherwise it is zero. Thus, if the attenuation coefficient $C^{j-1}_{\ell m}$ is known, a combination of equations (39-48) and (50) gives the solution for Δv_i with a given initial condition and a specified blade pitch input. After the value of Δv_i is determined, the induced velocity distribution can be obtained by using equation (37). The lift distribution is given by using equations (37), (38) and (45). Methods to obtain the attenuation coefficient

will be discussed in the next subsection.

In the case of the rotary wing, each assumed elliptical wing is one-sidedly arranged; therefore, when summing up induced velocities of each elliptical wings, upwashes are concentrated outboard of the blade tip as shown in Fig. 6[1]. Although each upwash outside an elliptical wing is negligible, the summation of upwashes outboard of the preceding blade tip is sometimes strong enough to give an effect on the lift distribution of the following blade (Refer to Fig. 9[1]). Consequently, it is necessary to take this into account when estimating the lift distribution of the following blade operating outside the tip vortex of any preceding blade. Remembering the calculation procedure to obtain the value of the induced velocity of each elliptical wing, i.e. Δv_i , it is necessary to omit the upwash only inboard of the blade tip ($x < 1$). This is because in the one-sided arrangement, the angle of attack at any spanwise station of the blade is independent of the tip-side upwash, unlike the inboard upwash. Therefore, after the value of the induced velocity, Δv_i , is determined by omitting the upwash inboard of the blade tip ($x \leq 1$), it is a simple matter to estimate the upwash outboard of the blade tip ($x > 1$) as follows:

$$v(x>1) = \sum_{i=1}^{n} \Delta v_i \left(1 - \frac{|\bar{x}|}{\sqrt{\bar{x}^2 - 1}}\right) \qquad (51)$$

Substituting equation (35) into (51) and using the expression with the suffix, equation (51) becomes

$$v_{ik}(x_i>1) = \sum_{\lambda=1}^{n} \Delta v_\lambda \left(1 - \frac{2x_i - 1 - x_\lambda}{2\sqrt{(x_i-1)(x_i-x_\lambda)}}\right) \qquad (52)$$

where i is larger than n because x_i is located outboard of the blade tip. Thus, when the blade under consideration is operating outside the tip vortex of any preceding blades, equation (52) should be added to the calculation procedure stated before. Furthermore, in equation (50), the induced velocity $v_{\ell m}^{j}$ at station (ℓ, m) should be given by the summation of all velocities induced, not only those induced by the real blade elements ($x \leq 1$, or $i \leq n$) passing through the station, but also those induced by the hypothetical blade elements ($x > 1$, or $i > n$) extending through the tip-side upwash region. In addition to this, similar to the downwash, the time-wise variation of the upwash is expressed by using the attenuation coefficient. Consequently, in this case, equation (50) becomes

$$v_{\ell m}^{j} = C_{\ell m}^{j-1}\left(v_{\ell m}^{j-1} + \sum_{i=1}^{n'}\sum_{k=1}^{b} v_{i\,j-1\,k} \cdot \delta_{\ell m}\right) \qquad (53)$$

where n' is the number of the spanwise partitions of the real and hypothetical blade. $\delta_{\ell m}$ should be considered to be one if any real or hypothetical blade element exists at station (ℓ, m) at time t = j-1; otherwise it should be considered to be zero.

When the pitching or rolling motion of a rotor hub or the blade flapping motion is considered, only the normal velocity component V_N needs to be modified as follows:

$$V_{Nj} = V\sin i + V\cos i \cdot \beta\cos\psi_j + R(x - x_\beta)\dot{\beta} - Rx(q\cos\psi_j + p\sin\psi_j) \qquad (54)$$

It should be realized that the normal component V_N is now the function of time or the azimuth angle in the above equation. Similar to the modification shown in equation (54), more complex hub motion or the blade deformation can also be introduced into the present theory without any essential change of the inflow calculation procedure.

The only difference between the present theory and other numerical calculations comes from the procedure to obtain the lift or induced velocity distribution from the given blade operating condition. Therefore, the calculation procedure is very similar to the usual computer program used for rotor aerodynamic analyses. One sample calculation procedure using the present theory is shown in Fig. 10.

As the present theory is designed to trace a time-wise variation of the lift or of the induced velocity distribution, a suitable numerical method, such as the Runge-Kutta method, should be used in order to solve the blade flapping equation. As an example, the sample blade flapping equation is:

$$I_\beta \ddot{\beta} + M_\beta \Omega^2 \beta + k_\beta (\beta - \bar{\beta}_0) = R^2 \int_{x_\beta}^{1} \ell(x)\, x\, dx \qquad (55)$$

where k_β is spring stiffness at the blade root and $\bar{\beta}_0$ is the preconing or neutral angle. The shear force at the blade root can be obtained by the numerical integration of the lift distribution from the root to the tip along the blade span, and the rotor thrust is obtained by the summation of the shear force at each blade root.

Because the initial induced velocity distribution and the initial blade flapping motion are unknown, a calculation to obtain the initial trimmed condition is required at the beginning of the computation. In the case of the calculation of a steady state, this initial trimmed condition is the solution, and the computation is completed. This initial trimmed condition is usually obtained within eight revolutions of the rotor in hovering, and within five revolutions in forward flight ($\mu > 0.15$). The initial value of the induced velocity is assumed to be zero in the present program. It is not effective in shortening the initial transient period to use the value of the induced velocity $v = \Omega R \sqrt{\frac{C_T}{2}}$ instead of zero. This is because this initial transient period depends mainly on the number of blades, on the development of the wake, and on the damping of the blade flapping motion.

In the actual calculation using equation (53), the following discussion might be useful; as stated before, the axes [ℓ, m] exist on the rotor rotational plane, and the origin is fixed to the inertial space in the case of a steady flight. The axes [i, j, k] are fixed to the blade, and the origin exists on the hub. The small difference between the two reference frames due to the coning angle is ignored. In the case of hovering or vertical climb, the axes [i, j, k] have only a rotating motion relative to the axes [ℓ, m]; therefore, the pie-shaped element is recommended for the station (ℓ, m), for the convenience of the conversion between the two reference frames. In contrast, in the case of the forward flight, the axes [i, j, k] have the transversal motion in addition to the rotating motion relative to the axes [ℓ, m]; therefore, in this case the square element is preferred for the station (ℓ, m).

Attenuation Coefficient

As stated in the previous section, the attenuation coefficient is introduced into the present theory in order to express the time-wise variation of the induced velocity at a local station on the rotor rotational plane. When it is necessary to estimate the induced velocity distribution on another specified plane such as the tail rotor operating plane, the attenuation coefficient should be obtained for that plane using a model which is different from the one presented here. The information obtained for the induced velocity distribution on the rotor rotational plane is usually enough, however, for an analysis of the rotor airloading. Consequently, discussion in this paper is limited to the use of the model in obtaining the attenuation coefficient on the rotor rotational plane.

The attenuation coefficient can be defined as the time-wise changing rate of induced velocities between any arbitrarily chosen time and that time when the blade element passes through the local station (ℓ, m). Therefore, if the exact value of the attenuation coefficient is desired, the physical model used should be very complex, such as the distorted wake vortex theory. Such a complex model requires greater computer time, however; consequently, the balance between accuracy of calculation and complexity of the model is the most important consideration in determining the model to be used in obtaining the attenuation coefficient.

Let us assume steady flight of hovering or of vertical climb, and, remembering the calculation procedure stated in the previous section, let us limit the purpose of the present analysis to the estimation of the lift distribution acting on a rotor blade. It is necessary, then, to know the

induced velocity remaining at station (ℓ, m) only if after the preceding blade has passed, the following blade is located just before the station. The attenuation coefficient at station (ℓ, m) can be given, then, as the ratio of the induced velocities of two times; one, when the preceding blade is passing through the station, and the other, when the following blade is located just before the station. The period between the two moments is given by

$$\Delta t_b = 2\pi/b\Omega \qquad (56)$$

The period Δt_b, in the above equation, can be obtained before the beginning of the calculation, and it is constant during the entire calculation procedure; therefore, during the calculation, the attenuation coefficient is no longer a function of time but a function only of the position of the station.

Furthermore, in the case of the simplest model, the attenuation coefficient is assumed to be uniform over the entire rotor disk. This simplest model was used in the earliest stage of the development of this theory to check the characteristics of the attenuation coefficient. The value of the uniform attenuation coefficient is determined by comparing the theoretical thrust coefficient with the experimental results. Thrust coefficients of a rotor were obtained theoretically by using the Local Momentum Theory, assuming various values of the uniform attenuation coefficient selected between 0.5 and 0.95. The curve of the thrust coefficient versus the uniform attenuation coefficient for a given collective pitch is shown

as a solid line in Fig. 11[2]. The thrust coefficient tends to become small when the value of the uniform attenuation coefficient is increased, because more induced velocity remains on the rotor rotational plane and the angle of attack of the rotor blade decreases. Eventually, the thrust coefficient becomes zero at the point C = 1.0, where all induced velocity remains; therefore, new induced velocity to be balanced with the lift acting on a blade is added to the previous induced velocity until the angle of attack of the blade becomes zero over the entire disk.

The chain line in Fig. 11[2] shows the thrust coefficient obtained by an experimental study[2] using a model rotor. This thrust coefficient, of course, is independent of the attenuation coefficient. The intersection of theoretical (solid) and the experimental (chain) lines gives the value of the uniform attenuation coefficient for a given collective pitch.

In Fig. 12[2], the intersections for various kinds of model rotors are[2,26,35] plotted. As the present uniform attenuation coefficient is defined by the period given by equation (56), the attenuation coefficient depends on the number of blades, i.e., b. Consequently, the equivalent attenuation coefficient C* is used for the lateral axis in Fig. 12[2] in order to unify various attenuation coefficients depending on the number of blade. As a three-bladed rotor is used as the standard in this figure (Fig. 12[2]), the equivalent attenuation coefficient of a b-bladed rotor is defined by

$$C^* = C^{(b/3)} \qquad (57)$$

The next step in estimating the attenuation coefficient is to develop a purely theoretical model. As shown in Fig. 13, the air mass hit by a preceding blade (Blade (A)) at a station (ℓ, m) at time t = j-1 moves downward as time passes. When the following blade (Blade (B)) comes to the same station (ℓ, m) at time t = j, the distance between the air mass and the station (ℓ, m) is shown as Z in Fig. 13. Here it is assumed that the air masses inside the rotor disk move downward with the same constant speed, in other words, the circular disk composed of the air masses moves downward. Such a flow field can be expressed by a semi-infinite vortex cylinder of uniform disk loading, and the circular disk moving downward corresponds to the upper end of the cylinder. Because the flow around the vortex cylinder is determined by using simple vortex theory[23], the attenuation coefficient is given as the ratio of the induced velocity at the rotor rotational plane and that at the upper end of the vortex cylinder, that is, between the two hatched elements shown in Fig. 13. After the blade (B) passes through the station, the process starts again. In other words, it is as if the cylinder suddenly returns to the rotor rotational plane and again begins to move downward. Each station, then, has its own vortex cylinder which moves up and down at each blade passage. Consequently, the attenuation coefficient obtained from the semi-infinite vortex cylinder is a function of two variables. One is the position of the station, i.e., coordinate (ℓ, m), and the other is the length between the upper end of the vortex cylinder and the rotor rotational plane that is shown Z in Fig. 13. In the case of hovering, Z is given by

$$Z = V_0 \Delta t_b \qquad (58)$$

where Δt_b is obtained from equation (56) and v_0 is the downward moving velocity of the upper end of the vortex cylinder; therefore,

$$v_0 = \sqrt{\frac{C_T}{2}}\,\Omega R \qquad (59)$$

The theoretical attenuation coeffient obtained from the semi-infinite vortex cylinder in the case of hovering is shown in Fig. 14[2].

The merits of this theoretical model for the case of hovering are as follows. First, the attenuation coefficent is a function of three variables, the coordinate (ℓ, m), the length Z given by equation (58) and the spanwise position r/R. Therefore, a general chart of the attenuation coefficient can be obtained (Fig. 14[2]) before the beginning of the calculation, and the chart can be used for any single rotor configuration. In addition to this, the flow field around the semi-infinite vortex cylinder can be obtained with very short computer time because of the available analytical solution[23].

Using equations (56), (58) and (59), the attenuation coefficient can be calculated for each model rotor from the given thrust coefficient and the specified position of the station. The result at $r/R = 0.7$ and $r/R = 0.8$ is compared with the previous experimental results in Fig. 12[2]. The reasonable agreement between the two results verifies the theoretical approach presented here. The result shows that the theoretical value at $r/R = 0.75$ may be used as the uniform attenuation coefficient when the simplest calculation is desired.

The use of the theoretical model in hovering flight to obtain the attenuation coefficient can be extended easily to the case of forward flight. Similar to the hovering case, the semi-infinite vortex cylinder with uniform disk loading is used to give the attenuation coefficient. In the case of forward flight, however, the cylinder is assumed to be inclined, the angle of which is given by

$$\chi = \tan^{-1}(\mu/\lambda) \qquad (60)$$

The flow around such an inclined semi-infinite vortex cylinder is known from simple vortex theory[23].

Furthermore, the attenuation coefficient in the case of forward flight is assumed to be uniform over the entire rotor disk. This assumption is based on the following considerations. From a moving axis fixed to a helicopter, a station on the rotor rotational plane appears to move rearward at the same speed as the forward velocity of the helicopter. Thus, every station has come from the upstream and has gone again to the outside of the rotor disk after a finite number of encounters with blade elements. Consequently, it is expected that the attenuation coefficient under the usual operating conditions of forward flight does not play as important a role as under hovering conditions, and therefore, the simpler model might be sufficient.

In the case of forward flight, in addition to the above assumptions, it is also necessary to assume that the period during which two successive blades pass through the same station, is given again by equation (56).

Exactly speaking, the period is no longer given by such a simple expression. The period is shorter on the advancing side ($\psi \fallingdotseq 90^{\circ}$) and is longer on the retreating side ($\psi \fallingdotseq 270^{\circ}$) than the period given as equation (56), because the rotor moves forward. However, as stated above, the simpler model might be sufficient in the case of forward flight, and the rotational speed of the blade is much greater than the forward speed under usual operating condition; therefore, equation (56) gives a sufficient approximation of the period.

Thus, the downward distance of the movement of the vortex cylinder during the period is given by

$$Z = (V\sin i + V\cos i \cdot \beta\cos\psi + v_0)\Delta t_b \qquad (61)$$

where v_0 is the mean induced velocity. Also, the rearward distance X_{cy} is given by

$$X_{cy} = V\cos i \cdot \Delta t_b \qquad (62)$$

Combining the analytical approach[23] to solve the inclined semi-infinite vortex cylinder with equations (56), (60), (61) and (62), the attenuation coefficient can be obtained at any station. Remembering the discussion in the case of hovering, the value at $r/R = 0.75$ and $\psi = 90^{\circ}$ or 270° may be used as the uniform attenuaton coefficient in the case of forward flight. Thus, similar to the case of hovering, the general chart for the theoretical attenuation coefficient in forward flight can be obtained with very short computer time. The result is shown in Fig. 15[2], and it can be used for any single rotor configuration. As will be seen in examples in the next section, this uniform attenuation coefficient based on the above assumptions gives a sufficiently good estimate of the variation of the induced velocity in

forward flight. It is, however, recommended that the attenuation coefficient at low forward flight ($\mu \leq 0.10$) be a function of radius and azimuth angle[24], similar to the case of hovering.

In the case of unsteady flight, the mean induced velocity $\bar{v}_0$ is a function of time. Therefore, the value of $\bar{v}_0$ is given by the averaged induced velocity along the blade span at each instant. Substituting the value of $\bar{v}_0$ into equation (58) or (61), and using the general chart, the attenuation coefficient can be obtained at each instant. The introduction of the time-wise variation of $\bar{v}_0$ into the present theory is nearly equivalent to time-wise change of the pitch of the helikal wake in the vortex theory.

Furthermore, when the rotor hub has unsteady motion, equations (58) and (61) should be modified. For example, when the rotor hub is rolling or pitching, equation (58) becomes

$$Z = \left\{ \bar{v}_0 - R\chi \left(q\cos\psi + p\sin\psi \right) \right\} \Delta t_b \qquad (63)$$

Equation (61) becomes

$$Z = \left\{ V\sin i + V\cos i \cdot \beta\cos\psi - R\chi \left(q\cos\psi + p\sin\psi \right) + \bar{v}_0 \right\} \Delta t_b \qquad (64)$$

Thus, the wake deformation and the interaction between a wake and blade airloading, which are caused by an unsteady hub motion or an unsteady control input, can be easily introduced into the present theory.

Application of the Theory

Hovering Rotor

The lift distribution along a blade span of a hovering rotor was calculated by the theory given in the previous section. Ir the calculation, the number of the blade spanwise partitions is n = 20, and the azimuth-wise increment is $\Delta\psi = 2\pi/b$. The latter may seem too large, but it is allowed because only the steady state with no blade-flapping motion is concerned.

An example of the result is shown in Fig. 16[1]. It is compared with the result obtained from vortex theory[5] and also compared with the experimental result[6] using a model rotor in the wind tunnel. As shown in the figure, the result of the present theory using non-uniform attenuation coefficients is very close to that of the vortex theory and is reasonably close to the experimental result. Even using the constant attenuation coefficient, the present theory gives a good estimation of the blade spanwise lift distribution of a hovering rotor. The computer time of the present theory is at most about 1/10 of that of the vortex theory.

Advancing Rotor

When a rotor is operating in forward flight, the effect of the upwash velocity observed outside the preceding blade-tip must, as stated before, be included in determining the angle of attack of the following blade.

An example of the analysis is shown in Figs. (17), (18), (19), and (20). In the calculation, the number of blade spanwise partitions is n = 20, and azimuth-wise increment is $\Delta\psi$ = 10 deg. The rotor rotational plane is divided into a net of square elements of dimension R/80, the number of which is $\ell \times m$ = 160×320. The lift coefficient is assumed to be zero in the reversed

flow region. The rotor is assumed to have articulated rigid blades and the airloading is coupled with the blade flapping motion. The spanwise and azimuth-wise lift distributions are shown in Fig. 17^{1} and in Fig. 18^{1} respectively, being compared with experimental results[27]. For the sake of comparison, the result obtained by using a vortex theory[28] is also shown in Fig. 18(a). In addition to the lift distribution, the radial distribution of time averaged induced velocity over one rotor revolution is shown in Fig. 19^{1}.. The result of the present theory is compared with that of a simple vortex theory[23]. Furthermore, the distribution of the angle of attack obtained by using the present theory is shown in Fig. 20^{42} . In this figure, the broken line indicates the trace of the intersection of the blade under consideration with the tip vortex of the preceding blade.

As shown in Figs. 17^{1} and 18^{1}, the correlation between the present theory and the experiment is reasonable, even though the constant attenuation coefficient is used for simplicity of calculation. The correlation near the intersections of the blade under consideration with the tip vortex of the preceding blade (Refer Fig. 20) is not, however, as good as the rest. This is because the wake deformation is not considered in the present calculation. Since the lift distribution at the outer part of the blade is more sensitive to the tip vortex positions, the difference between the present theory and the experiment becomes greater at this part.

In addition to the effect of the latest tip vortex, the effects of the older tip vortices on the angle of attack distribution are observed in the result using the present theory (Fig. 20^{42}). These tip vortices cause the variation of the spanwise lift distribution (Fig. 17^{1}), and the high frequency oscillations of the lift (Fig. 18^{1}). The use of the constant attenuation

coefficient tends to emphasize these effects. This is because the variable attenuation coefficient near the intersections of the tip vortices with the blade is smaller than the constant attenuation coefficient. When using the variable attenuation coefficient, the effect of the latest tip vortex alone is remarkable[42].

As shown in Fig. 18(a), the lift obtained by the present theory is more quickly changed than that obtained by vortex theory. This is because the present theory is based on the steady airfoil characteristics and ignores the shed vortices.

Rotor Response due to Rapid Increase of Collective Pitch

A transient response of the rotor thrust and a related induced velocity variation following a rapid collective pitch change have been studied in experimental tests[9,10]. Analyses also have been conducted by introducing an apparent mass associated with the rotor disk into the classical momentum theory[9,10]. Such an analysis, however, requires the use of experimental results to obtain the value of the apparent mass. The approach using the vortex theory is orthodox but it requires much computer time, even though the rigid wake is assumed[29]. In contrast, it is very easy to apply the present theory to this problem and the result can be obtained with much less computer time.

Fig. 21[1] compares an analysis for the case of hovering using the present theory with one using the vortex theory[29]. The aerodynamic thrust shown in the figure means the thrust which does not include the inertia force due to the blade flapping motion.

In the calculation, the mean induced velocity v_0, which is used in equation (58) in order to calculate the moving distance of the vortex cylinder, is determined by two methods: by averaging the induced velocity along the blade span at each instant, and by using the same value used in the calculation for the vortex theory. The solid line shows the results using the former, and the chain line shows the results using the latter. In either way, the results of the present theory are coincident with those of the vortex theory shown by the broken line. This indicates the insensitivity of the transient shape of v_0 to the thrust coefficient.

In the variation of the aerodynamic thrust, the first decrement following a peak results from the blade flapping motion which reduces the blade attack angle. The second decrement following the maximum thrust is due to the development of the wake which increases the induced velocity.

A comparison is shown in Fig. 22[1] of the results of the present theory and those of the classical momentum theory in which the apparent mass of the entire rotor disk has been introduced. The value of the apparent mass associated with the rotor disk is assumed M_0 or $2M_0$, where M_0 is the apparent mass of the impervious disk in the unsteady translation perpendicular to its plane. M_0 is given by

$$M_0 = \frac{8}{3} \rho R^3 \qquad (65)$$

The blade is constrained at the flapping hinge in this calculation in order to compare only the aerodynamic characteristics obtained by using two theories. The irregular curves of the thrust and the induced velocity obtained by using the present theory result from the mutual interference among

the induced velocities of all blades. In the calculation, the number of blade spanwise partitions is n = 20, and azimuth-wise increment is $\Delta\psi$ = 10 deg. The present calculation supports Carpenter's experimental result[10] that the apparent mass of the rotor due to rapid collective pitch change is equal to that of the impervious disk in the normal translation.

Rotor Response due to Sudden Increase of Cyclic Pitch

Fig. 23[2] shows the time history of the inclination of the tip path plane following the step cyclic pitch input into a hovering rotor. The lines show the traces of the point of the unit vector which stands at the hub center normal to the tip path plane. The inclination of the unit vector is obtained from the individual blade flapping angle by using the multiblade coordinates[30] at each instant. As the sample rotor does not have flappin hinge offset nor a spring at the blade root, the coordinate of the steady state is (0, -1). The solid line shows the results of the present theory. The broken line shows the result using the model of constant induced velocity distribution over the entire rotor disk[3,2]. The double chain line indicates the result obtained by the theory[7] based on the momentum balance in the pie-shaped area in the rotor disk. The results obtained by the introduction of the apparent mass of the rotor disk to the theory, in addition to the former theory itself[2], are shown by the chain lines. The results indicated by the chain lines are reasonably close to those of the present theory for various values of Lock number.

In the classical momentum theory, the time-wise variation of the induced velocity is approximated by the inertia term due to the apparent mass of the rotor. Therefore, the difference between the chain line and

the double chain line shows the effect of the time-wise variation of the induced velocity. Furthermore, the difference between the chain line and the broken line indicates the effect of the space wise non-uniformity of the induced velocity distribution, in addition to the time-wise variation. As shown in the figure, the latter difference is small at the beginning of the motion, and the former difference becomes small as time passes.

The reasons are as follows. In the model shown by the broken line, the induced velocity is constant; therefore, when the imbalance of the flapping moment is produced by the step cyclic pitch input, only the blade motion is changed in order to satisfy the new equilibrium. In the model shown by the double chain line, the induced velocity distribution can be changed in addition to the blade flapping motion. However, the induced velocity distribution is given by the condition at the terminal steady state[7]; therefore, the induced velocity has developed to the terminal value even at the very beginning of the transient motion. In the model shown by the chain line, due to the inertia term associated with the apparent mass, the induced velocity distribution is not changed as rapidly. Consequently, at the beginning of the transient motion, the imbalance of the flapping moment is satisfied largely by the change of the blade flapping motion. The induced velocity, then, develops to the steady state. In the case of the very low frequency response of the rotor, therefore, the effect of the apparent mass may be neglected, and the model shown by the double chain line can give a good approximation of the rotor inclination[7].

The step cyclic pitch response of the advancing rotor is shown in Fig. 24[1]. The time histories of the thrust coefficient and the coning angle are indicated in Fig. 24(a)[1]. The inclination of the tip path plane is shown in Fig. 24(b)[1]. The small high-frequency variation observed in the thrust coefficient results primarily from the non-uniformity of the induced velocity distribution, caused primarily by the tip vortex of the preceding blade. The effect of the inclination of the tip path plane on the thrust is shown as the low frequency variation in the figure. In the calculation, the number of the spanwise partitions is n = 20, and the azimuth-wise increment is $\Delta\psi$ = 10 deg.

A few more applications of the Local Momentum Theory have been tried. For example, the tandem rotor in yawed flight and the coaxial rotor are analyzed in Ref. 31. The gust response of a single rotor is studied in Ref. 21.

The new hovering model including the wake deformation

Calculation model

A recent extension of the Local Momentum Theory to include the wake deformation of steady hovering flight is presented in this section. Although, as discussed in the previous section, the results using the Local Momentum Theory showed good correlation with a few experimental cases, this extension of the theory was necessary in order to analyze the airloading distributions measured by a laser velocimeter.[33,34]

The wake deformation of a hovering rotor is separated into spanwise deformation and axial deformation. The spanwise wake deformation includes the contraction and rollup of the vortices. The axial wake deformation is

the axial deviation from the rigid helical wake position. In the Local Momentum Theory, the spanwise wake deformation is equivalent to the spanwise movement of a local station on the rotor rotational plane. In order to express the axial wake deformation, a new model to give a corresponding attenuation coefficient was developed. Because of the effect of the tip vortex on a spanwise lift distribution is dominant among all the wake components, the model of the present theory was developed primarily to trace the behavior of the tip vortex. Fig. 25(a) and Fig. 25(b) show the side view and top view of the tip vortex. The tip vortex No. 1 in Fig. 25(a) is shed from the blade under consideration (blade (A)) at position P_1 at time $t = j$. The tip vortex No. 2 was shed from the preceding blade (blade (B)) at position P_1 at time $t = j-1$, and is located at position P_2 at time $t = j$. The period between $t = j-1$ and $t = j$ is the period during which two neighboring blades successively pass through the same position of the rotor rotational plane, that is, Δt_b given as equation (56). During the period Δt_b, the tip vortex No. 2 moves from P_1 to P_2. Following the motion of the tip vortex No. 2, a station on the rotor rotational plane moves from r_1 to r_2 during the period, where r_i is a radial position of the tip vortex No. i. Similarly, each station moves from r_{i-1} to r_i during the period following the motion of the tip vortex No. i. The positions of the tip vortices are given by a generalized wake model[16,17,18,35]:

$$x_T = K_4 + (1 - K_4)\, e^{-K_3 \phi} \tag{66}$$

$$z_T \begin{cases} = K_1 \phi & 0 \le \phi < \frac{2\pi}{b} \\ = K_1 \left(\frac{2\pi}{b}\right) + K_2 \left(\phi - \frac{2\pi}{b}\right) & \frac{2\pi}{b} \le \phi \end{cases} \tag{67}$$

where x_T and z_T are the axial and radial non-dimensional positions of the tip vortices. Using equation (66), the radial position of the tip vortex No. i is given as

$$r_i = R\{K_4 + (1-K_4)e^{-K_3\phi_i}\} \qquad (68)$$

$$\phi_i = \frac{2\pi}{b}\cdot(i-1) \qquad (69)$$

Outside the rotor disk (r > R), each of the stations moves a distance equal to that between r_1 and r_2 toward the blade root in order to avoid making a gap between neighboring stations. At the inner area of the rotor ($r \leq RK_4$), the stations don't move, because no tip vortex moves into this area (Refer to equation (66)). Therefore, the positions of the stations in the inner area are coincident with those of the rigid wake model. The parameters K_1, K_2, K_3 and K_4 in equations (66), (67) and (68) are determined by experimental data using flow visualization techniques. There are three available generalized wake models, one proposed by Landgrebe[16],,one by Kocurek and Tangular[17], and one by Kocurek, Berkowitz and Harris[35]. In this paper, the second model is most frequently used, because of the applicability over wide range variations of rotor geometry, and because of the convenience of comparison with other computer codes.

As each station moves, a part of the following blade (the hatched area in Fig. 25(b)) operates in the upwash region generated by the preceding blade, even in the hovering case. Therefore, it is necessary to calculate the upwash distribution outside the blade tip in addition to the downwash distribution along the blade. The upwash or downwash distributions are calculated at each station by using equation (37), equation (39) through (48) and equation (52).

The new model was also developed to take the wake deformation into account and to obtain the attenuation coefficient at the upwash region. Fig. 26 shows the new model which is composed of a vortex ring and a semi-infinite vortex cylinder. The vortex ring represents the tip vortex nearest to the rotor rotational plane, and the vortex cylinder represents the remaining tip vortices. The vortex cylinder is made of the continuous vortex, the strength of which is equal to that of the axially averaged tip vortices[23]. The strength of the vortex ring is equal to that of the tip vortex. Fig. 26(a) shows that the preceding blade passes through a local station at time $t = j-1$. The vortex ring is localed on the rotor rotational plane, and the top of the vortex cylinder is located at the position of the second tip vortex. The distance between the top of the vortex cylinder and the rotor rotational plane is Z_2. Fig. 26(b) shows that the following blade comes just before the station at time $t = j$. During the period between time $t = j-1$ and $t = j$, the vortex ring and the vortex cylinder move downward and radially contract. Using equation (67), the vertical position Z_i is given by

$$Z_i \begin{cases} = RK_1\phi_i & i \le 2 \\ = R\left\{K_1\left(\frac{2\pi}{b}\right) + K_2\left(\phi_i - \frac{2\pi}{b}\right)\right\} & i > 2 \end{cases} \qquad (70)$$

where ϕ_i is given by equation (69). The radius of the vortex ring is equal to that of the tip vortex nearest to the rotor rotational plane (Refer to Fig. 26(b)). For simplicity, the radius of the vortex cylinder is assumed to be equal to that of the vortex ring instead of the corresponding tip vortex radius. This leads, however, to an overestimation of the radius of the vortex cylinder because of the contraction of the tip vortices as shown in Fig. 25(a). The radii of the vortex ring and the vortex cylinder are given as equation (68).

The attenuation coefficient is defined by the changing rate of induced velocities at a station (ℓ, m) between time t = j and t = j-1. In the present model including the wake deformation, the station (ℓ, m) moves from position r_{i-1} to position r_i on the rotor rotational plane during this period. Consequently, the attenuation coefficient of that station is given as

$$C_{\ell m}^{j-1} = v_{\ell m}^{j} / v_{\ell m}^{j-1} \qquad (71)$$

where $v_{\ell m}^{j-1}$ is the induced velocity at position r_{i-1} on the rotor rotational plane at time t = j-1, and $v_{\ell m}^{j}$ is the induced velocity at position r_i on the rotor rotational plane at time t = j. Because the station at the inner part of the blade ($r \leq RK_4$) does not move, the attenuation coefficient of that station is given as the changing rate of the induced velocities at the same radial position between time t = j and t = j-1. The stations which are located between positions r_2 and R at time t = j were situated outside the rotor disk (r > R) at time t = j-1. Therefore, when determining the attenuation coefficients of these stations by using equation (71), the induced velocity $v_{\ell m}^{j-1}$ is calculated outside the rotor disk. If the old model, which is composed of the vortex cylinder alone (Refer to Fig. 13), is used, the induced velocity $v_{\ell m}^{j-1}$ is zero outside the rotor disk, and it is impossible to define the attenuation coefficients of these stations. Consequently, the discrete vortex was introduced into the present model.

In the Landgrebe wake model and in the Kocurek and Tangular wake model, the parameters K_1, K_2, and K_3 in equations (66), (67), (68) and (70) are

functions of a thrust coefficient[16,17]. In the present method, those parameters are calculated at each time step by using the value of a thrust coefficient. There is an analytical solution[23] for the induced velocity around the vortex cylinder or the vortex ring. Based on this solution, general tables of the induced velocity are constructed for the vortex ring and for the vortex cylinder, before the start of the calculation. The attenuation coefficient is calculated at each time step from these general tables by using equation (71). The entire calculation is completed when the thrust coefficient reaches a steady state. The calculation procedure of the present theory is shown by Fig. 27.

Calculation Results

A comprehensive study has been conducted to check this extended Local Momentum Theory. The spanwise lift distributions for five different rotors were calculated by this theory. The results were compared with experimental data and with those obtained by using other analyses. Table 1 shows the geometrical characteristics and the operating conditions of sample rotors used in this study (see also Refs. 26, 34, 36-38). Three of them are model rotors, and two are full scale rotors.

Two computer codes of the prescribed wake vortex theory were used in this study, the AMI lifting surface program[22], and the UTRC lifting line program[18]. In the present theory and the UTRC code, the lift curve slope of airfoil sections is given as

$$a = a_0/\sqrt{1-M^2} \qquad (72)$$

$$a_0 = 6.05 \quad (1/\text{rad.}) \qquad (73)$$

M is the Mach number of the airfoil section and it is given as

$$M = \Omega R x_i / a_s \qquad (74)$$

where a_s is the speed of sound. The above equations are based on Refs. (39) and (40). Because the angles of attack of the airfoil sections are far below the stall angles in all experimental cases presented here, the above simple relations are applicable.

The results are shown in Figs. 28 through 37. A comparison of the present theory with the AMI code and with the first experiment[34] when using the Kocurek and Tangular wake model is presented in Fig. 28. The experimental result was obtained using a laser velocimeter to measure the bound circulation. Although there are differences, especially around x = 0.8, the result obtained by using the present theory shows good correlation with that of the AMI code. The experimental data show a higher lift peak at the blade tip than either theoretical estimation. This is probably caused by the existence of a larger wake deformation than estimated using the generalized wake model[41], rather than by modeling errors in the two theories. The same experimental result[34] was analyzed by using the Landgrebe wake model as shown in Fig. 29. In addition to the comparison of the present theory with the AMI code, the result obtained by the UTRC code is also presented. The three theoretical results are very similar. Comparing Fig. 29 with Fig. 28, the Landgrebe wake model gives better estimation than the Kocurek and Tangular wake model in this experimental case. The difference of lift distributions between the two wake models is, however, very small.

In addition to the results shown in Fig. 29, the results using the previous rigid wake model of the Local Momentum Theory and using blade element theory with a uniform induced velocity are shown in Fig. 30. The uniform iduced velocity is given as $v_0 = \Omega R\sqrt{\frac{C_T}{2}}$ where the thrust coefficient is equal to that of the AMI code. For convenience, the lift curve slope of the airfoil section is again given as equations (72), (73) and (74) in the rigid wake model of the Local Momentum Theory and in blade element theory. It is apparent that the present extension of the Local Momentum Theory improves the capability of estimating the lift distribution near the blade tip.

An analysis of the second experimental case using the Kocurek and Tangular wake model is shown in Fig. 31. The experimental data were measured by a flight test using H-34 rotor (Table 4 in Ref. 36). Although the correlation between the present theory and the AMI code is not as good as the first experimental case shown in Figs. 28 and 29, it is reasonable. Compared with either theoretical prediction, the experimental data show a lower value of the lift distribution at the inner part of the blade.

Results of another analysis of the second experiemental case[36] using the Landgrebe wake model are shown in Fig. 32. The previous results, shown in Figs. 28 through 31, were obtained by using the collective pitch input mode for all codes, in which the measured value of the collective pitch is given to the computer program. In this experimental case, the collective pitch input mode showed poor correlation between the UTRC code and the AMI code. Therefore, the thrust coefficient input mode, in which the value of the thrust coefficient is given to the computer program, was also tried. The results using the collective pitch input mode and the thrust coefficient

input mode are shown by the double chain line and by the broken line, respectively. The thrust coefficient input mode gives better correlation, but a measureable difference between the two computer codes still exists near the blade tip. Because the same thrust coefficient is used in the AMI code and in the UTRC code when using the thrust coefficient input mode, the difference between these two results comes from the difference between lifting surface and lifting line, and also comes from the difference between the numerical methods to calculate the thrust coefficient. In this experimental case, the tip vortices generated by the preceding blade are closer to the following blade than in the first experimental case shown in Figs. 28 through 30. Therefore, the airloading distribution is more sensitive to the tip vortex positions, which depend on the thrust coefficient. This is the primary reason for the poor correlation between the two computer codes when using the collective pitch input mode.

The results of the third experimental case, analyzed by the Kocurek and Tangler wake model, are shown in Fig. 33. The experimental data were obtained by a UH-1A helicopter[37]. The correlation between the present theory and the AMI code is very good. The correlations between the experiment and the present theory or the AMI code are good. It is also apparent that the present extension of the Local Momentum Theory shows good improvement in the capability of estimating the lift distribution.

The analyses of the fourth experimental case[26] using the Kocurek and Tangler wake model are presented in Figs. 34 and 35. Fig. 34 shows the results using the collective pitch input mode. The experimental data,

however, show poor correlation with the theoretical estimations. Ironically, the previous rigid wake model gives better correlation with the experiment in this input mode (Refer to Fig. 16). When using the thrust coefficient input mode, the present theory and the AMI code show good correlation with the experiment as shown in Fig. 35. The airloading distribution near the blade tip can be estimated only when using the distorted wake model.

The fifth experimental case[38] was analyzed by the Kocurek and Tangular wake model. The results using the collective pitch input mode and the thrust coefficient input mode are shown in Figs. 36 and 37, respectively. Again, only the thrust coefficient input mode of the present theory or of the AMI code show good correlation with the experiment. The correlation between the present theory and the AMI code are reasonable in both input modes.

Reviewing analyses of the five experimental cases, correlation between the present theory and the AMI code is always good. However, the correlation near a blade tip is not as good as that of the inner part of the blade, nor it is as good when the aspect ratio of the blade becomes smaller, or when the tip vortices of the preceding blade are closer to the blade under consideration. These tendencies of the correlation are due to the simplicity of the present model. An improvement of the attenuation coefficient at the upwash region might be effective in obtaining a better correlation.

The difference between the results obtained using the AMI code and the UTRC code is sometimes greater than the difference between those obtained using the AMI code and the present theory. The experimental results fluctuate around the three theoretical results, and it is difficult to determine which computer code gives the best correlation with the experiments. There-

fore, the development of a more complicated model of the present theory, which might make it possible to obtain a better correlation with the AMI code alone, is not necessary at present.

The computer time required for each of the three codes to obtain the results shown Figs. 29 and 32 is given in Table 2. These calculations were conducted under the same condition by using CDC-7600 at Ames Research Center. The variation of the computer time of the UTRC code in the case of Fig. 32 is due to the difference of the convergence speeds of the iteration included in this code. The computer time required by the present theory is less than 1/15 of that of the UTRC code, and less than 1/60 of that of the AMI code.

The experimental data of the fourth and the fifth cases are very different from the theoretical estimation obtained by the present theory and by the AMI code when using the collective pitch input mode. This may be due to elastic torsion deflection of the blade. When the thrust coefficient input mode is used, however, the results obtained from using the distorted wake model show the best correlation with the experiments. In the other three experimental cases, the results obtained using the present theory and the AMI code show reasonable correlation with the experimental results, even when the collective pitch input mode is used.

Conclusion

The fundamentals of the Local Momentum Theory were presented to make clear the boundaries of this theory and to assist to make a computer program using this theory. Then, an extension of this theory to include the effect of the rotor wake contraction in hovering flight was presented. This

extended Local Momentum Theory was compared with a prescribed wake vortex theory. The results indicated that the extended Local Momentum Theory has the capability of achieving a level of accuracy similar to that of a prescribed wake vortex theory over wide range variations of rotor geometrical parameters. It was also shown that the analytical results obtained using either theory were in reasonable agreement with experimental data. The computer time required by the present theory was less than 1/15 of that of the prescribed wake vortex theory. Consequently, this extended Local Momentum Theory is especially effective when calculations are required for numerous cases.

Acknowledgement

The work to extend the Local Momentum Theory to the distorted wake model of hovering has been conducted during the period of a National Research Council Resident Research Associateship, at Ames Research Center, National Aeronautics and Space Administration, Moffett Field, CA. The author wishes to thank the following persons for their contributions to this paper: Professor Akira Azuma, University of Tokyo, Tokyo, Japan from whom the author received the idea of the extension of the theory; Dr. Wayne Johnson, Ames Research Center, National Aeronautics and Space Administration, Moffett Field, California who reviewed this paper; and Mr. Henry Jones, Ames Research Center who assisted to use the AMI code and the UTRC code.

Appendix A-1

Recurrence Equation to Give the Induced Velocity Distribution in the Case of the Fixed Wing

In this section, a sample procedure is presented to derive a recurrence equation from equation (28). This recurrence equation is used to solve the induced velocity distribution along the fixed wing span.

For simplicity, it is assumed that the wing has a rectangular planform, no twist angle and the same airfoil section along the span, that is, the chord, the geometrical angle of attack and the slope of the lift coefficient are constant along the wing span. Furthermore, the assumed elliptical wings are onesidedly arranged as shown in Fig. 2. In addition to this, the difference of the span length is constant between neighboring elliptical wings, that is, $\Delta\eta = \eta_{j+1} - \eta_j$ is constant.

Substituting j = 1 into equation (28), equation (28) becomes

$$\ell_1 = \int_{-1}^{-\eta_2} \tfrac{1}{2} \rho V^2 C a \left(\theta - \Delta v_1 / V\right) \frac{d\eta}{(1-\eta_2)}$$

$$= 2 \bar{m}_1 \Delta v_1 \qquad (A.1-1)$$

Also, in the case of j = 1, equation (21) becomes

$$\bar{m}_1 = \int_{-1}^{-\eta_2} \rho b_1 V \sqrt{1-\eta^2} \frac{d\eta}{(1-\eta_2)} \qquad (A.1-2)$$

Substituting equation (A.1-2) into (A.1-1) and performing the integration, the following equation can be obtained:

$$\Delta v_1 = V\theta \Big/ \left\{ 1 + \frac{4b \cdot g(1,\eta_2)}{ac\Delta\eta} \right\} \qquad (A.1-3)$$

where

$$\Delta\eta = 1 - \eta_2 \qquad (A.1\text{-}4)$$

In equation (A.1-3), g(x, y) comes from the integration and it is generally defined by

$$g(x, y) = \frac{1}{2}\left(x\sqrt{1-x^2} + \sin^{-1}x - y\sqrt{1-y^2} - \sin^{-1}y\right) \qquad (A.1\text{-}5)$$

Therefore, $g(1, \eta_2)$ is given as

$$g(1, \eta_2) = \frac{1}{2}\left(\frac{\pi}{2} - \eta_2\sqrt{1-\eta_2^2} - \sin^{-1}\eta_2\right) \qquad (A.1\text{-}6)$$

Similar to the case of j = 1, the following can be obtained from equations (21) and (28) in the case of $j \geq 2$:

$$\Delta v_j = \left\{\theta V - \sum_{i=1}^{j-1}\Delta v_i - \frac{4}{ac\Delta\eta}\sum_{i=1}^{j-1} b_i \Delta v_i \cdot G(\eta_j, \eta_{j+1}, b_i)\right\} \Big/ \left\{1 + \frac{4b_j}{ac\Delta\eta} G(\eta_j, \eta_{j+1}, b_j)\right\} \qquad (A.1\text{-}7)$$

where

$$G(\eta_j, \eta_{j+1}, b_i) = \int_{-\eta_j}^{-\eta_{j+1}} \sqrt{1 - \left(\frac{b}{b_i}\right)^2 (\eta - \eta_{oi})^2}\, d\eta \qquad (A.1\text{-}8)$$

Performing the integration in the above equation and using equation (A.1-4), equation (A.1-7) becomes

$$G(\eta_j, \eta_{j+1}, b_i) = \left(\frac{b_i}{b}\right) g(\zeta_j, \zeta_{j+1}) \qquad (A.1\text{-}9)$$

where

$$\zeta_j = \left(\frac{b}{b_i}\right)(\eta_j + \eta_{oi}) \qquad (A.1\text{-}10)$$

$$\zeta_{j+1} = \left(\frac{b}{b_i}\right)(\eta_{j+1} + \eta_{oi}) \qquad (A.1\text{-}11)$$

As the one-sided arrangement is assumed here, η_{oi} is given by

$$\eta_{oi} = (i-1)\cdot\Delta\eta/2 \qquad (A.1\text{-}12)$$

In summary, the initial value $\Delta\Gamma_1$ is given by equations (A.1-3), (A.1-4) and (A.1-5). The remaining $\Delta\Gamma_j$ ($j \geq 2$) is given by equations (A.1-4), (A.1-5) and from (A.1-7) through (A.1-12). After the values of $\Delta\Gamma_j$ ($j = 1 \sim n$) have been obtained, the induced velocity distribution and the lift distribution can be obtained by using equations (27) and (17), respectively.

Appendix A-2

Momentum Balance of Each Elliptical Wing Operating in a Sheared Flow

In this section, a momentum balance of each elliptical wing operating in the sheared flow shown in Fig. 5[1] is discussed. As defined in the subsection of the rotary wing, an elliptical wing means a wing which has an elliptical circulation distribution along the span. The horizontal velocity for the elliptical wing is linearly increased from the root to the tip along the wing span as given by equation (29). The trailing vortices shed from each elliptical wing are straight, perpendicular to the wing span, and they are horizontally extended to infinity. The elliptical circulation distribution of the wing can be expressed by the following equation using a constant C_Γ :

$$\Gamma(x) = C_\Gamma \sqrt{1-\xi^2}$$

$$= C_\Gamma \sqrt{1-\{(2x-1-x_i)/(1-x_i)\}^2} \qquad (A.2-1)$$

where the relation between ξ and x is given as equation (35). Using the Biot-Savart relation, the induced velocity inside the wing span is given as

$$\Delta v_i = \frac{1}{4\pi R}\int_{x_i}^{1}\frac{d\Gamma(x')}{x-x'} \qquad (A.2-2)$$

Substituting equation (A.2-1) into (A.2-2) and performing the integration, equation (A.2-2) becomes

$$\Delta v_i = C_\Gamma/\{2R(1-x_i)\} \qquad (A.2-3)$$

Substituting $C_\Gamma = 2R(1-x_i)\Delta v_i$ from the above equation into (A.2-1), equation (A.2-1) is rewritten as

$$\Gamma(x) = 2R(1-x_i)\Delta v_i \sqrt{1-\xi^2}$$

$$= 2R(1-x_i)\Delta v_i \sqrt{1-\left\{(2x-1-x_i)/(1-x_i)\right\}^2} \qquad (A.2-4)$$

The spanwise lift distribution of each elliptical wing, i.e., $(l_i(x))_{elp}$ is given as

$$(l_i(x))_{elp} = \rho U \Gamma \qquad (A.2-5)$$

Substituting equations (29) and (A.2-4) into (A.2-5), equation (A.2-5) becomes

$$(l_i(x))_{elp} = (2\rho V_{i,c} R (1-x_i)\Delta v_i)(U/V_{i,c})$$

$$\times \sqrt{1-\xi^2} \qquad (A.2-6)$$

The total lift of each elliptical wing L_i can be given as

$$L_i = \int_{x_i}^{1} \rho U(x)\Gamma(x) R\, dx \qquad (A.2-7)$$

Substituting equations (29) and (A.2-4) into the above equation, L_i can be expressed by

$$L_i = 2 m_i \Delta v_i \qquad (A.2-8)$$

where

$$m_i = \rho\pi\left\{R(1-x_i)/2\right\}^2 V_{i,c} \qquad (A.2-9)$$

$$V_{i,c} = V\sin\psi + \Omega R(1+x_i)/2 \qquad (A.2-10)$$

Appendix A-3

Recurrence Equation to Give the Induced Velocity Distribution in the Case of the Rotary Wing

In this section, a sample procedure is presented to derive a recurrence equation from equations (37) and (39)-(47). The recurrence equation is used to solve the spanwise induced velocity distribution of the rotary wing.

For simplicity, it is assumed that a rotor blade has a rectangular planform, no twist angle and the same airfoil section along the span, that is, the chord, the pitch angle and the slope of the lift coefficient are constant along the blade span. Furthermore, it is assumed that the difference of the span length is constant between neighboring elliptical wings, that is, $\Delta\chi = \chi_{i,i+1} - \chi_{i,i}$ is constant.

Using equation (35) and replacing x in equation (47) with ξ, equation (47) becomes

$$\overline{m}_i = \frac{\rho R}{2\Delta\chi}(1-\chi_i)^2 \int_{\xi_{i,i}}^{\xi_{i,i+1}} (C_i\xi + V_{i,c})\sqrt{1-\xi^2}\,d\xi \qquad (A.3-1)$$

where

$$C_i = \frac{\Omega R}{2}(1-\chi_i) \qquad (A.3-2)$$

$$\xi_{i,i+1} = \{2\chi_{i+1} - (1+\chi_i)\}/(1-\chi_i) \qquad (A.3-3)$$

$$\xi_{i,i} = \{2\chi_i - (1+\chi_i)\}/(1-\chi_i) \qquad (A.3-4)$$

$$\Delta\chi = \chi_{i+1} - \chi_i \qquad (A.3-5)$$

and where $V_{i,c}$ is given as equation (33). Performing the integration in equation (A.3-1), $\overline{m}_i$ can be given as

$$\overline{m}_i = \frac{\rho R}{2\Delta\chi}(1-\chi_i)^2 H(\xi_{i,i+1}, \xi_{i,i}) \qquad (A.3-6)$$

In the above equation, H(x, y) comes from the integration and it is defined by

$$H(x,y) = -\frac{c_i}{3}\left\{(1-x)^{3/2} - (1-y)^{3/2}\right\} + V_{i,c}\cdot g(x,y) \qquad (A.3\text{-}7)$$

where g(x, y) is given as equation (A.1-5). Replacing $\overline{m}_i$ in equation (39) with (A.3-6), substituting i' = 1 into equation (39) and using equations (37), (45) and (A.3-5), ΔV_1 can be obtained,

$$\Delta V_1 = \left(\theta U_1 - V_N - V_{1m}^{\dagger}\right) \Big/ \left\{1 + \frac{2R(1-x_1)^2}{ac\Delta x\, U_1}\cdot H(\xi_{1,2}, \xi_{1,1})\right\} \qquad (A.3\text{-}8)$$

where U_1, V_N, $H(x,y)$, $\xi_{1,2}$ and $\xi_{1,1}$ are given by equations (40), (46), (A.3-7), (A.3-3) and (A.3-4), respectively.

Similar to i' = 1, the following can be obtained in the case of i' ≥ 2:

$$\Delta V_{i'} = \left[\theta U_{i'} - V_N - V_{1m}^{\dagger} - \sum_{i=1}^{i'-1}\left\{1 + \frac{2R(1-x_i)^2}{ac\Delta x\, U_{i'}}\cdot H(\xi_{i,i'+1}, \xi_{i,i'})\right\}\Delta V_i\right] \Big/ \left\{1 + \frac{2R(1-x_{i'})^2}{ac\Delta x\, U_{i'}}\cdot H(\xi_{i',i'+1}, \xi_{i',i'})\right\} \qquad (A.3\text{-}9)$$

where $U_{i'}$, V_N, H(x, y), $\xi_{i,i'+1}$ and $\xi_{i,i'}$ are given by equations (40), (46), (A.3-7), (A.3-3) and (A.3-4), respectively.

In summary, when $\Gamma_{tm}^{\dagger}$ is known, the initial value $\Delta\Gamma_1$ is given by equation (A.3-8), and the remaining $\Delta\Gamma_{i'}$ ($i' \geq 2$) is given by equation (A.3-9). After the values of $\Delta\Gamma_{i'}$ ($i' = 1 \sim n$) have been determined, the induced velocity distribution and the lift distribution can be obtained by using equations (37) and (38) respectively. The upwash distribution outside the blade tip can be obtained by using equation (52).

References

1. Azuma, A. and Kawachi, K.: "Local Momentum Theory and Its Application to the Rotary Wing," Journal of Aircraft, Vol. 16, No. 1, January 1979, pp. 6-14.

2. Azuma, A. and Kawachi, K.: "Local Momentum Theory and Its Application to the Rotary Wing," AIAA Paper 75-865, AIAA 8th Fluid and Plasmadynamic Conference, Hartford, CT, June 16-18, 1975.

3. Stepniewski, W. Z.: "Rotary-Wing Aerodynamics Volume I - Basic Theories of Rotor Aerodynamics (With Application to Helicopters)," NASA Contractor Report 3082, 1979, pp. 219-260.

4. Glauert, H.: "A General Theory of the Autogyro," British Aeronautical Research Council, R&M 1111, 1926.

5. Klemin, A.: "Principles of Rotary-Wing Aircraft," AERO Digest, May 1 and June 1, 1945.

6. Shupe, N. K.: "A Study of the Dynamic Motions of Hingeless Rotored Helicopters," United States Army Electronics Command ECOM-3323 (AD 713402), 1970.

7. Azuma, A. and Nakamura, Y.: "Pitch Damping of Helicopter Rotor with Nonuniform Inflow," Journal of Aircraft, Vol. 11, No. 10, Oct. 1974, pp. 639-646.

8. Ormiston, R. A. and Peters, D. A.: "Hingeless Helicopter Rotor Response with Nonuniform Inflow and Elastic Blade Bending," Journal of Aircraft, Vol. 9, No. 10, Oct. 1972, pp. 730-736.

9. Rebont, J., Valensi, J. and Soulez-Lariviere: "Response of a Helicopter Rotor to an Increase in Collective Pitch for the Case of Vertical Flight," NASA TTF-55, 1961.

10. Carpenter, P. J. and Fridovich, B.: "Effect of a Rapid Blade - Pitch Increase on the Thrust and Induced-Velocity Response of a Full-Scale Helicopter Rotor," NACA TN 3044, 1953.

11. Crews, S. T., Hohenemser, K. H. and Ormiston, R. A.: "An Unsteady Wake Model for a Hingeless Rotor," Journal of Aircraft, Vol. 10, No. 12, December 1973, pp. 758-760.

12. Peters, D. A.: "Hingeless Rotor Frequency Response with Unsteady Inflow," NASA SP-352, pp. 1-12.

13. Ormiston, R. A.: "Application of Simplified Inflow Models to Rotorcraft Dynamic Analysis," Journal of the American Helicopter Society, Vol. 21, No. 3, July 1976, pp. 34-37.

14. Banerjee, D., Crews, S. T., Hohenemser, K. H. and Yin, S. K.: "Indentification of State Variables and Dynamic Inflow from Rotor Model Dynamic Tests," Journal of the American Helicopter Society, Vol. 22, No. 2, April 1977, pp. 28-36.

15. Banerjee, D., Crews, S. T. and Hohenemser, K. H.: "Parameter Identification Applied to Analytic Hingeless Rotor Modeling," Journal of the American Helicopter Society, Vol. 24, No. 1, January 1979, pp. 26-32.

16. Landgrebe, A. J.: "The Wake Geometry of a Hovering Helicopter Rotor and Its Influence on Rotor Performance," Journal of the American Helicopter Society, Vol. 17, No. 2, Oct. 1972, pp. 3-15.

17. Kocurek, J. D. and Tangler, J. L.: "A Prescribed Wake Lifting Surface Hover Performance Analysis," Journal of the American Helicopter Society Vol. 22, No. 1, January 1977, pp. 24-35.

18. Landgrebe, A. J.: "An Analytical and Experimental Investigation of Helicopter Rotor Hover Performance and Wake Geometry Characteristics " USAAMRDL TR 71-24, Eustis Directorate, U. S. Army Air Mobility Research and Development Laboratory, Ft. Eustis, Virginia, June 1971.

19. Prandtl, L. and Tietjens, O. G.: "Fundamentals of Hydro- and Aeromechanics," McGraw-Hill, New York, 1934.

20. Multhopp, H.: "Die Berechnung der Auftriebsverteilung vor Tranglfugeln," Luftfahrt Forshung, Bd. 15, 1938, pp. 153-169; transl. as Aeronautical Research Council Rept. 8516.

21. Azuma, A. and Saito, S.: "Study of Rotor Gust Response by Means of the Local Momentum Theory," Paper No. 27, Fifth European Rotorcraft and Powered Lift Aircraft Forum, September 4-7, 1979.

22. Summa, J. M. and Clark, D. R.: "A Lifting-Surface Method for Hover/Climb Airloads," Preprint No. 79-3, American Helicopter Society 35th Annual National Forum Proceedings, May 21-23, 1979.

23. Castles, W., Jr., and De Leeuw, J. H.: "The Normal Component of the Induced Velocities in the Vicinity of a Lifting Rotor and Some Examples of Its Application," NACA Rept. 1184, 1954, (supersedes NACA TN 2912).

24. Kawachi, K.: "Blade Flapping Behavior of Articulated Rotors at Low Advance Ratio," Japan Society for Aeronautical and Space Sciences Aircraft Symposium Proceedings, Nov. 1976, pp. 134-137.

25. Ichikawa, T.: "Linearized Aerodynamic Theory of Rotor Blades (III)," National Aerospace Lab. of Japan, NAL TR-100, 1966.

26. Mayer, J. R., Jr. and Falabella, G., Jr.: "An Investigation of the Experimental Aerodynamic Loading on a Model Helicopter Rotor Blade," NACA TN 2953, 1953.

27. Sheiman, J. and Ludi, L. H.: "Qualitative Evaluation of Effect of Helicopter Rotor-Blade Tip Vortex on Blade Airloads," NASA TN D-1637, 1963.

28. Johnson, W. and Scully, M. P.: "Aerodynamic Problems in the Calculation of Helicopter Airloads," Symposium on Status of Testing and Model Techniques for V/STOL Aircraft, American Helicopter Society, Oct. 1972.

29. Segel, L.: "A Method for Predicting Nonperiodic Air Loads on a Rotary Wing," Journal of Aircraft, Vol. 3, Nov.-Dec. 1966, pp. 541-548.

30. Hohenemser, K. H. and Yin, S. K.: "Some Application of the Method of Multiblade Coordinates," Journal of the American Helicopter Society, Vol. 17, No. 3, July, 1972, pp. 3-12.

31. Azuma, A., Saito, S., Kawachi, K. and Karasudani, T.: "Application of the Local Momentum Theory to the Aerodynamic Characteristics of Multi-Rotor Systems," Vertica, Vol. 3, No. 2, pp. 131-144.

32. Azuma, A.: "Dynamic Analysis of the Rigid Rotor System," Journal of Aircraft, Vol. 4, No. 3, May-June 1967, pp. 203-209.

33. Ballard, J. D., Orloff, K. L. and Luebs, A. B.: "Effect of Tip Shape on Blade Loading Characteristics for a Two-Bladed Rotor in Hover," Preprint No. 79-1, American Helicopter Society 35th Annual National Forum Proceedings, May 21-23, 1979.

34. Ballard, J. D., Orloff, K. L. and Luebs, A. B.: "Effect of Tip Planform on Blade Loading Characteristics for a Two-Bladed Rotor in Hover," NASA TM 78615, November, 1979.

35. Kocurek, J. D., Berkowitz, L. F. and Harris, F. D.: "Hover Performance Methodology at Bell Helicopter Textron," Preprint No. 80-3, American Helicopter Society 36th Annual National Forum Proceedings, May 13-15, 1980.

36. Scheiman, J.: "A Tabulation of Helicopter Rotor-Blade Difference Pressures, Stresses, and Motions as Measured in Flight," NASA TM X-952, 1964.

37. Bell Helicopter Co.: "Measurement of Dynamic Air Loads on a Full-Scale Semirigid Rotor," TCREC-TR-62-42, Dec. 1962.

38. Rabbott, J. P., Jr.: "Static-Thrust Measurements of the Aerodynamic Loading on a Helicopter Rotor Blade," NACA TN 3688, July 1956.

39. Lizak, A. A.: "Two-Dimensional Wind Tunnel Tests on an H-34 Main Rotor Airfoil Section," TRECOM TR-60-53, U. S. Army Transportation Res. Command, Fort Eustis, VA, 1960.

40. Abbott, J. H. and Doenhoff, A. E.: "Theory of Wing Sections," Dover, New York, 1958.

41. Johnson, W. R.: "Comparison of Calculated and Measured Model Rotor Loading and Wake Geometry," NASA TM 81189, April 1980.

42. Kawachi, K.: "A Calculation of Airloading on the Rotary Wing and Its Evaluation," Journal of Japan Society for Aeronautics and Space Sciences, Vol. 27, No. 309, October 1979, pp. 510-516.

	A	B	C	D	E
Blade section	0012	0012	0012	0015	0012
Blade twist, θ_t (deg.)	-10.902	-8.0	-12.0	0	0
Collective pitch angle at x = 0.75, $\theta_{0.75}$ (deg.)	9.8	9.41	8.97	8.0	5.3
Rotor radius, R(m)	1.045	8.53	6.67	0.762	2.32
Number of blades, b	2	4	2	2	2
Solidity, σ	0.0464	0.0621	0.0369	0.0637	0.0974
Aspect ratio of a blade, AR	13.7	20.5	17.3	10.0	6.54
Flapping hinge offset, x_β	0	0.0357	0	0	0
Mach number of blade tip, M_{tip}	0.226	0.583	0.639	0.188	0.360
Source	NASA TM 78615(34)	NASA TM X-952(36)	TCREC-TR-62-42(37)	NACA TN 2953(26)	NACA TN 3688(38)
	Model	H-34 Flight Test	UH-1A Flight Test	Model	Model

Table 1 Rotor parameters and operating conditions

	Computer time (sec)	
Code/Case	Fig. 29	Fig. 32
Present theory	0.34	0.44
AMI code	23.18	43.03
UTRC code	6.37	7.02-40.52

Table 2 Comparison of computer time

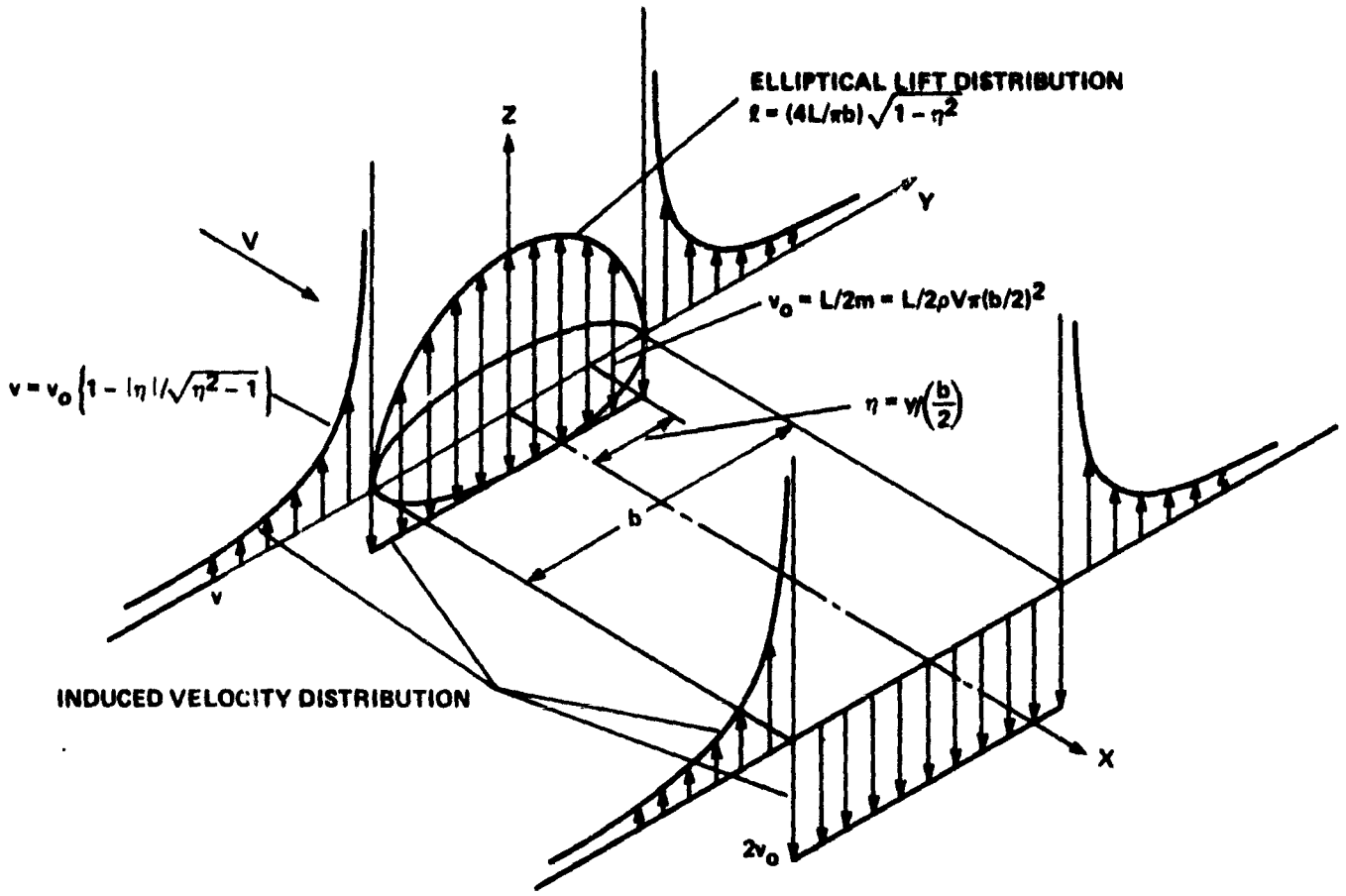

Fig. 1 Lift and induced velocity distributions of an elliptical wing[1].

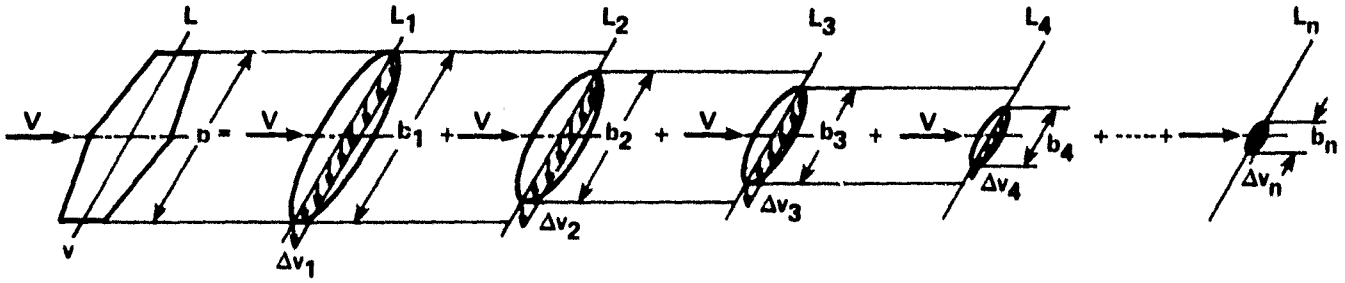

(a) SYMMETRIC ARRANGEMENT

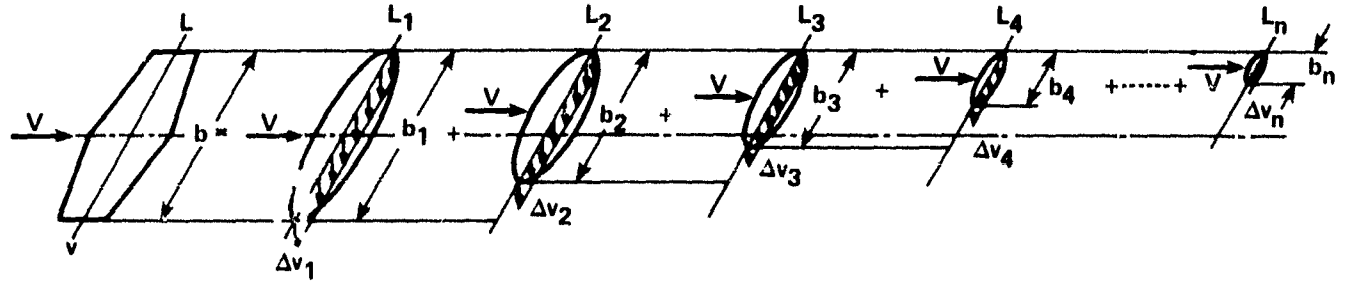

(b) ONE-SIDED ARRANGEMENT

Fig. 2 Decomposition of a fixed wing to hypothetical elliptical wings[1]

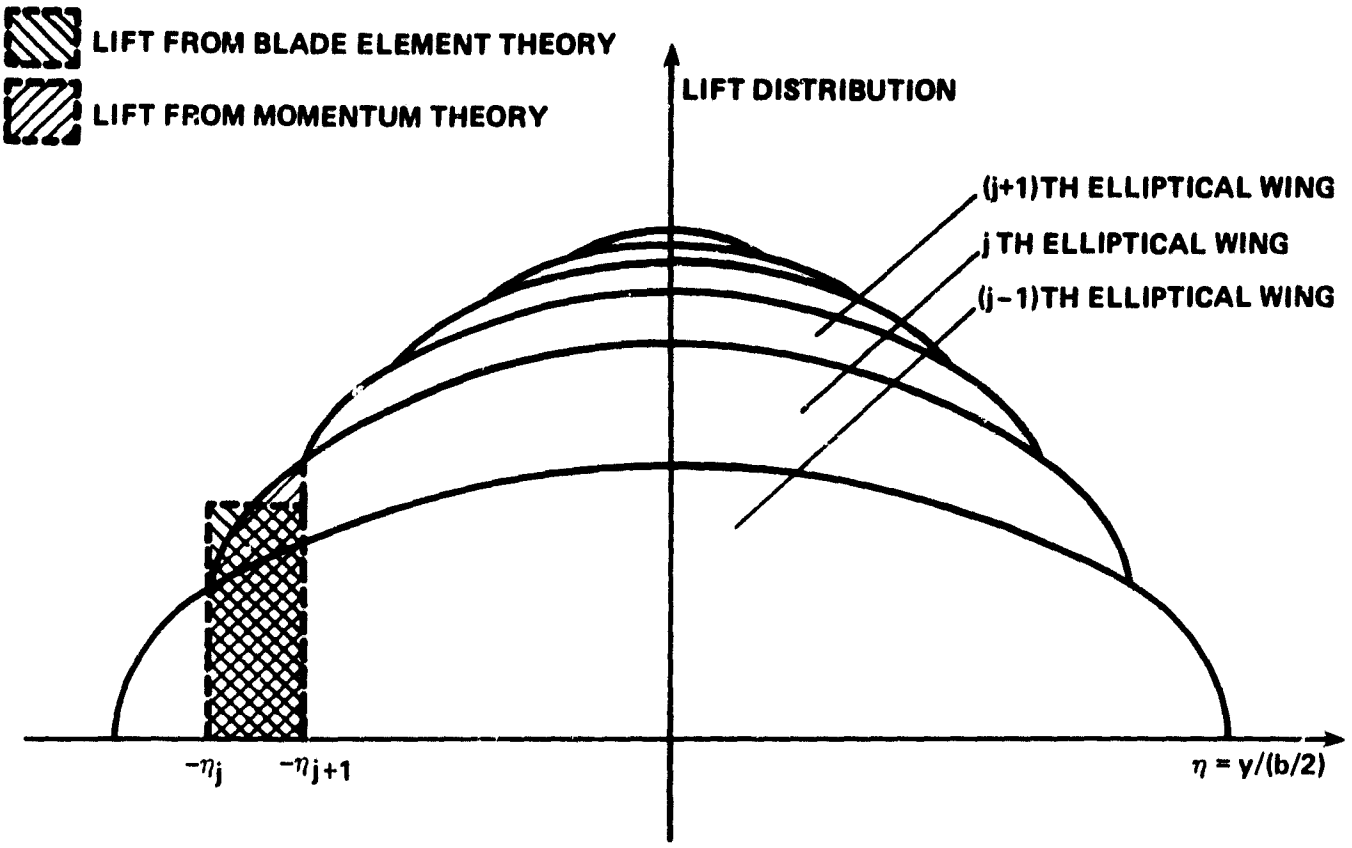

Fig. 3 Lift acting on a local segment of a fixed wing.

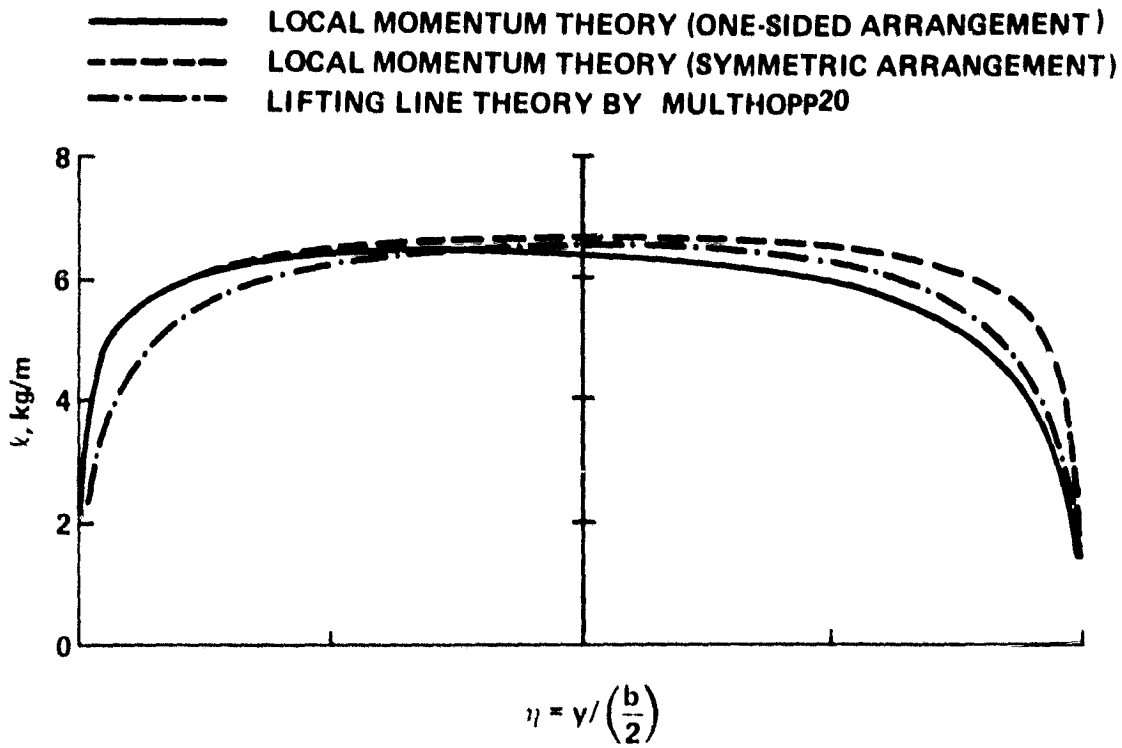

(a) LIFT D STRIBUTION

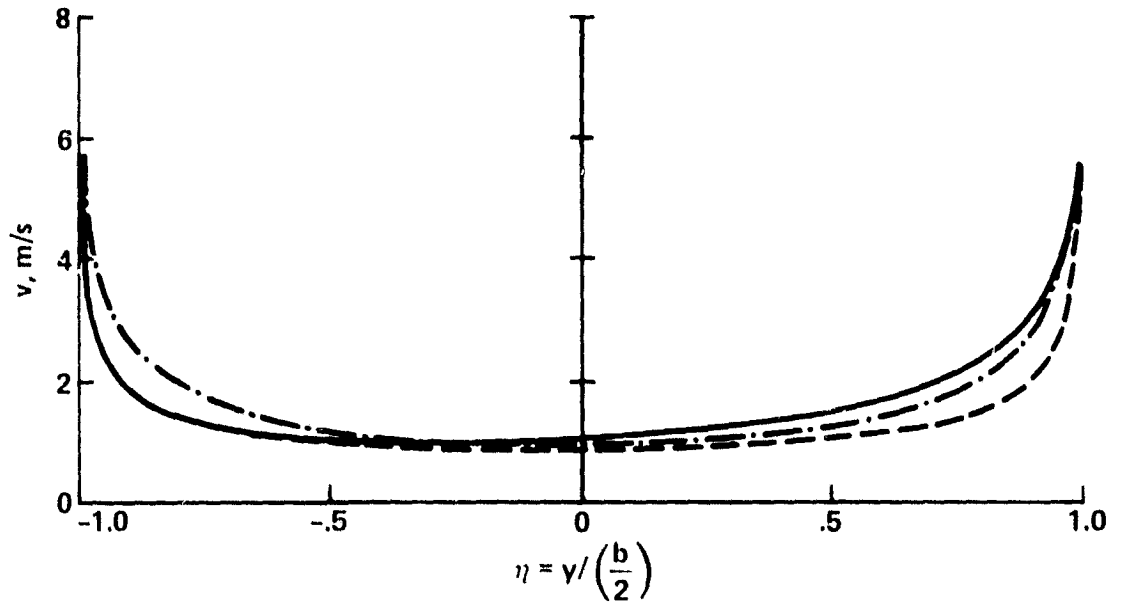

(b) INDUCED VELOCITY DISTRIBUTION

Fig. 4 Lift and induced velocity distributions for a rectangular wing (AR = 6, π = 50).

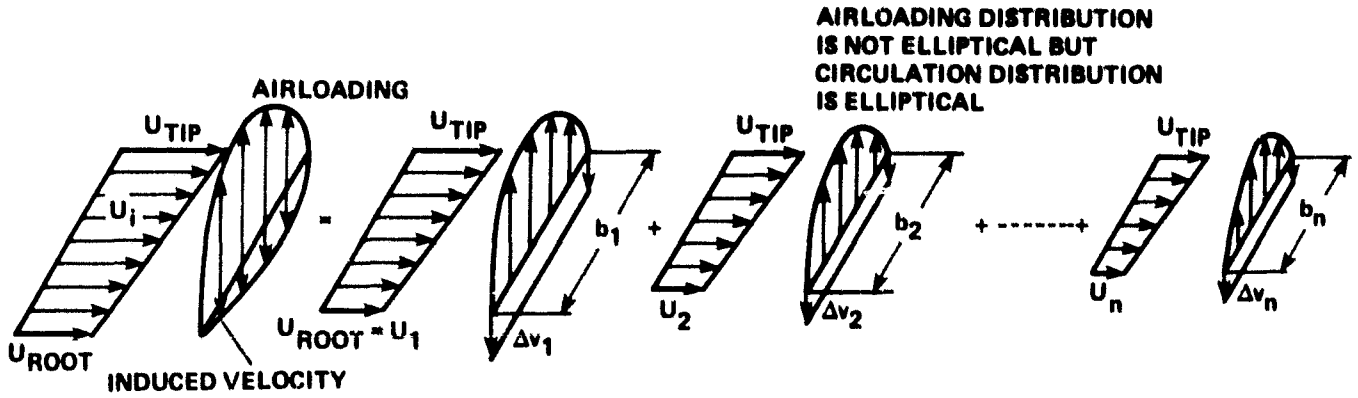

Fig. 5 Decomposition of a rotor blade to hypothetical elliptical wings.

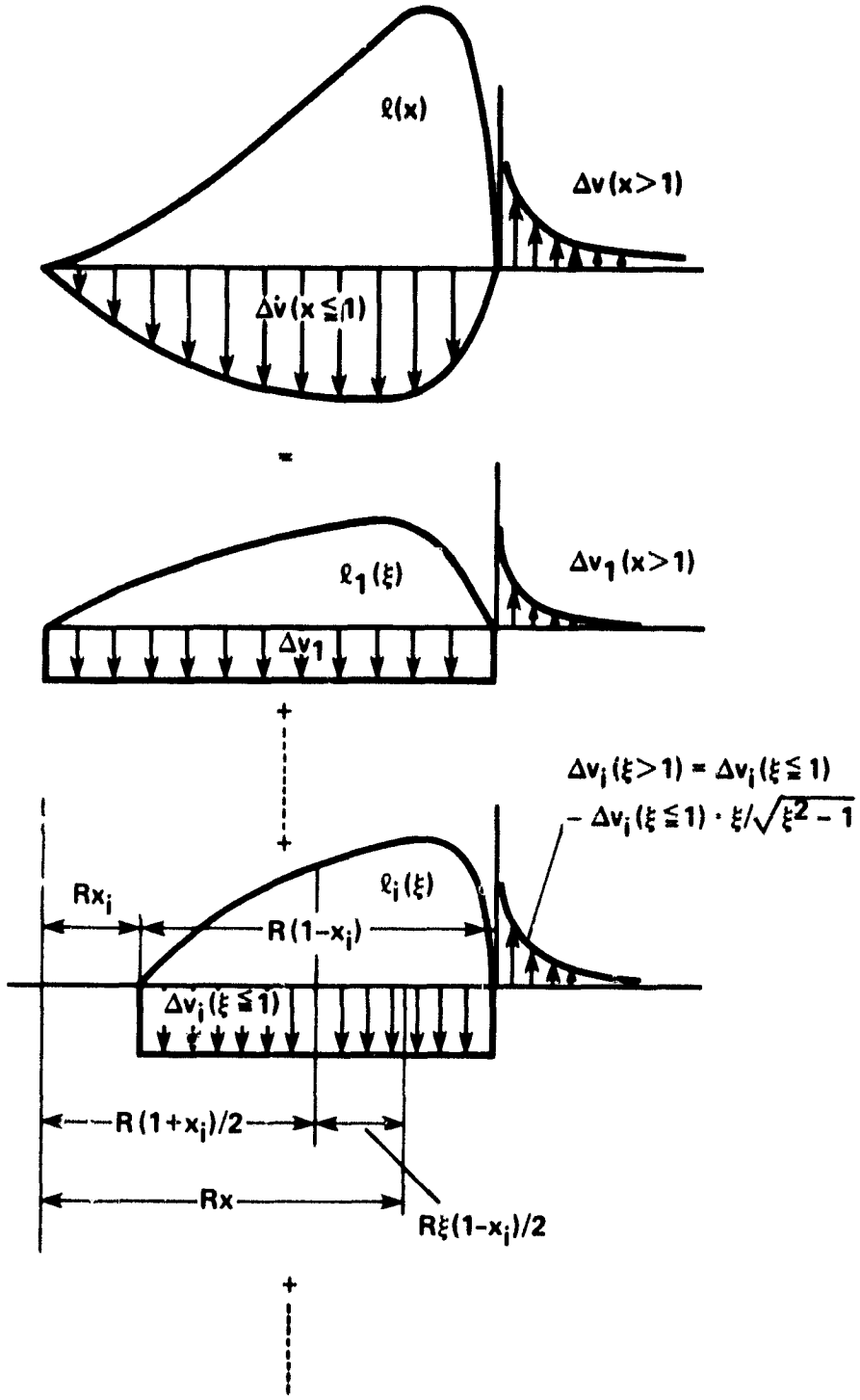

Fig. 6 Summation of induced velocity distributions of component elliptical wings[1].

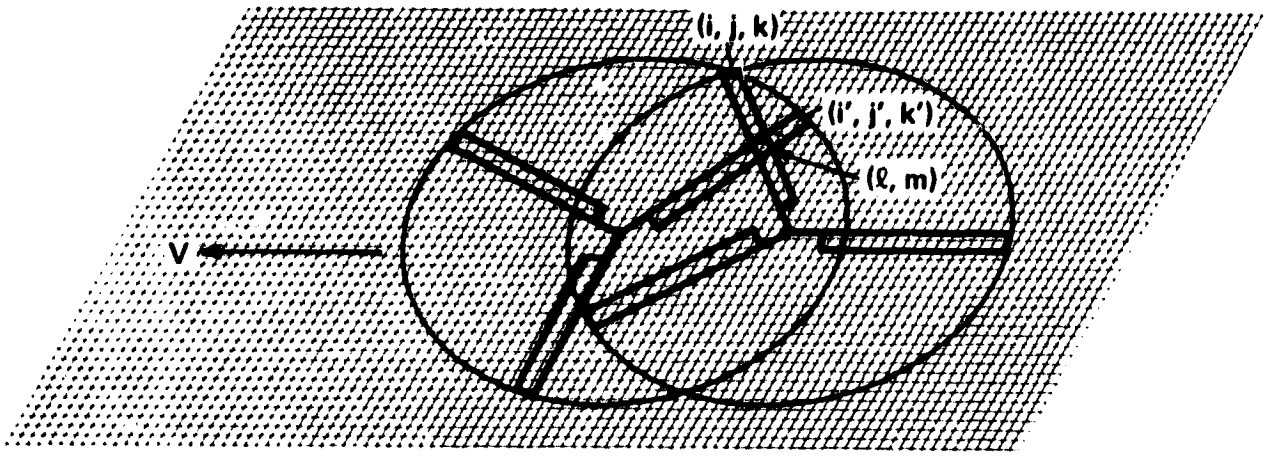

Fig. 7 Two blade passages through a same local station on rotor rotational plane[1].

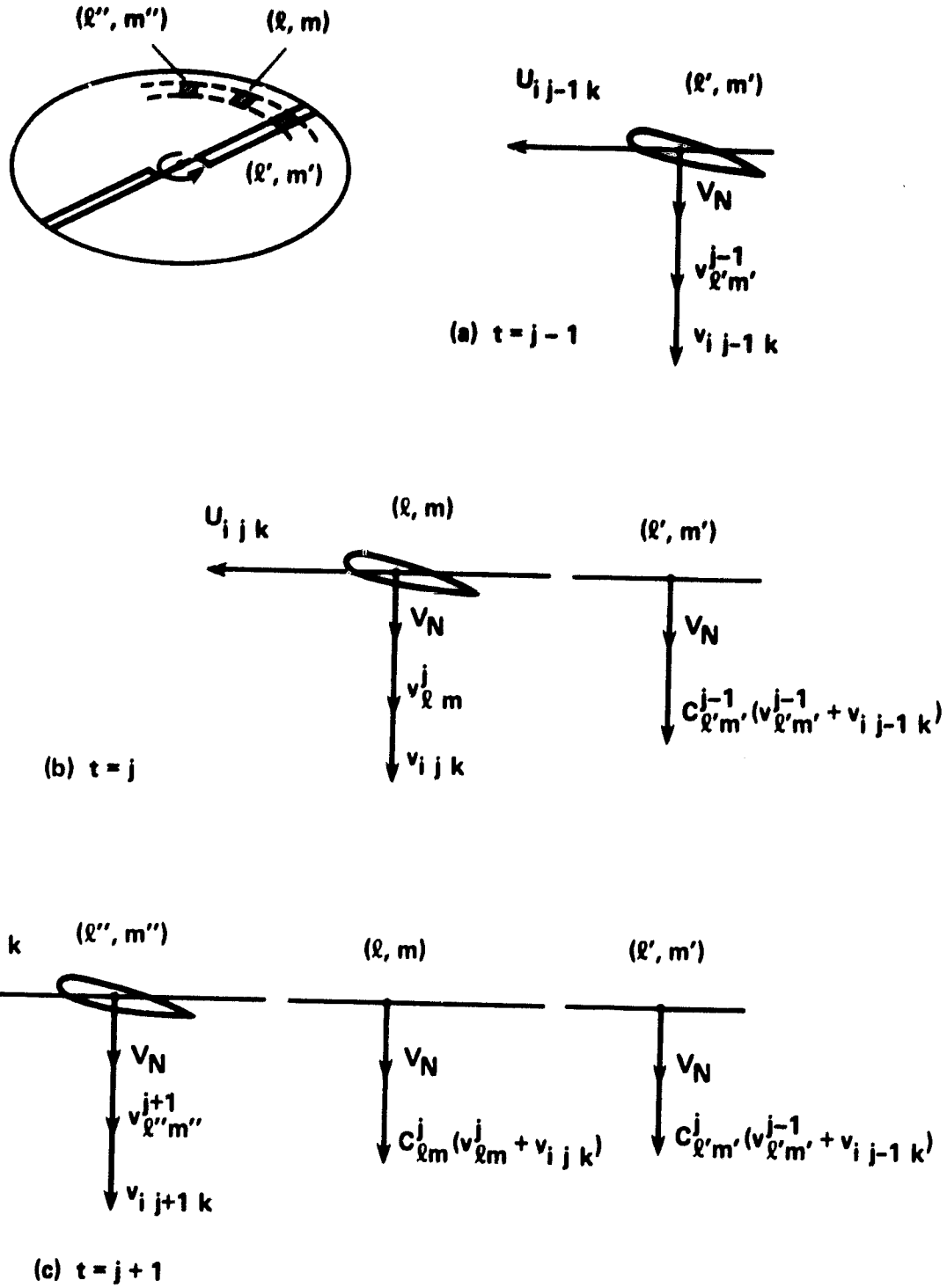

Fig. 8 Time-wise variation of induced velocity on rotor rotational plane[1].

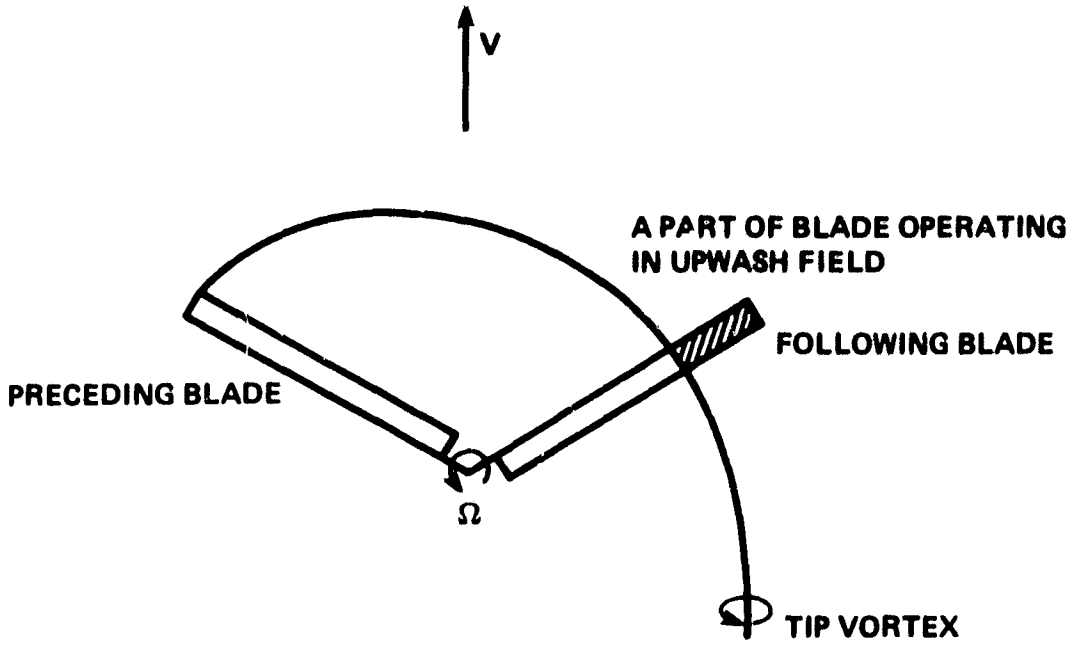

Fig. 9 Effect of upwash of a preceding blade on the following blade[1].

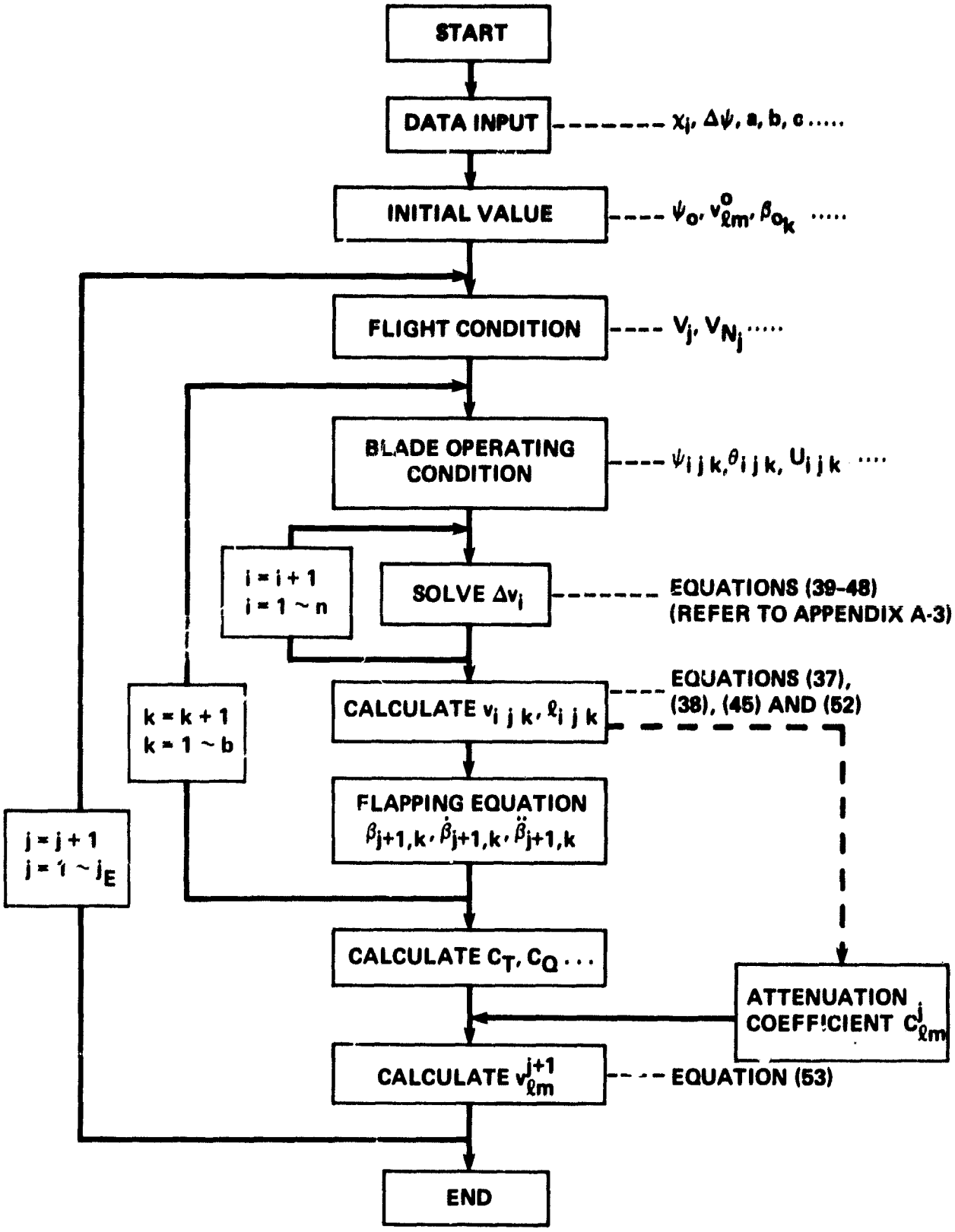

Fig. 10 Global flow chart.

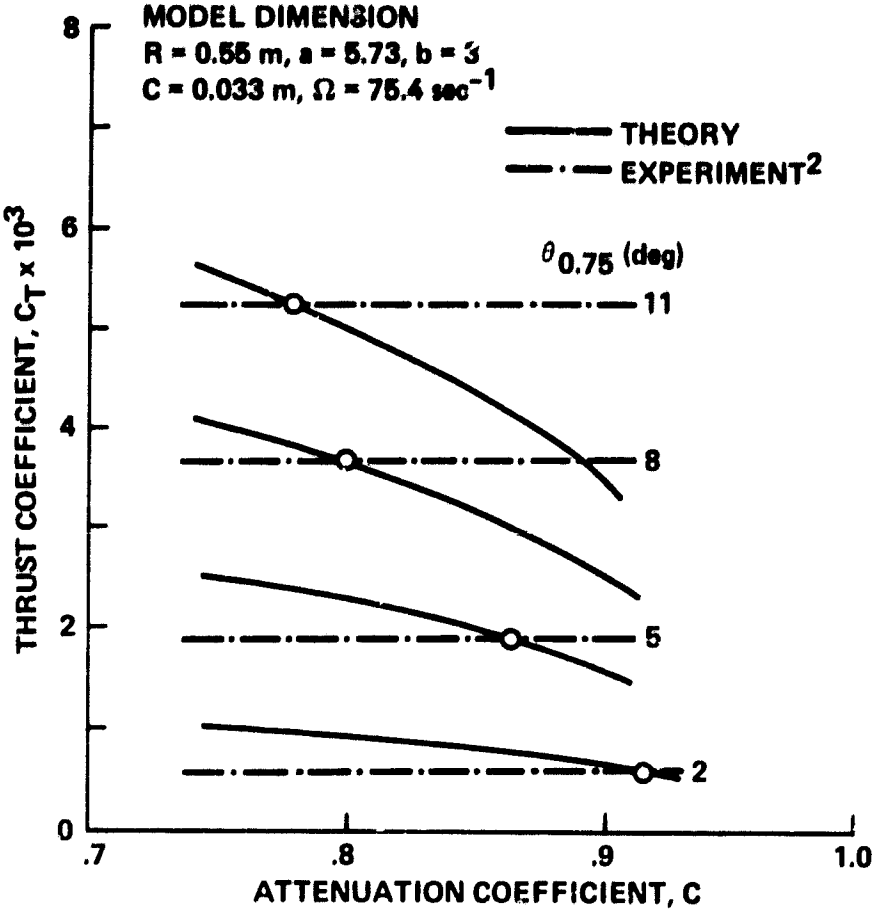

Fig. 11 Thrust coefficient versus uniform attenuation coefficient in hover[2].

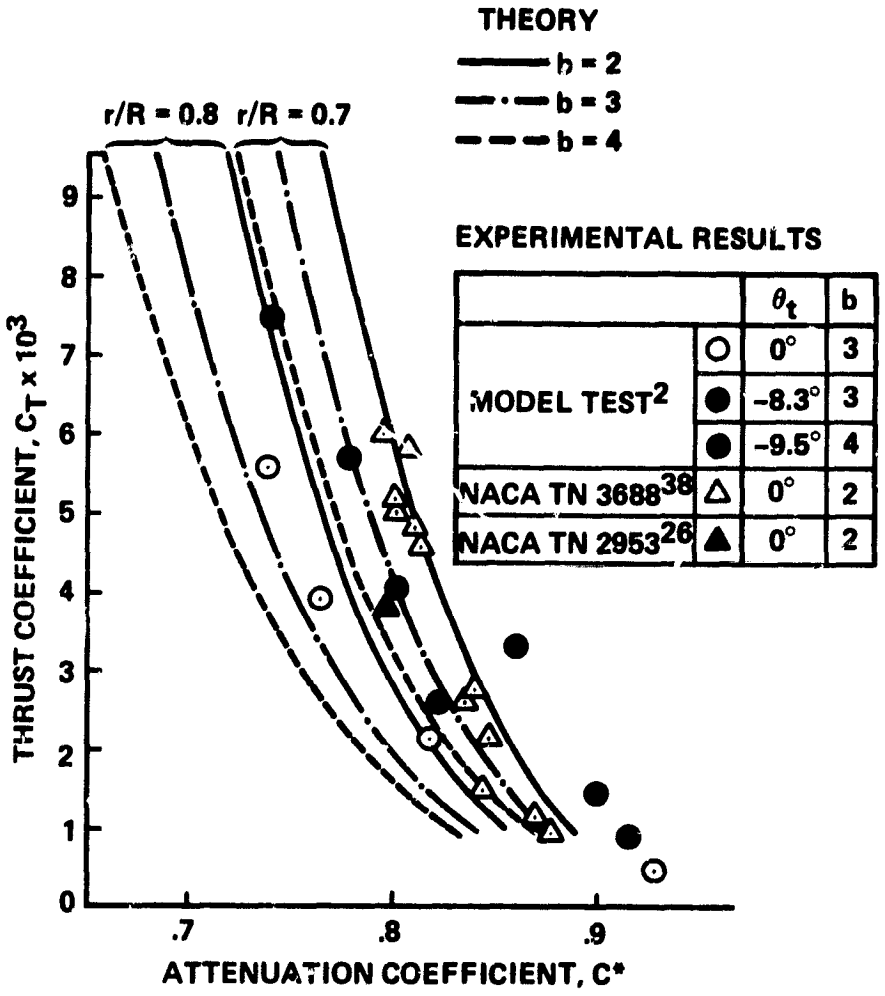

Fig. 12 Comparison of theoretical and experimental results of uniform attenuation coefficient[2].

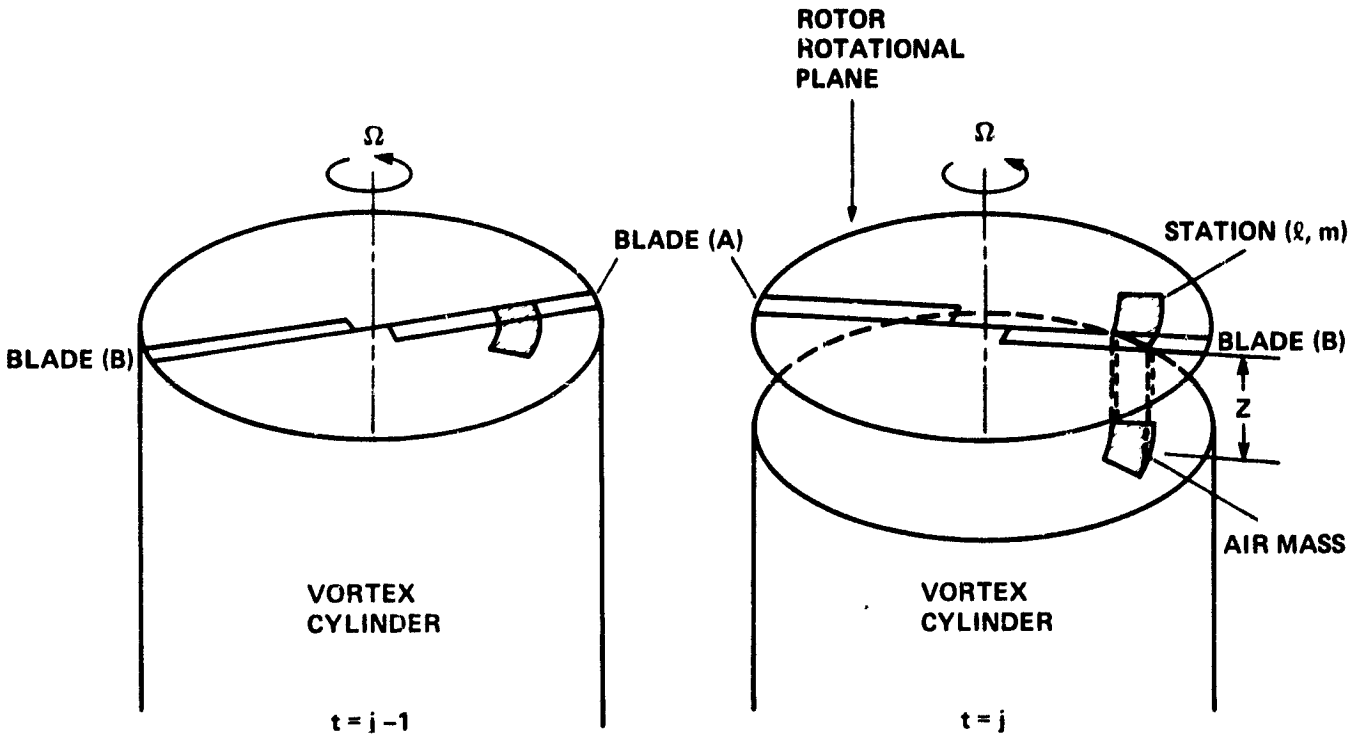

Fig. 13 Model for theoretical attenuation coefficient.

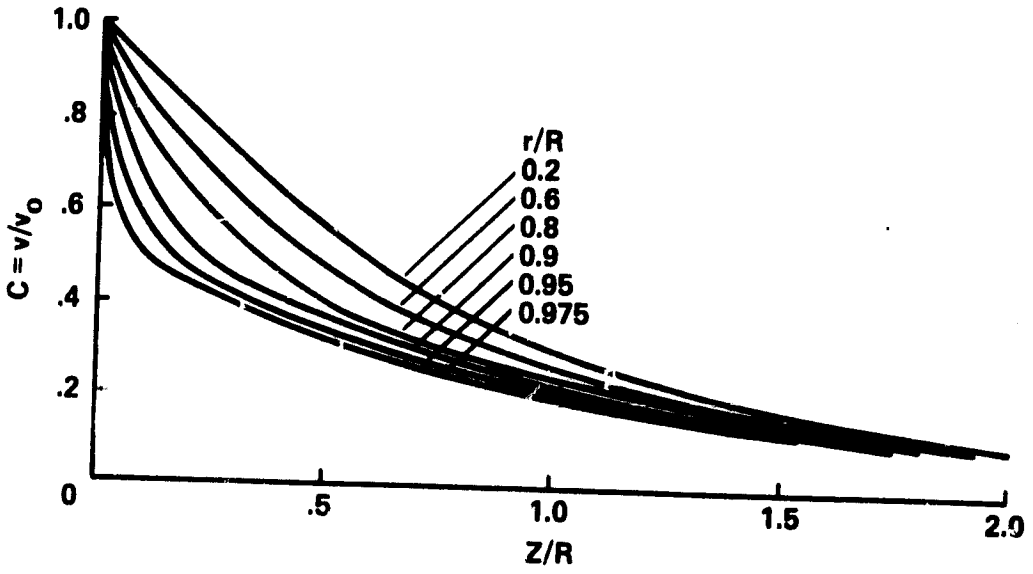

Fig. 14 General chart of attenuation coefficient in hover[2].

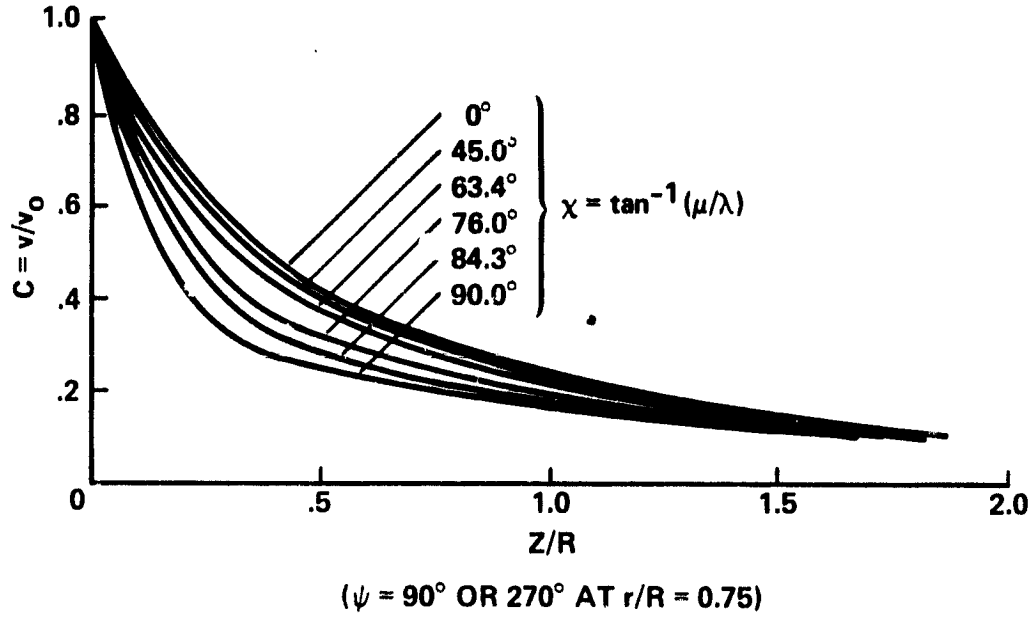

Fig. 15 General chart of attenuation coefficeint in forward flight[2].

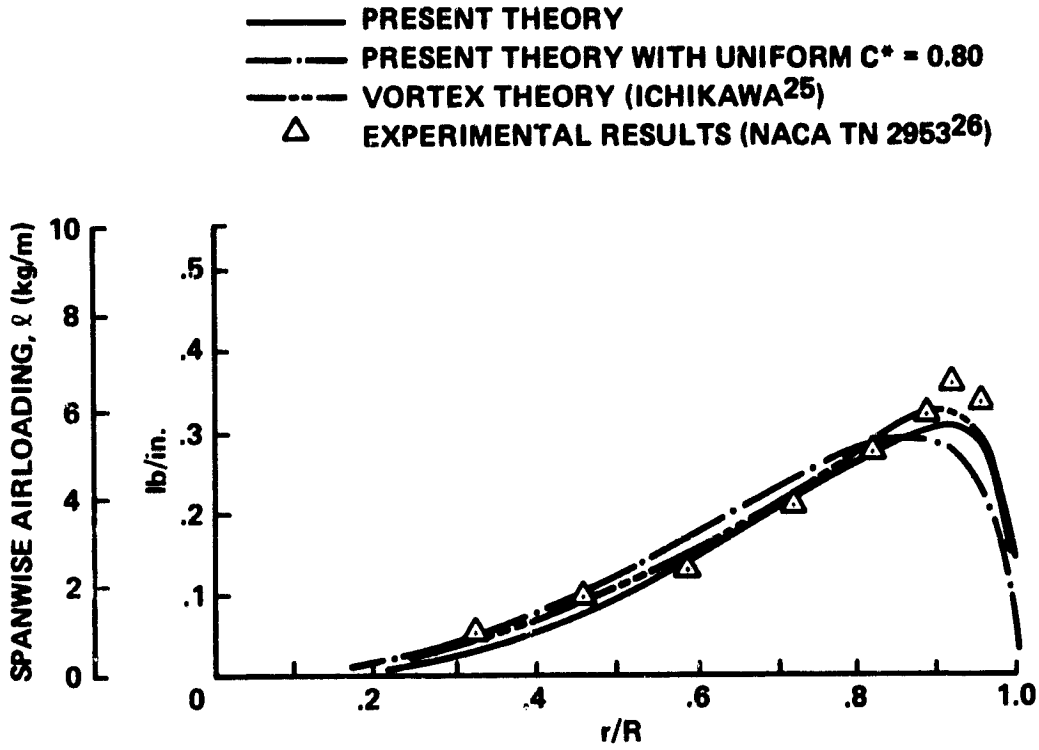

Fig. 16 Spanwise airloading of a rotor blade in hover[1]. (μ = 0, b = 2, θ_t = 0 deg.).

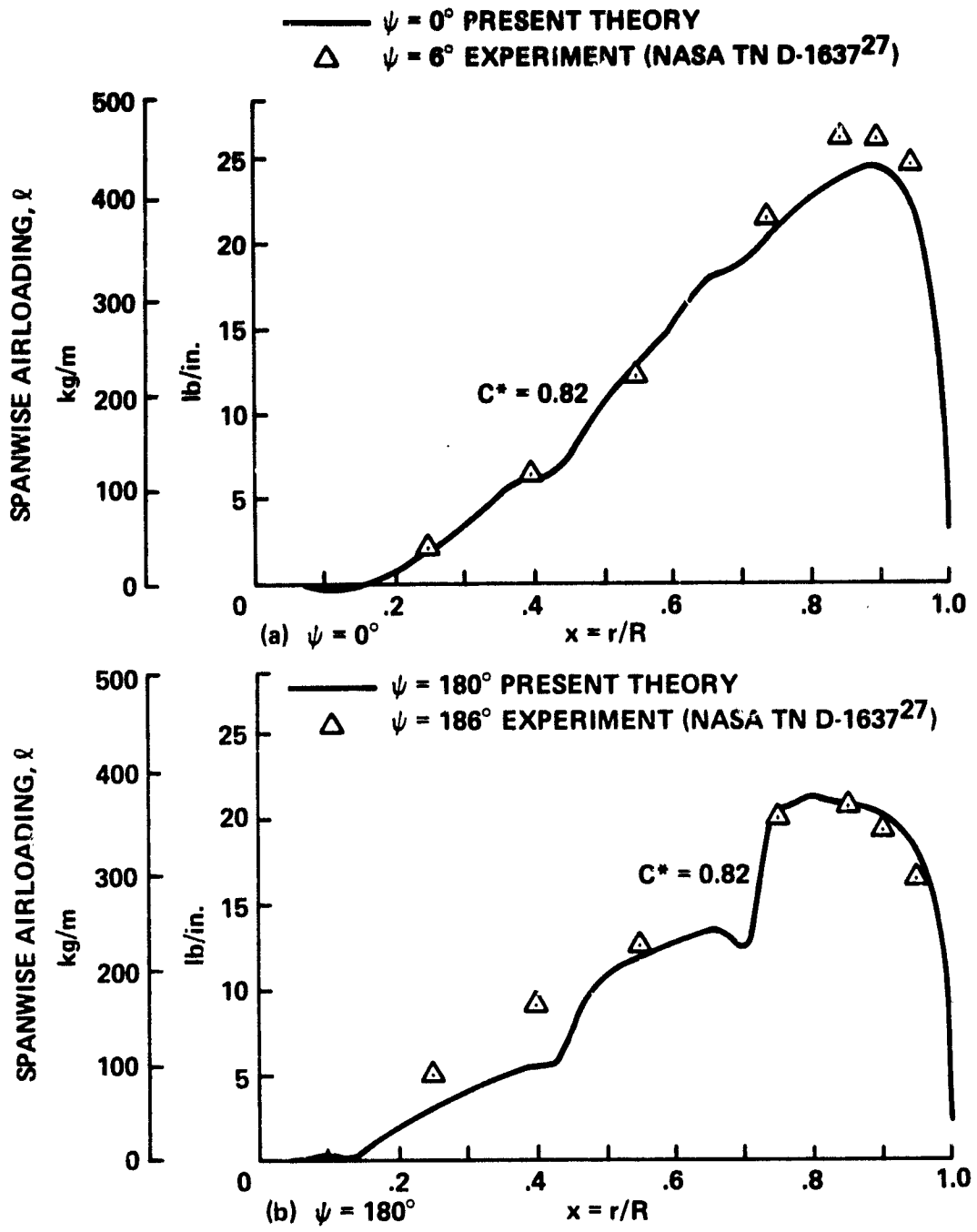

Fig. 17 Spanwise airloading of a rotor blade in forward flight[1] (μ = 0.18, b = 4, θ_t = -8.0 deg.).

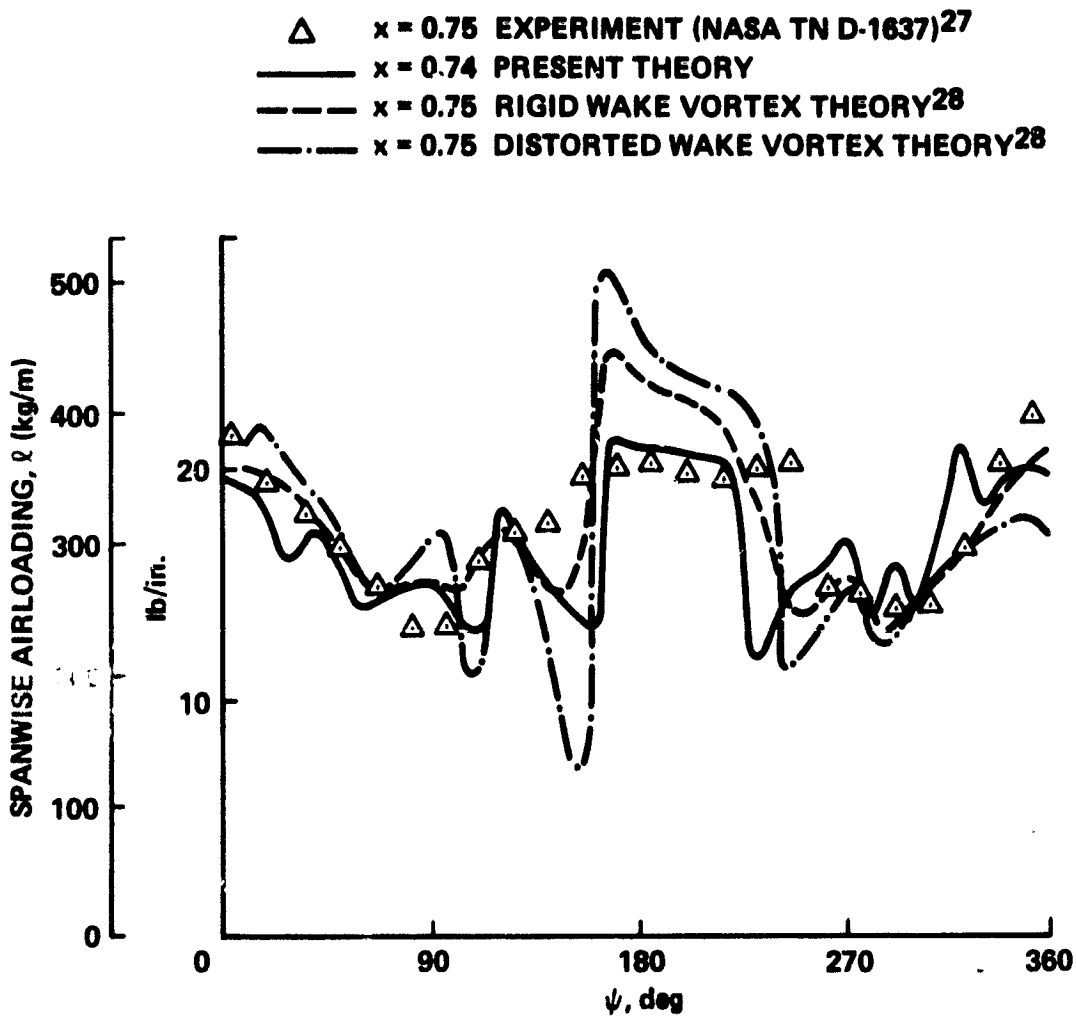

Fig. 18(a) Azimuth-wise variation of airloading in forward flight[1] (μ = 0.18, b = 4, θ_t=-8.0 deg.).

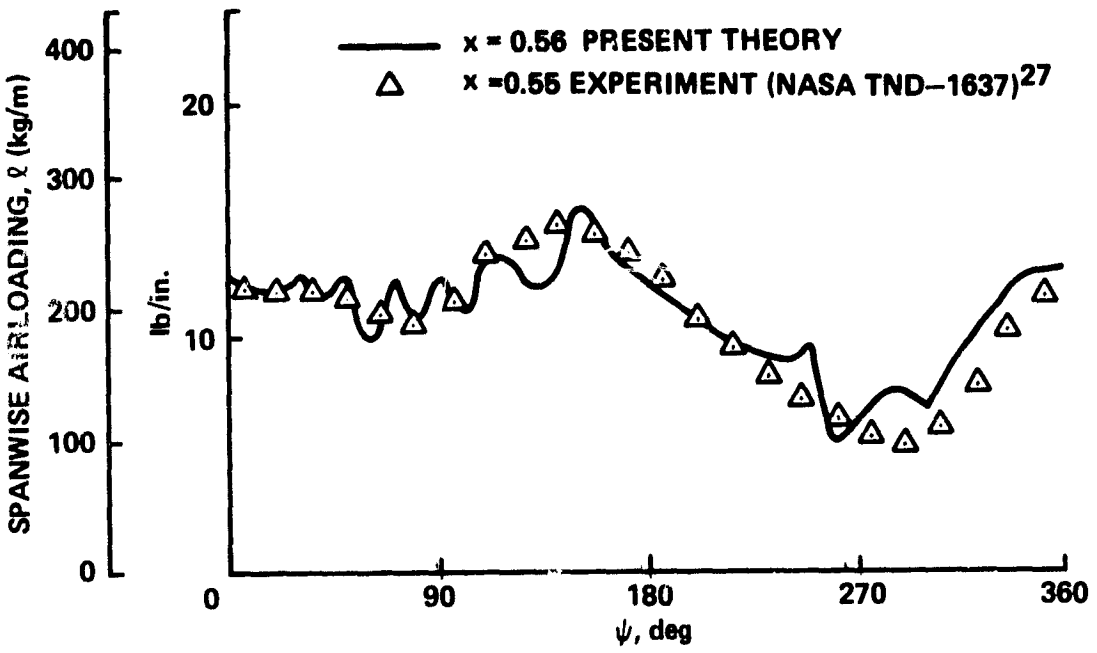

Fig. 18(b) Azimuth-wise variation of airloading in forward flight[1] (μ = 0.18, b = 4, θ_t= -8.0 deg.).

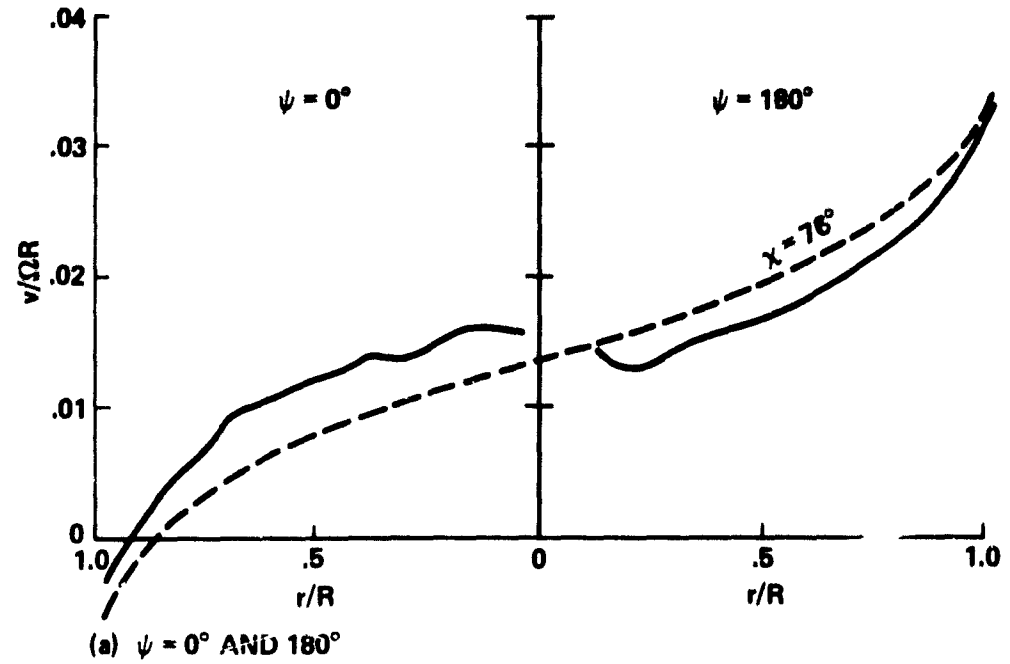

(a) $\psi = 0°$ AND 180°

PRESENT THEORY

SIMPLE VORTEX THEORY USING A VORTEX CYLINDER[23]

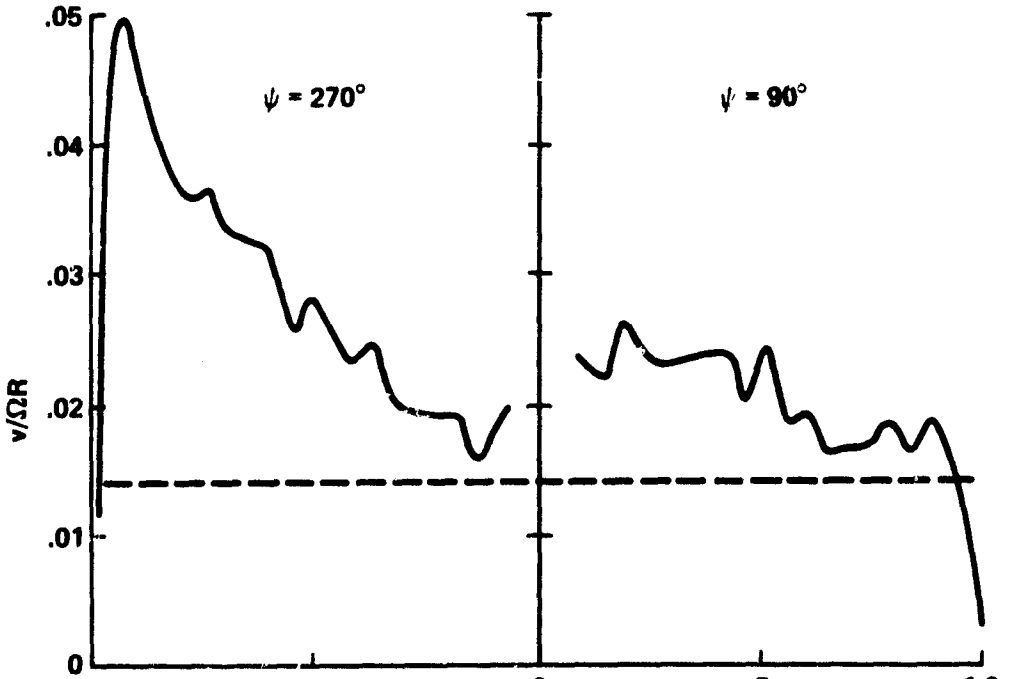

(b) $\psi = 90°$ AND 270°

Fig. 19 Radial distribution of time averaged induced velocity[1] ($\mu = 0.18$, $b = 4$, $\theta_t = -8.0$ deg.).

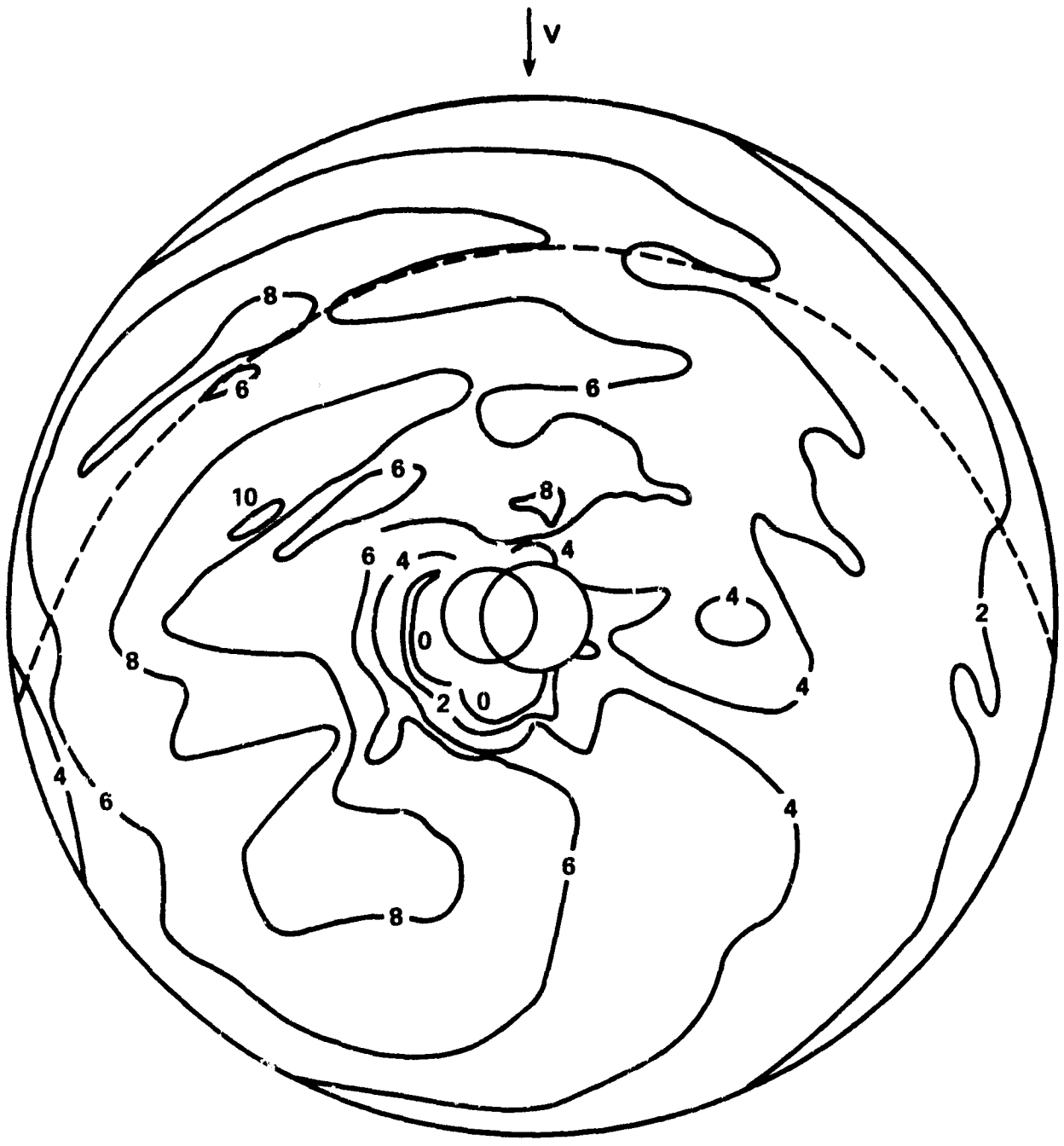

---- TRACE OF INTERSECTION OF BLADE UNDER CONSIDERATION WITH TIP VORTEX OF PRECEDING BLADE

Fig. 20 Distribution of angle of attack (deg.)[42] (μ = 0.18, b = 4, θ_t=-8.0 deg.).

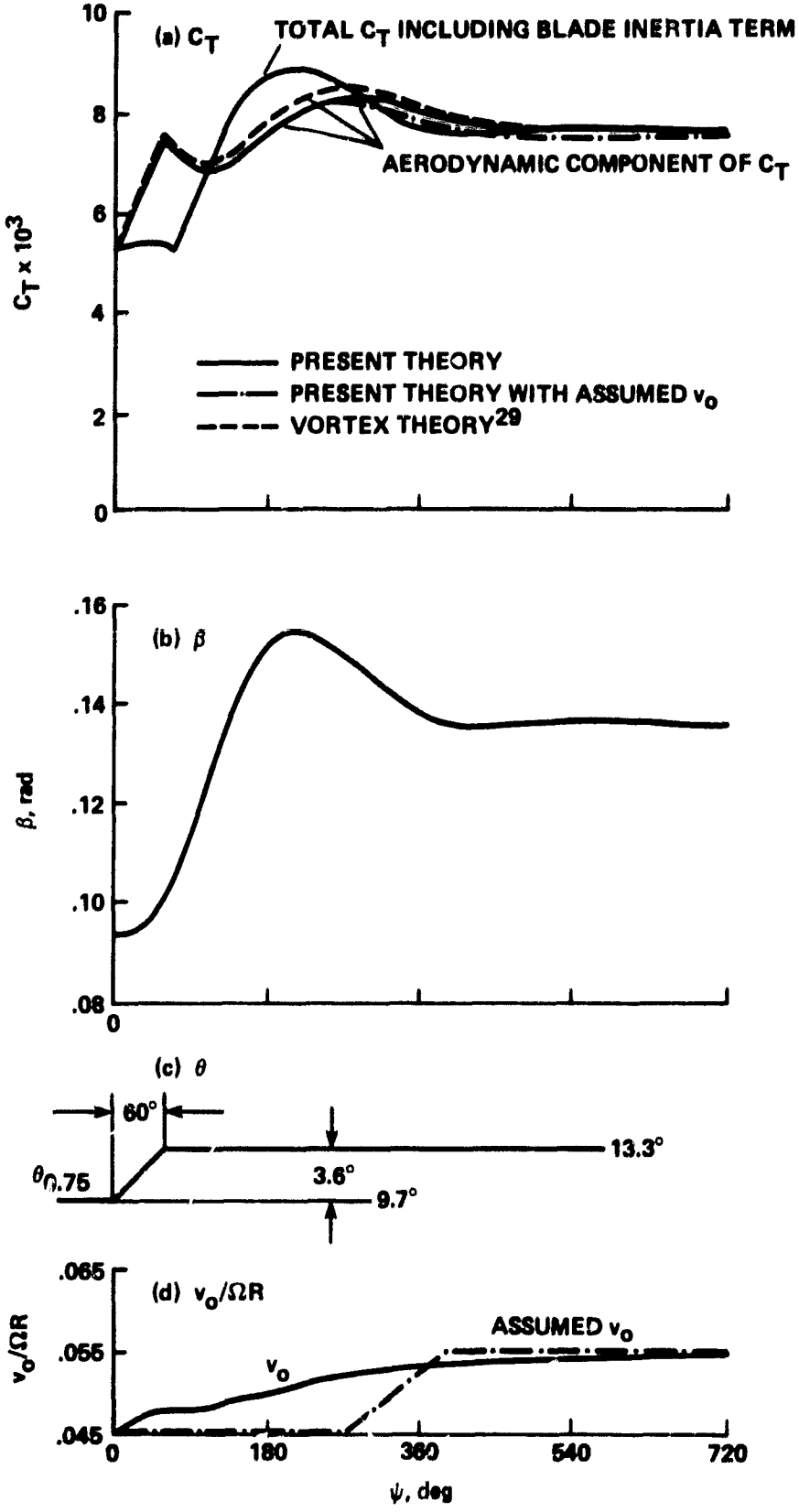

Fig. 21 Time response caused by a rapid increase of collective pitch[1] (μ = 0, b = 4, θ_t = -8.0 deg.).

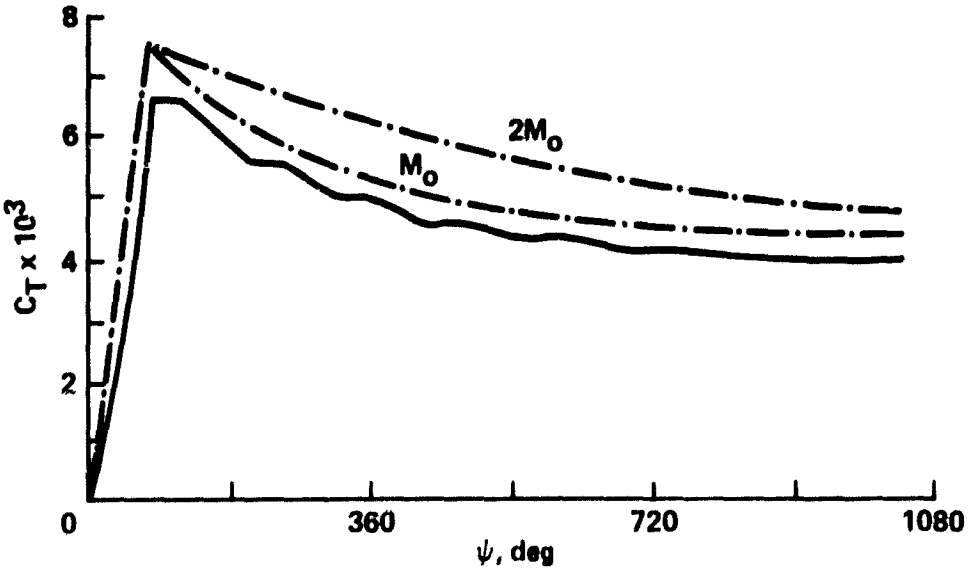

(a) THRUST COEFFICIENT

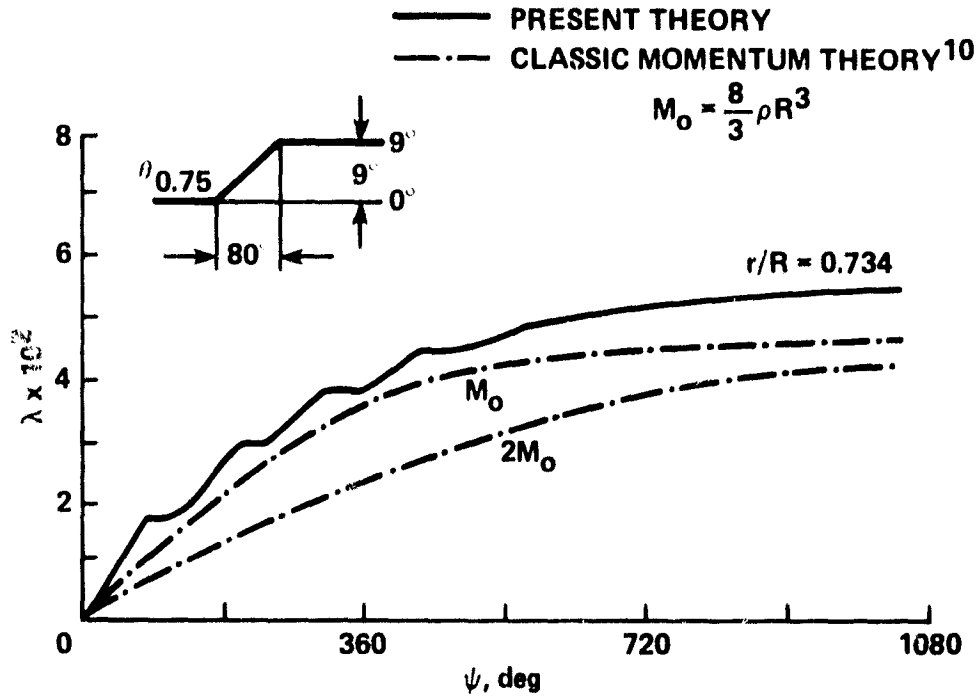

(b) INFLOW RATIO AT r/R = 0.75

Fig. 22 Comparison of the results obtained by present theory and classical momentum theory[1] ($\mu = 0$, $b = 3$, $\theta_t = 0.0$ deg.).

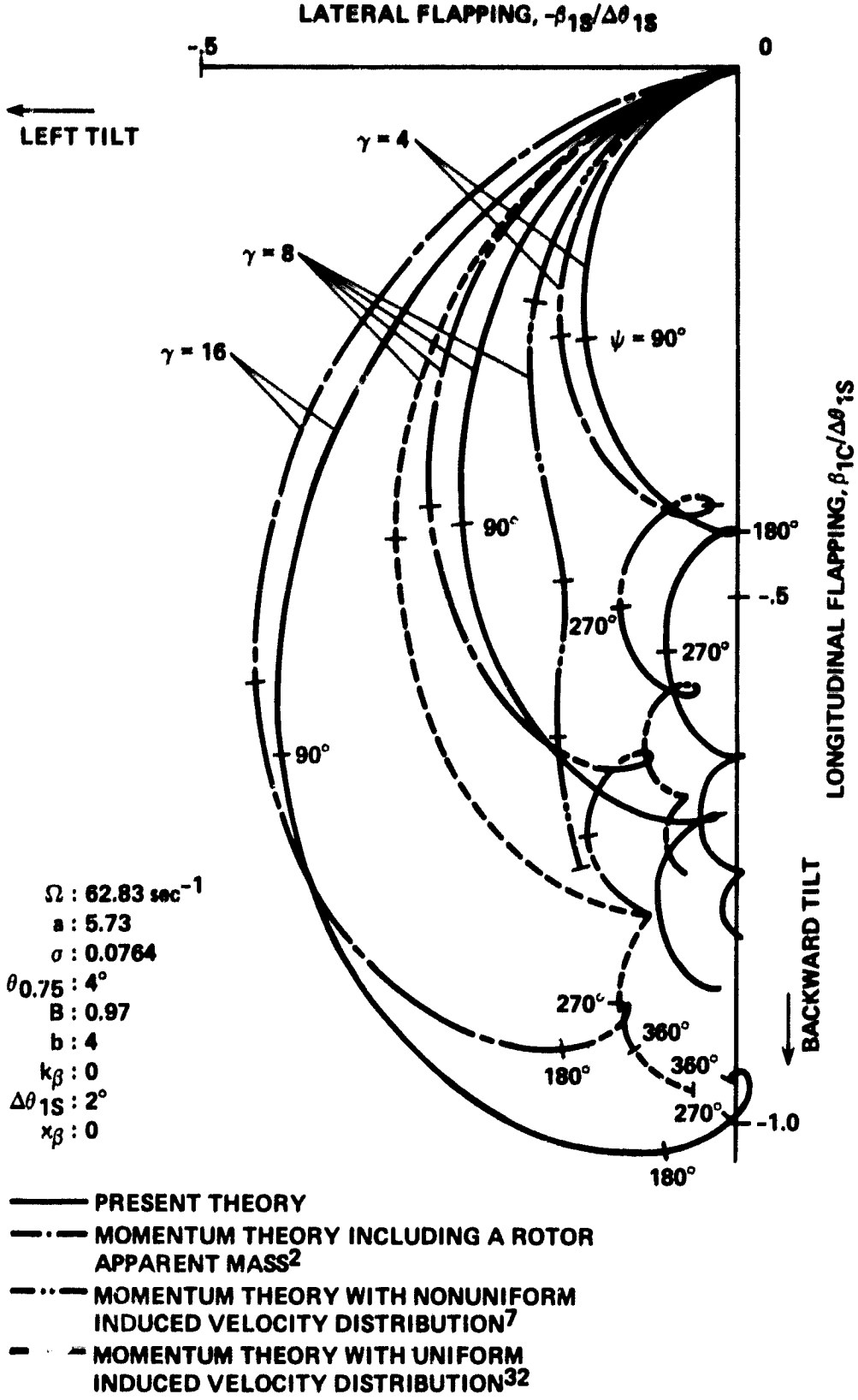

Fig. 23 Inclination of tip path plane following a step cyclic pitch input[2] (μ = 0, b = 4, θ_{β} = 0 deg.).

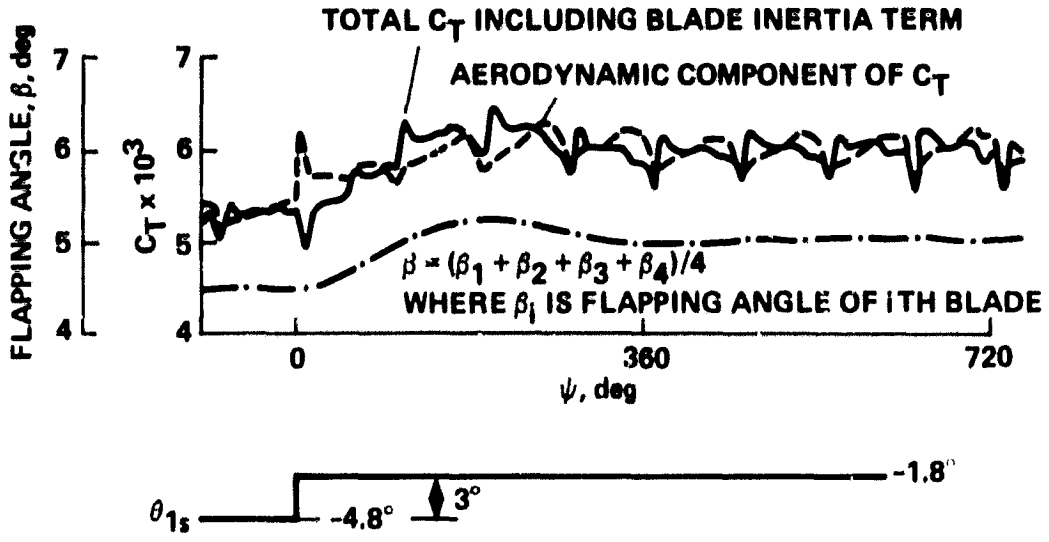

(a) TIME RESPONSE

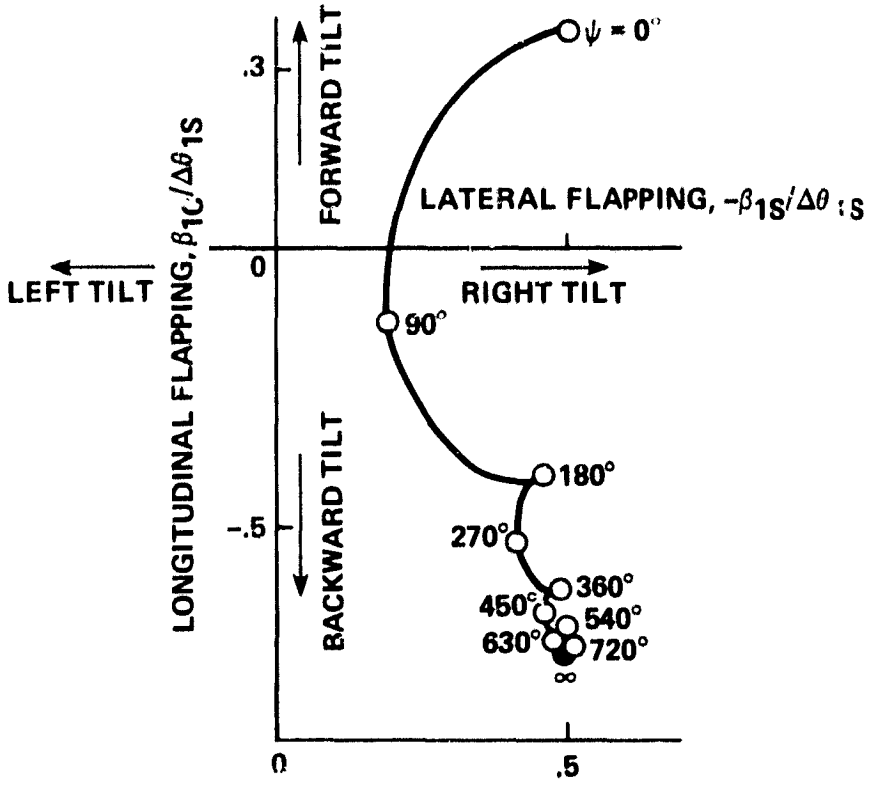

(b) INCLINATION OF TIP PATH PLANE

Fig. 24 Time response to a step cyclic pitch input[1] (μ = 0.18, b = 4, θ_t = -8.0 deg.).

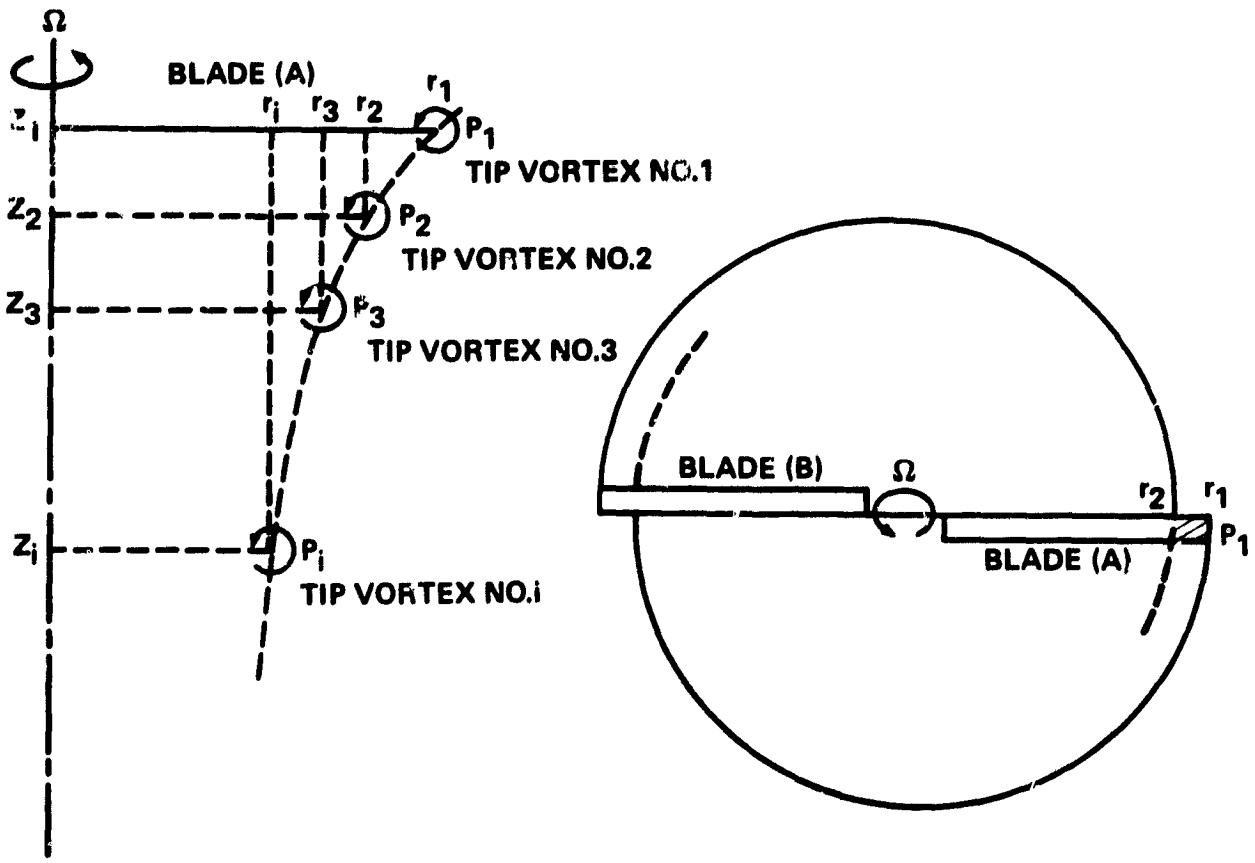

(a) SIDE VIEW OF TIP VORTICES (b) TOP VIEW OF TIP VORTICES

Fig. 25 Views of Tip Vortices.

C-2

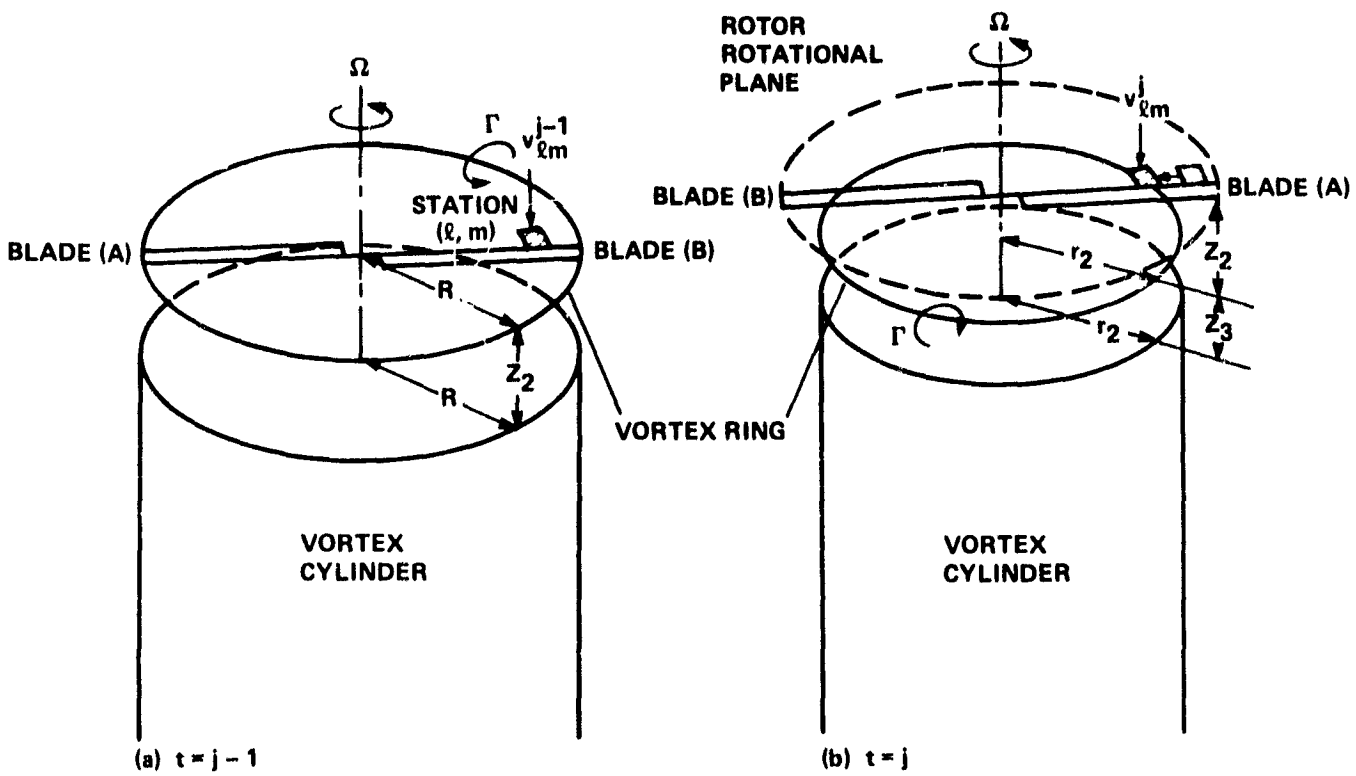

Fig. 26 Extended model for attenuation coefficient.

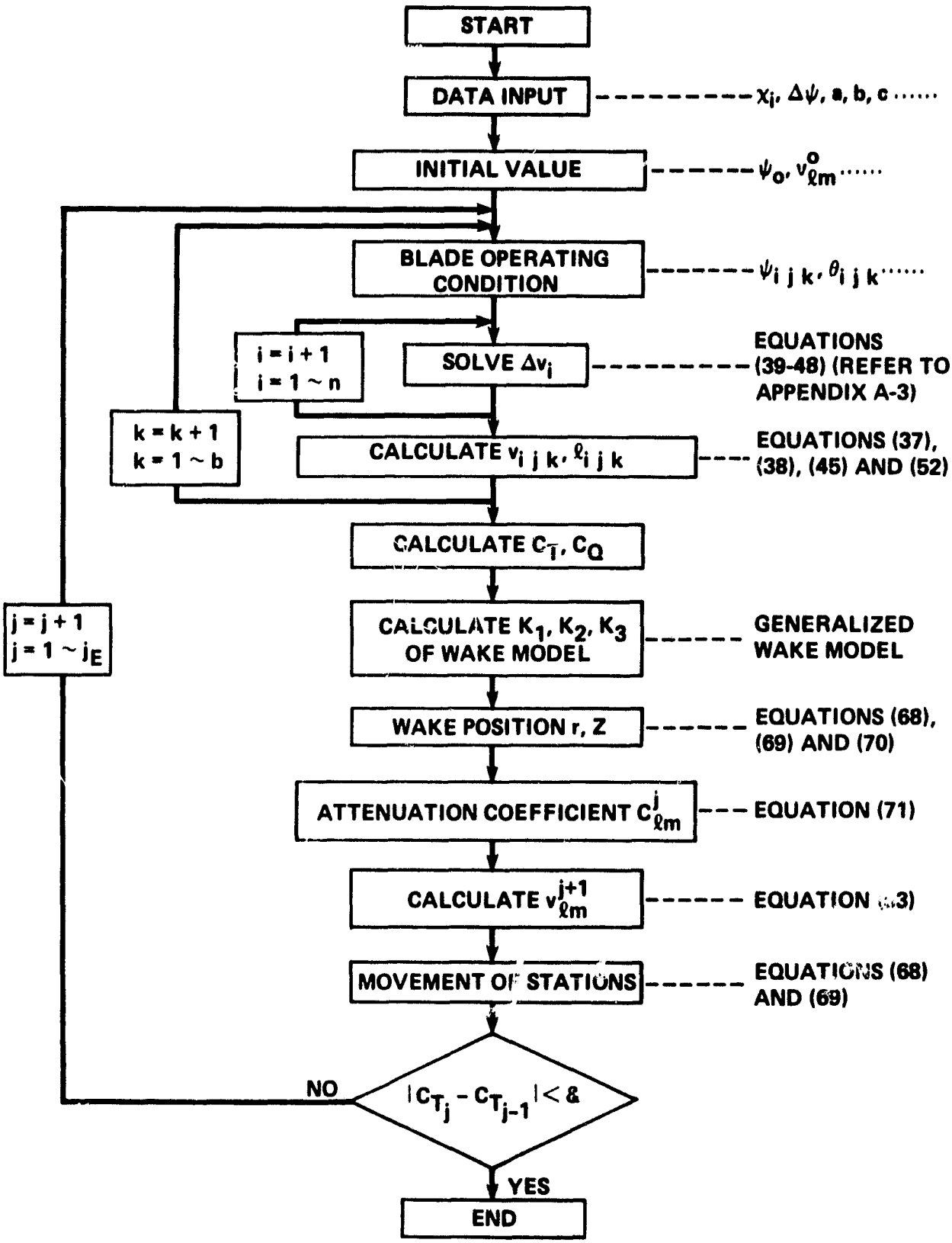

Fig. 27 Global flow chart of extended Local Momentum Theory.

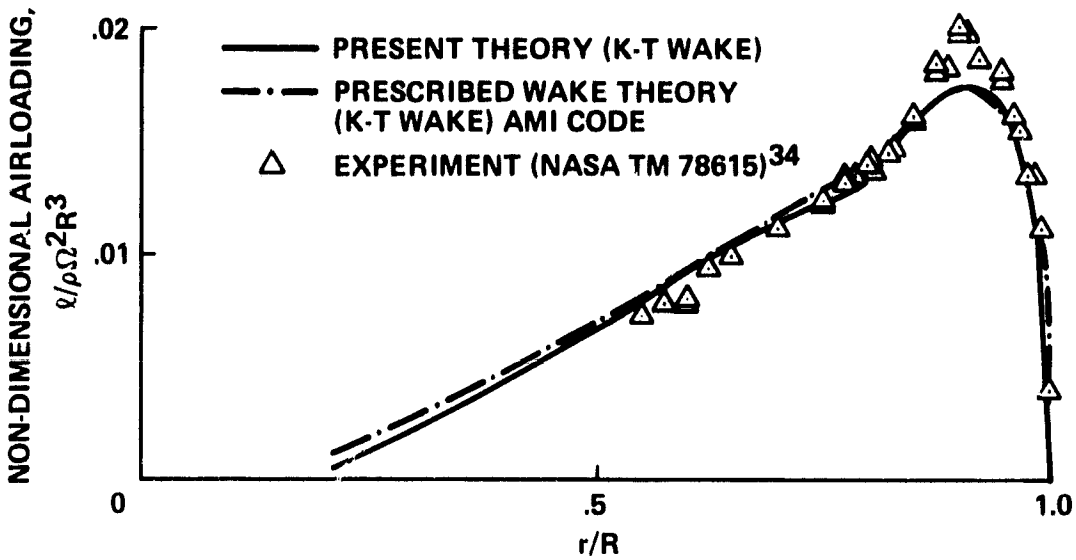

Fig. 28 Comparison of measured and calculated spanwise lift distributions in hover, with Kocurek and Tangular wake model, (b = 2, θt = -10.9 deg., AR = 13.7, $\theta_{0.75}$ = 9.8 deg.).

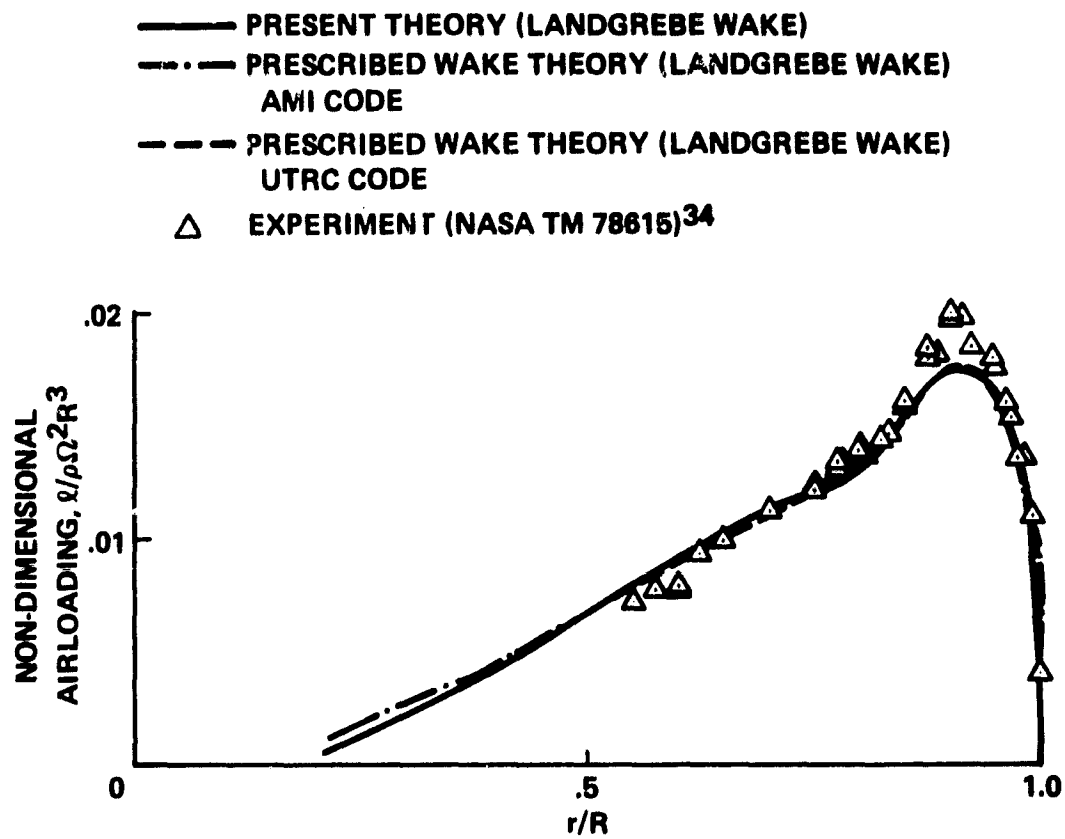

Fig. 29 Comparison of measured and calculated spanwise lift distributions in hover, with Landgrebe wake model, (b = 2, θ_t = -10.9 deg., AR = 13.7, $\theta_{0.75}$ = 9.8 deg.).

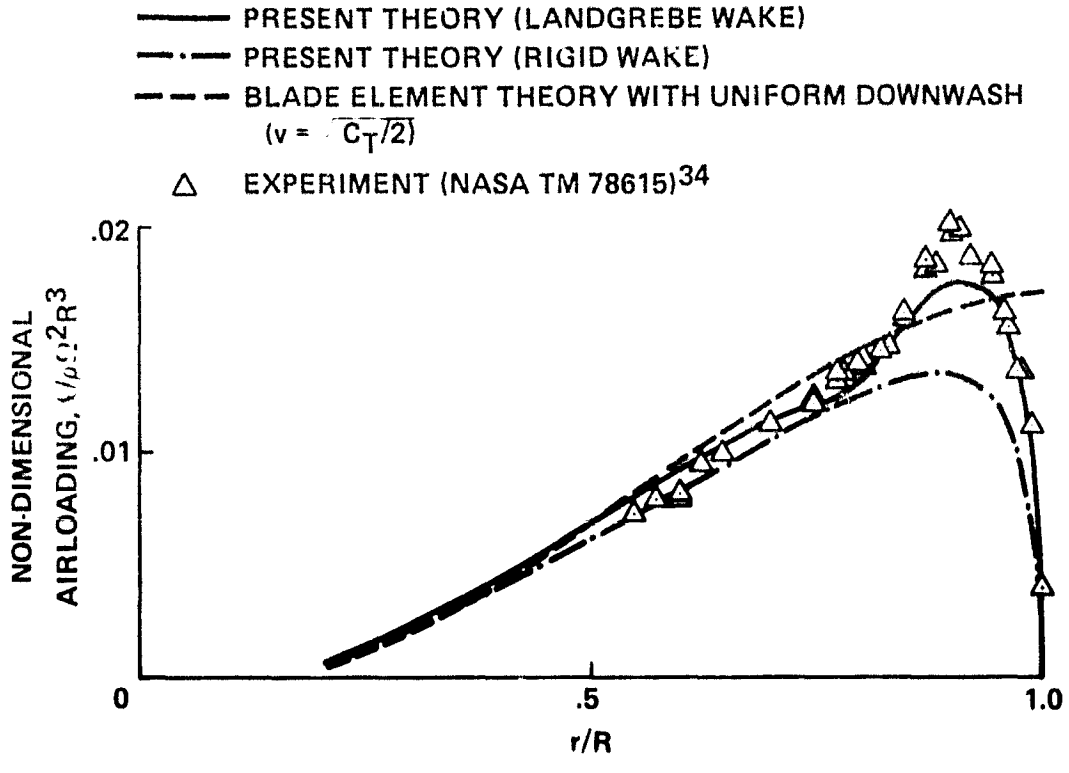

Fig. 30 Comparison of distorted wake model with rigid wake model or blade element theory, ($b = 2, \theta_t = -10.9$ deg., $AR = 13.7$, $\theta_{0.75} = 9.8$ deg.).

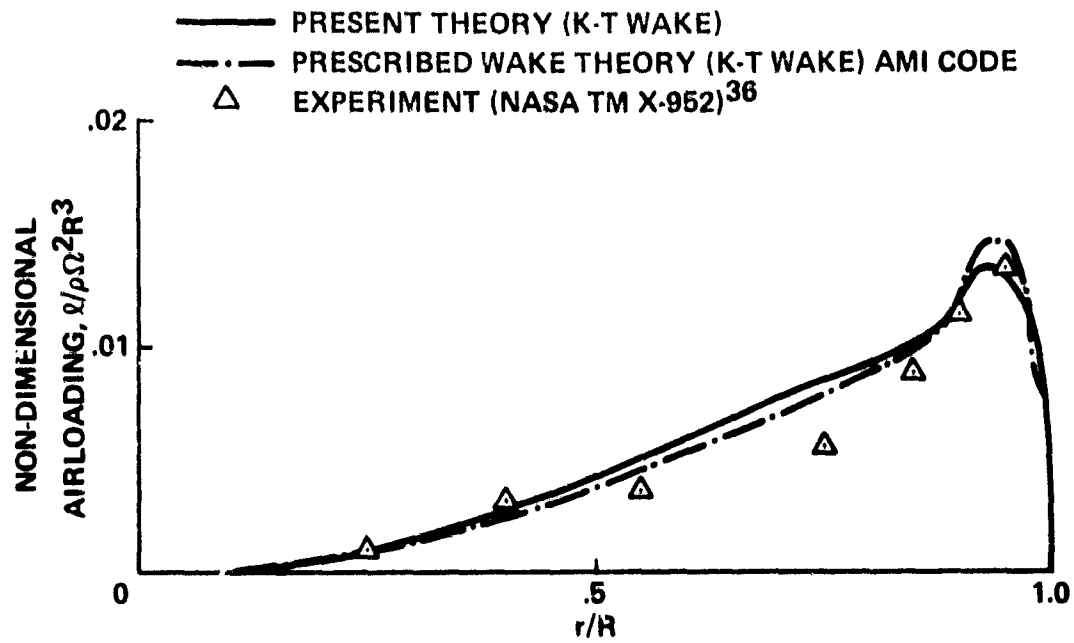

Fig. 31 Comparison of measured and calculated spanwise lift distributions in hover, with Kocurek and Tangular wake model, ($b = 4, \theta_t = -8.0$ deg., $AR = 20.5, \theta_{0.75} = 9.41$ deg.).

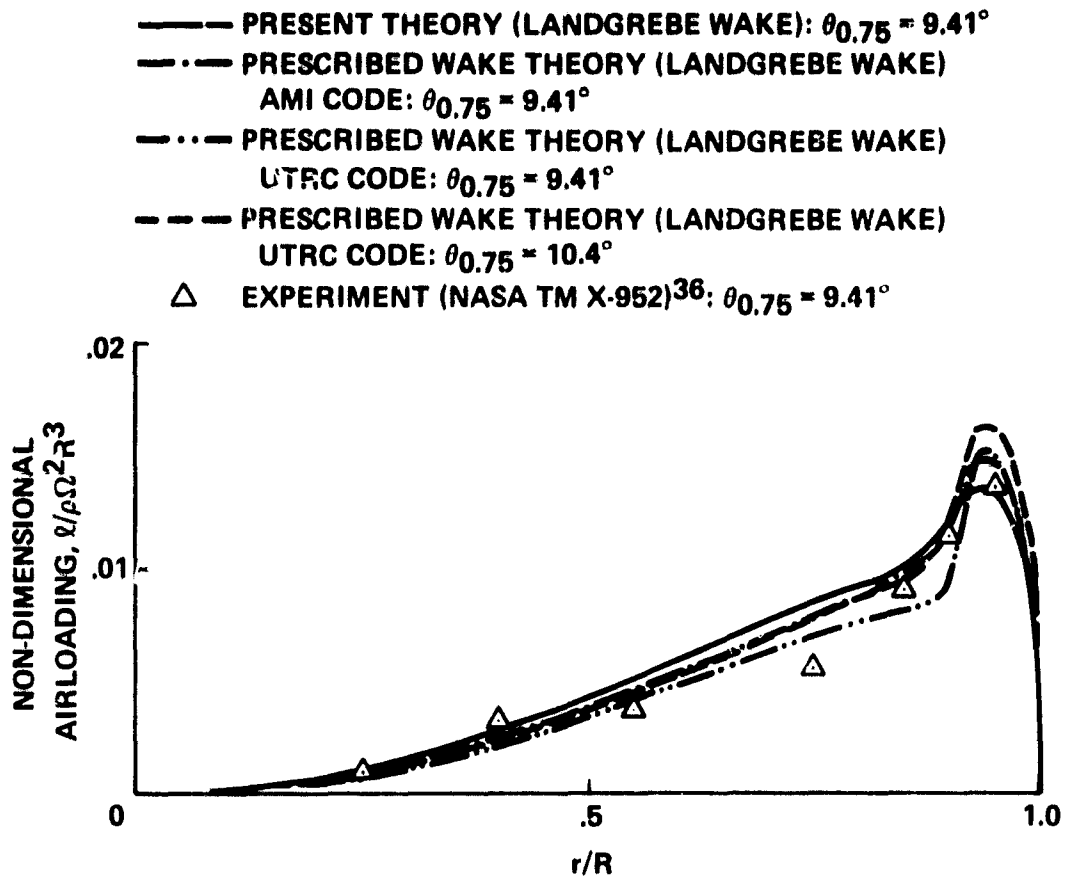

Fig. 32 Comparison of measured and calculated spanwise lift distributions in hover, with Landgrebe wake model , (b = 4, θt = -8.0 deg., AR = 20.5).

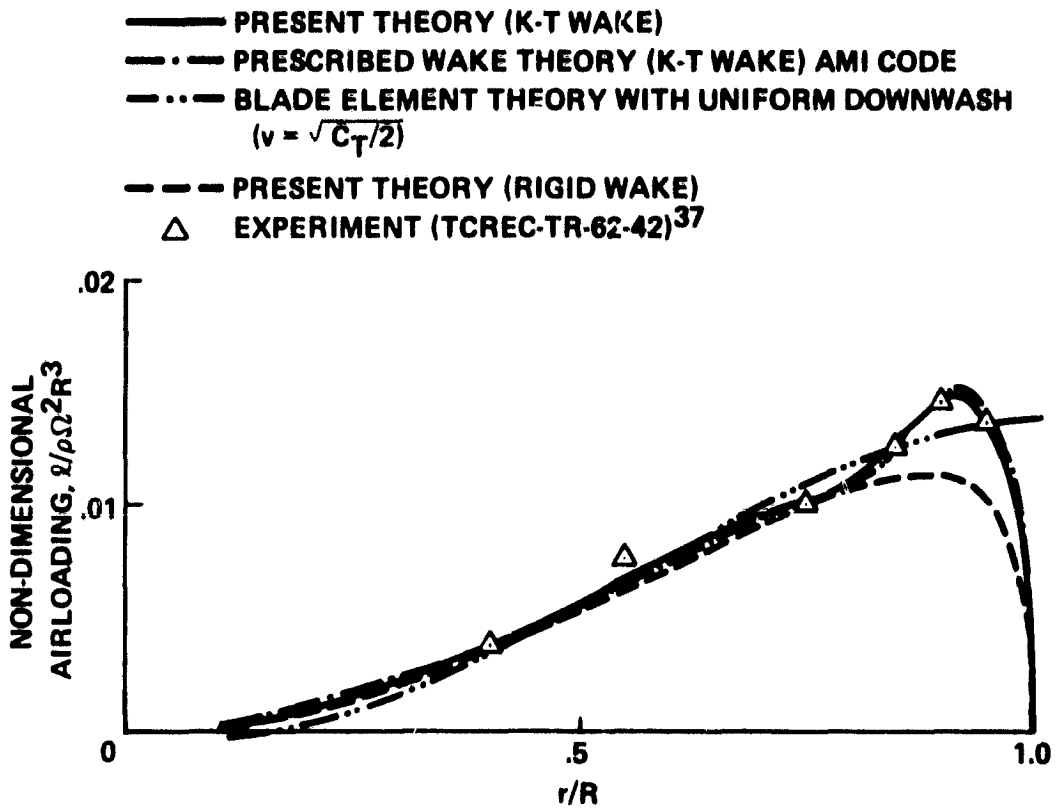

Fig. 33 Comparison of measured and calculated spanwise lift distributions in hover, with Kocurek and Tangular wake model, (b = 2, θt = -12.0 deg., AR = 17.3, $\theta_{0.75}$ = 8.97 deg.).

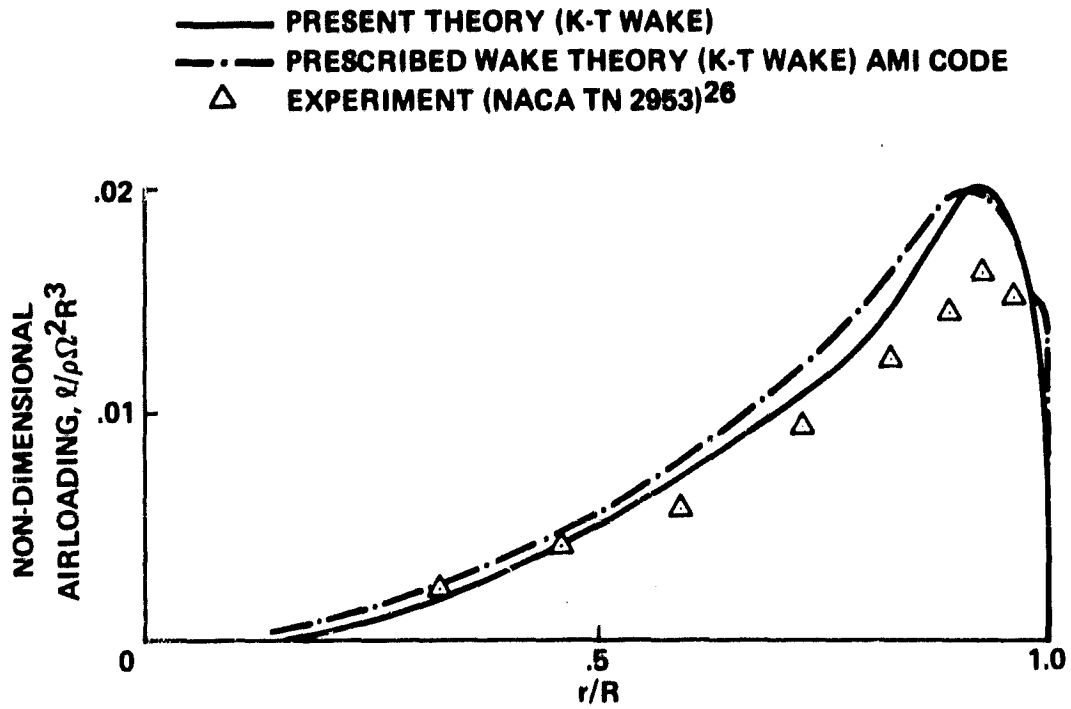

Fig. 34 Comparison of measured and calculated spanwise lift distributions in hover, collective pitch input mode, (b = 2, θt = 0.0 deg., AR = 10.0 deg, $\theta_{.75}$ = 8.0 deg.).

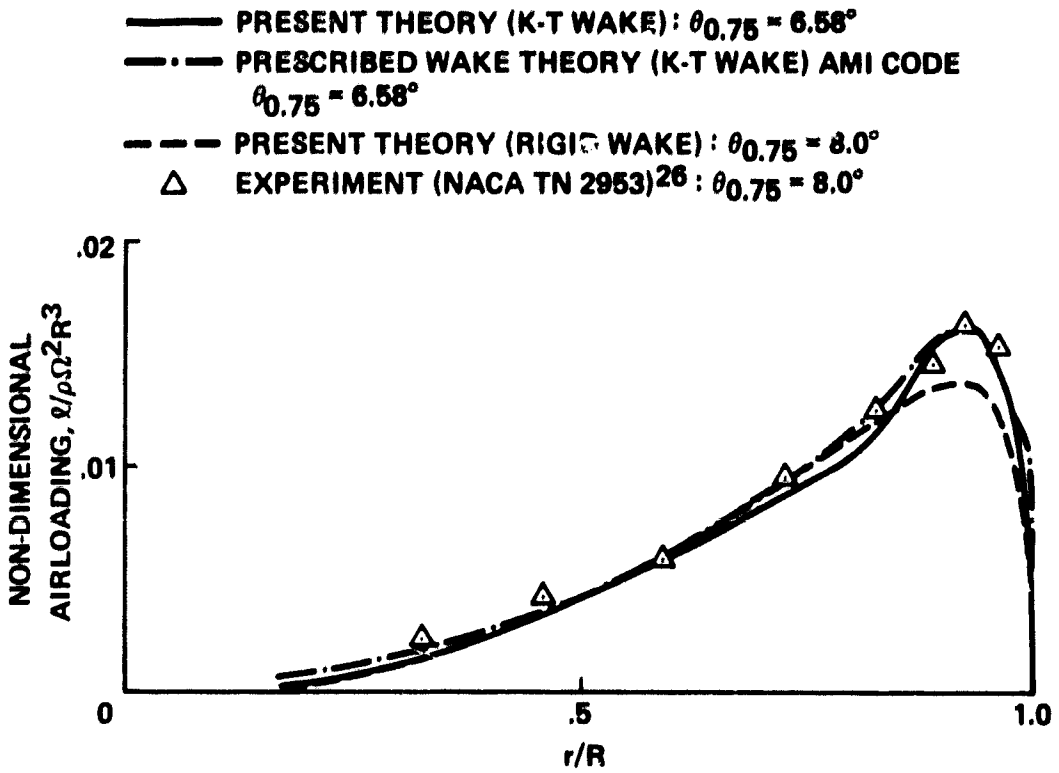

Fig. 35 Comparison of measured and calculated spanwise lift distributions in hover, thrust coefficient input mode, (b = 2, θ_t = 0.0 deg., AR = 10.0).

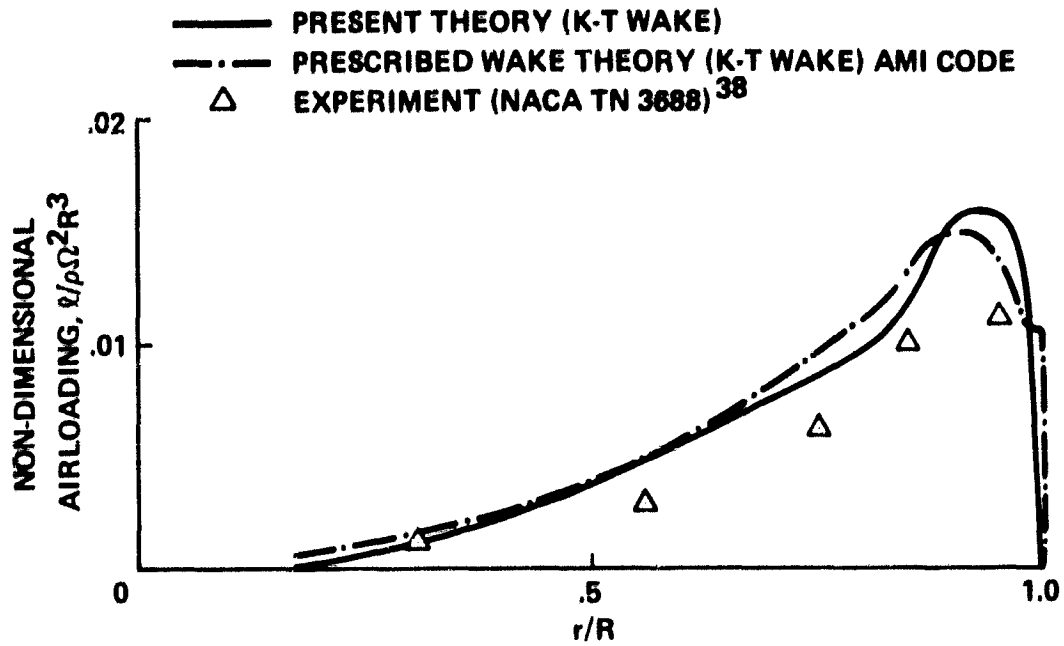

Fig. 36 Comparison of measured and calculated spanwise lift distributions in hover, collective pitch input mode, (b = 2, θ_t = 0.0 deg., AR = 6.54, $\theta_{0.75}$ = 5.3 deg.).

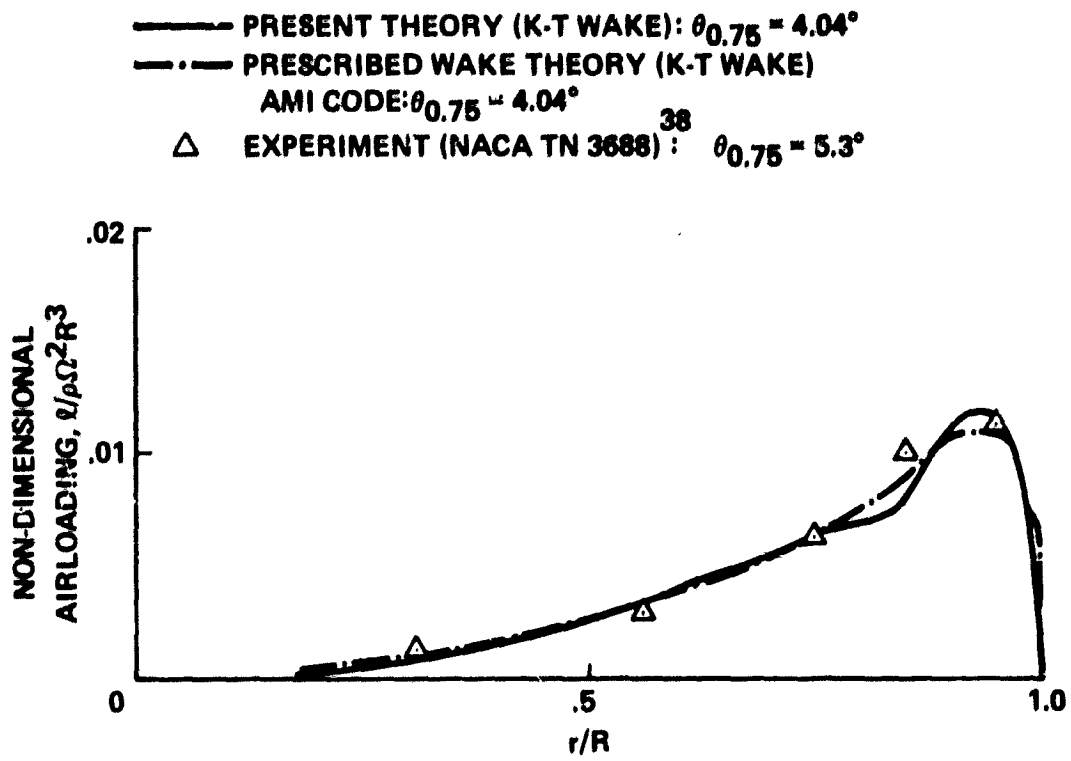

Fig. 37 Comparison of measured and calculated spanwise lift distributions in hover, thrust coefficient input mode, (b = 2, θ_t = 0.0 deg., AR= 6.54).